NUMERICAL SIMULATIONS OF SINGLE-PHASE AND MULTIPHASE REACTING FLOWS UNDER SHOCK AND DETONATION CONDITIONS

by

Prashant Tarey

A dissertation submitted to the faculty of
The University of North Carolina at Charlotte
in partial fulfillment of the requirements
for the degree of Doctor of Philosophy in
Mechanical Engineering

Charlotte

2023

Approved by:

_____
Dr. Praveen Ramaprabhu

_____
Dr. Douglas Schwer

_____
Dr. Russell Keanini

_____
Dr. Yuri Godin

ABSTRACT

PRASHANT TAREY. Numerical Simulations of Single-Phase and Multiphase Reacting Flows Under Shock and Detonation Conditions. (Under the direction of DR. PRAVEEN RAMAPRABHU)

Mode transition in Rotating Detonation Engines (RDEs) refers to an abrupt change in the number of detonation waves due to a change in inlet conditions such as the injected fuel reactivity and total pressure. Previous theories describing mode transition were based on 2D detonation tube models, and stipulate that the detonation wave (DW) height should be an integral multiple of the detonation cell width for stability. According to this mechanism, with changes in inlet conditions, the detonation cell width can change, and along with it the DW height resulting in mode transition. Through detailed numerical simulations in a 2D unrolled RDE geometry, an alternate mechanism for mode transition is proposed, along with a corresponding quantitative criterion that is validated using simulation data. We observed mode transition when the N_2 dilution of the injected fuel mixture was reduced, so that the more reactive, fresh mixture injected into the combustion chamber triggered a localized, micro-detonation to form. In the simulations, we observe the micro-detonation to eventually lead to a mode transition when $\tau_{MD}<\tau_L$, where τ_L is the time of revolution of the parent DW and τ_{MD} is the time required for a 'micro-detonation' to form. When this criteria was not satisfied, the parent DW consumed the fuel mixture in the hot spot, before a daughter wave could form. A relationship to predict the number of DWs following mode transition is also proposed and verified using simulation data.

In the second part of this thesis, we describe detailed numerical simulations of a liquid fuel droplet impacted by a Mach 5 shock wave, considering the effects of chemical reactions and phase change due to evaporation. In our baseline case, a $5\,\mu m$, $n-Dodecane$ fuel droplet is preheated to $460\,K$, and surrounded by preheated O_2 gas at $700\,K$. The fuel droplet undergoes significant

deformation and morphological changes following shock impingement, as the droplet surface becomes unstable to the Kelvin-Helmholtz instability. The droplet core is also observed to eject a thin sheet near the equatorial plane, which is then stretched by the high-speed post-shock gas flow, affecting the late-time behavior. We find the observed dominant modes associated with the Kelvin-Helmholtz instability are in reasonable agreement with linear theory [1, 2], when the local conditions at the droplet surface are considered. The production of fuel vapors by the droplet impairs the growth of such surface instabilities, leading to reduced growth of the droplet surface area when compared with a non-evaporating droplet. Furthermore, an evaporation-induced Stefan flow is established which blows off the hot post-shock gasses surrounding the droplet, leading to droplet cooling. As the fuel vapors react, a diffusion flame is formed on the droplet-windward side, leading to intense droplet heating and enhanced vapor production in this region. In contrast, the leeward side of the droplet is occupied by pre-shock gasses entrapped in a low-pressure region formed by flow separation, resulting in lower temperatures and vapor production at that site. We investigated the effect of the Damkohler number on droplet evolution by varying the fuel reactivity, and found the flame thickness decreased with increasing reactivity in agreement with trends predicted by laminar diffusion flame theory. In addition, the greater consumption of fuel vapor in the region surrounding the droplet at higher reactivities, resulted in increased growth of the droplet surface area, and increased expansion rate of the ejected thin sheet structures. At the highest reactivity, secondary burning of fuel vapors was observed in the droplet wake, while the resulting flame eventually reattached to the droplet surface. Our results show significant spatial inhomogeneities are present in the droplet flowfield in all the cases investigated, which must be considered in the development of reduced order point-particle models for system-level simulations of detonation engines.

ACKNOWLEDGEMENTS

First and foremost, I would like to express my gratitude to my PhD advisor, Dr. Praveen Ramaprabhu who trusted me with the two most interesting projects from our research group, to work on for my PhD. He has always encouraged me to aim for innovative solutions to harder problems. The deep scientific discussions with him has always helped me to convert a raw idea into a presentable form. I would like to thank Drs. Douglas Schwer, Russell Keanini, Shaozhong Deng and Yuri Godin for serving as my committee members and providing me with valuable feedback on my research. During my research I was fortunate to have esteemed guidance from Dr Jacob McFarland for my Shock-Droplet interaction project and Dr. Douglas Schwer for my Rotating Detonation Engine project. I wish to acknowledge the help I received from Dr. Nitesh Attal and Dr. Ismael Boureima in learning the FLASH code and Dr. Pedram Bigdelou and Mr. Chen Liu for explaining me the IMPACT code. The continued support and encouragement from my friends and labmates, Dr. Peyman Razi, Mr. Madhav Nagori and Mr. Kelso Kitowski always kept me motivated. Finally, on a personal level, I am grateful to my family and especially my parents for always being unconditionally supportive during my long journey towards a Doctoral degree. This work was supported by the National Science Foundation under grant no: 1933479. The software used in this work was developed in part by the DOE NNSA ASC- and DOE Office of Science ASCR-supported Flash Center for Computational Science at the University of Chicago.

TABLE OF CONTENTS

LIST OF TABLES

LIST OF FIGURES

CHAPTER 1:INTRODUCTION

In this work, we have investigated using detailed numerical simulations, the properties of detonation waves occurring in single-phase rotating detonation engines and the evolution of a shock-driven liquid fuel droplet. The studies span vastly different scales from the microscale at which the behavior of an isolated liquid fuel droplet has been investigated to device-scale simulations of a gas-phase rotating detonation engine. Our simulations of the gas-phase rotating engine have highlighted the possibility of a new pathway to mode transition, in which the number of detonation waves can change abruptly, along with a discussion of the impact of such a phenomenon on engine operation. To address the behavior of an isolated liquid fuel droplet driven by a shockwave considering the effects of surface tension, evaporation and chemical reactions, we have developed extensive numerical capabilities in our Direct Numerical Simulation code called IMPACT.

1.1 Rotating Detonation Engines

Rotating Detonation Engines (RDEs) represent a relatively new concept in pressure gain combustion, where a detonation wave (DW) formed from injected mixture, travels circumferentially within an annular channel. The DW compresses the fuel to much higher pressures, resulting in the extraction of additional work and efficiencies not accessible through the conventional Brayton cycle. Unlike conventional engine designs, RDEs have no moving parts, making their manufacturing simpler, while their compact design increases their payload carrying capacity [3]. Conventional combustion engines are limited to operating at subsonic speeds, and can only operate at supersonic by decelerating the intake air to subsonic velocities to enable combustion, which generates heat and drag. In contrast, detonations in RDEs occur at supersonic speeds, which can be achieved without decelerating the intake air resulting in higher efficiencies

and reduced heat loss and drag [4]. In recent years, RDEs have gained significant attention [5-8] owing to their higher theoretical efficiencies (up to 25% increase over the Brayton cycle), including several experimental [9-13] and numerical [6, 7, 11-17] investigations. It has been observed that the number of DWs (nW) can abruptly change in an RDE, due to a change in the inlet conditions such as the fuel reactivity, mass flow rate or chamber pressure. This phenomenon has been termed mode transition in the RDE literature [18-21].

Existing theories of mode transition [12-17] in RDEs are based on fundamental detonation tube models and experiments. For a DW to self-propagate in a detonation tube, there should exist at least n_{crit} number of triple points along its height. If this condition is not met (i.e. $h<n_{crit}\lambda$), the DW can extinguish due to heat loss to the tube walls. A similar phenomenon has been observed for detonation waves in RDEs, where it has been observed that when the detonation height is not an integer multiple of λ, mode transition can occur as observed in the experiments of [13, 18]. However, in practical RDE devices, due to the presence of highly turbulent and inhomogeneous flowfield ahead of the detonation wave, the network of triple points can be disrupted. Yet, we find from our simulations that mode transition can occur, even in the absence of the detonation cell network, suggesting an alternate mechanism at play. Specifically, our simulations show that when the reactivity of the inlet mixture was varied, local hot spots can develop first into micro-detonations, and eventually into detonation waves. A necessary condition for mode transition is proposed, based on two timescales of the flow, namely the time of revolution of the parent DW τ_L, and a 'micro-detonation' time τ_{MD} that represents the deflagration-to-detonation (DDT) time of a local hot spot.

1.2 Shock-Droplet Interaction

Shock-driven droplet breakup, evaporation, and reaction plays an important role in liquid fuel droplet combustion, with applications in scramjets [22-25], Rotating Detonation Engines (RDEs) [26, 27] , and several industrial phenomena [28]. Liquid fuels have the advantage of ease of storage, higher energy density (defined as energy per unit volume) leading to higher thrust-to-weight ratios, and the ability to be used as a coolant, making them an attractive energy source for engines [29, 30]. Gaseous fuels, such as Liquified Natural Gas (LNG) and Compressed Natural Gas (CNG), can provide up to 25% higher specific energy (defined as energy per unit mass) [31, 32] when compared to liquid fuels like Jet-A and Kerosene. However, gaseous fuels are required to be maintained at low cryogenic temperatures (~ -160 °C for LNG [33] at atmospheric pressure) or high pressures (~ 250 atm at room temperature for CNG [34]), presenting challenges in their handling and storage. Despite their increased specific energy, the energy density remains lower than liquid fuels such as Jet-A or Diesel (~60% for LNG [32] and ~25% for CNG [32]). Due to these challenges in the storage of gaseous fuels and the high volume they occupy even in their liquified or compressed state, there is an increased interest in the use of liquid fuel for detonation engines [26, 27]. In a typical detonation engine, the liquid fuel is injected into the combustion chamber [26], where the high-speed gas fragments the liquid jet into droplets, called *primary* breakup, while the droplets may undergo further deformation and *secondary* breakup . As the fuel droplets deform, the high temperature environment within the combustion chamber [22, 35, 36] also leads to evaporation, a process that is further enhanced by the instability-driven increase in the total surface area of the droplets due to its stretching [37, 38]. The fuel vapors produced from evaporation undergo combustion, thereby generating thrust and energy; thus, the overall efficiency of the engine is closely linked to the rate of droplet conversion to fuel vapors involving stretching,

breakup and evaporation. For typical scramjet operation, the combustor flow will have Mach numbers in the range 2 - 3 [22, 25], while detonation waves in RDEs are expected to operate at even higher Mach numbers. For a typical combustor section of length $\sim 1\,m$ [22, 39], the corresponding residence time of fuel droplets will be $\mathcal{O}(ms)$ [22], during which the droplets will have to disintegrate, evaporate and burn.

While significant progress has been made in our understanding of gaseous fuel-air mixing and combustion phenomena, the fundamentals of liquid fuel combustion are still poorly understood [40, 41]. For efficient combustion in detonation engines, fuel droplets must undergo rapid conversion to vapor through instability, breakup and phase change. This has motivated several experimental [42-48] and numerical [49-54] studies that have focused extensively on droplet breakup mechanisms and their dependence on different operating parameters. A significant source of uncertainty remains however in the coupling between the evaporation, reactions and droplet surface instabilities. Thus, the primary focus of this numerical work is to investigate the evolution of a shock-driven fuel droplet under the combined effects of surface tension mediated deformation, evaporation and reactions. In this section, we first summarize some previous investigations of non-evaporating, evaporating and reacting droplets using experiments and simulations.

Over the past century, theoretical and experimental work on liquid jets and droplet breakup has laid the foundation for detailed droplet breakup theories [55-57]. For large liquid-to-gas density ratios, shock-driven droplet breakup characteristics are influenced by the Weber number, $We = \frac{\rho_{ps} u_{ps}^2 D}{\sigma}$ (where ρ_{ps}, u_{ps}, D and σ are the density, relative velocity, droplet diameter and surface tension respectively, and the subscript 'ps' denotes post-shock gas conditions), and the Ohnesorge number $Oh = \frac{\sqrt{We}}{Re}$. For $Oh < 0.1$, viscous effects are insignificant, so that the droplet

breakup regimes are governed primarily by the Weber number [42, 43, 57]. For a liquid droplet under a gas flow, the different breakup regimes observed experimentally [58-60] are: vibrational modes ($We < 10$), bag breakup ($10 \leq We < 30$), multi-bag ($30 \leq We < 80$), shear breakup ($80 \leq We < 350$), and catastrophic ($We > 350$). The recent experiments of Theofanous [42-44] have highlighted the existence of two dominant modes of droplet breakup, namely Rayleigh Taylor (RT) piercing ($We < 10^2$) stemming from the growth of RT instability at the front face of the droplet, resulting in bag and multi-bag droplet breakup, and Shear Induced Entrainment (SIE) for $We > 10^3$ due to the formation of KHI instabilities at the droplet equator, with a mixed RTI and SIE regime for intermediate Weber numbers ~10^2 to 10^3. Further experimental studies [47, 48] have supported these findings, including the existence of mixed RT and SIE regimes.

Droplet breakup has also been investigated using 2D and 3D simulations over a wide range of Weber numbers. The authors of [35, 36] studied the effect of the Ohnesorge and Weber numbers on droplet breakup at liquid-to-gas density ratios of 10.0 and 1.15. Jalaal and Mehravaran [61] performed 2D and 3D shock-droplet simulations at $We = 50 - 200$, that showed KH instabilities form at the equator and are pulled downstream by the gas flow to create an axisymmetric sheet, which is then punctured by azimuthal RT instabilities, disintegrating the liquid sheet into child droplets. More recently, the 3D simulations by Meng and Colonius [50] reached similar conclusions about the formation of liquid sheets due to KH instabilities, although only broadband wavelengths were observed. For a more detailed discussion of droplet breakup mechanisms, please see recent review article by [62].

In spite of their relevance to several high-speed engine designs and concepts, there have been relatively few studies of evaporating or reacting droplets that have been impacted by a shock or high-speed background gas flow. Jeng and Deng [63] simulated an $n - Dodecane$ evaporating

droplet developing in a convective flow at $Re = 100$ and Weber numbers ranging from $1.33 - 298$, and found that the evolution of droplet deformation was largely unaffected by evaporation. They further observed that the evaporation rate per unit area decreased as the droplets underwent deformation, due to the formation of recirculation regions behind the droplets where the evaporation rate was significantly lower. The evaporation and reaction of a $230\ \mu m$, aluminum particle pre-heated to 2750K, and driven by $M = 2 - 4$ shocks ($We = 200 - 2800$) were simulated by Houim and Kuo [38]. They observed that as the surface area of the droplet increased due to deformation, the evaporation rate of the droplet exceeded that of a droplet in a quiescent environment. Similarly, Das and Udaykumar [64] varied the Mach number ($M = 1.1 - 3.5$) and Reynold number ($Re = 100 - 1000$) in their simulations of a shock-impacted aluminum droplet, and observed a transition from an attached flame at low Damkohler numbers to a droplet-detached flame at high Damkohler numbers.

More recently, Redding and Khare [65] simulated vaporization of a $100\ \mu m\ \ n - dodecane$ droplet impacted by $M = 2.4$ and $M = 6.5$ shock waves. With the increase in shock Mach number, the evaporation rate was found to decrease, due to the higher post-shock pressures surrounding the droplets at higher M. Furthermore, higher droplet evaporation rates led to suppression of the hydrodynamic instabilities at the droplet-gas interface. Recently, Boyd and Jarrahbashi [66] numerically studied using 2D axisymmetric simulations, the transcritical shock-droplet interaction (TSDI) problem involving a $5\ cm$, $n - Dodecane$ droplet. They noted that for a diverging TSDI, where the fuel is in a *liquid-like* state, a behavior similar to a classical subcritical liquid shock-droplet interaction (SDI) is observed; in contrast, a converging TSDI where the fuel is in a *gas-like* state, exhibited behavior similar to the classical shock-bubble interaction (SBI) problem. Strotos et al. [67] simulated droplet evaporation and breakup of a $100\ \mu m$, 2D

axisymmetric n-heptane droplet, and found that droplet heating and evaporation played a minor effect on breakup, due to the short time scales of droplet deformation compared to the heating time scales.

The majority of experimental studies of shock-droplet interactions [43-45, 47, 48, 68] have addressed, due to diagnostic limitations, droplets of $1 - 5\,mm$ diameter, at density ratios of $\mathcal{O}(1000)$ and near-atmospheric conditions $(0.1 - 1\,atm)$. Similarly, full-scale 3D simulations are challenged by the need to resolve the most unstable KHI wavelengths, with the dominant wavenumbers and the number of mesh points per droplet diameter scaling as ~ We. In this work, we report on detailed, 2D axisymmetric simulations that fully resolve interfacial instabilities on the droplet surface, and investigate the coupling between droplet evaporation, gas phase reaction and deformation due to instability growth. To the best of our knowledge, this is the first such study on the combined effects of droplet deformation, evaporation and reactions on the evolution of a shock-driven hydrocarbon fuel droplet, under conditions relevant to detonation engines.

The rest of this dissertation is organized as follows: Details of the numerical setup, including governing equations and discretization method are described in Chapter 2, for both FLASH (§ 2.1) and IMPACT (§ 2.2). The results from simulations of RDEs are discussed in Chapter 3, and include the Simulation setup (§ 3.1) and Initial conditions (§ 3.2.1), followed by phenomenological description of mode transition using several cases simulated (§ 3.2.2, § 3.2.3, § 3.2.4). We present a simple model to predict mode transition in RDEs in § 3.3, followed by thrust analysis for RDEs in § 3.4. In Chapter 4, simulation results from the shock-droplet interaction problem for a liquid fuel droplet are presented. The problem setup for 2D simulations is given in § 4.1. Results from the simulations include 1D simulations of an evaporating and reacting liquid-gas interface (§ 4.2), 2D shock-droplet interaction of a notional $n - Dodecane$ fuel droplet considering the effects of

surface tension, evaporation and reactions (§ 4.3), and an investigation of the effect of varying the droplet Damkohler number (§ 4.4). Finally the Conclusions are presented in Chapter 5, for both mode transition phenomenon in RDEs (§5.1) and evolution of shock impinged liquid fuel droplet (§ 5.2).

CHAPTER 2:NUMERICAL SETUP

The gas phase RDE simulations were performed using a modified version of the astrophysical FLASH code [69], where reacting flow capabilities including detailed chemistry, multi-species EOS and temperature-dependent transport and thermal properties were added as described in [70]. The microscale simulations of the liquid fuel droplet were investigated using IMPACT, an in-house Direct Numerical Simulation code, with multi-material and multi-physics capabilities as detailed in § 2.2 below.

2.1 FLASH

2.1.1 Governing Equations

In this section, we describe the governing equations used in FLASH for the gas-phase RDE simulations. The inviscid, compressible reacting multispecies 2D Euler equations were solved, as shown below:

$$\frac{\partial \rho}{\partial t} + \nabla.(\rho \mathbf{v}) = 0 \tag{2.1}$$

$$\frac{\partial \rho Y_i}{\partial t} + \nabla.(\rho Y_i \mathbf{v}) = \dot{\omega}_{i,rxn} \tag{2.2}$$

$$\frac{\partial \rho \mathbf{v}}{\partial t} + \nabla.(\rho \mathbf{v}\mathbf{v}) + \nabla P = 0 \tag{2.3}$$

$$\frac{\partial \rho E}{\partial t} + \nabla.[(\rho E + P)\mathbf{v}] = 0 \tag{2.4}$$

where, ρ, $\mathbf{v}$, Y_i ,$\dot{\omega}_{i,rxn}$ and P represents density, velocity, mass fraction of i^{th} species, volumetric source term due to reactions for i^{th} species, and pressure respectively, while E represents the sum of internal energy ϵ and kinetic energy per unit mass,

$$E = \epsilon + \frac{1}{2}|\mathbf{v}|^2 \tag{2.5}$$

An ideal gas Equation of State (EOS) is used in this work, where the pressure is obtained from density and internal energy as follows:

$$P = (\gamma - 1)\rho\epsilon \tag{2.6}$$

$$\epsilon = E - \frac{1}{2}|\mathbf{v}|^2 \tag{2.7}$$

where γ is a ratio of specific heat capacity at constant pressure and constant volume. However, in regions where the kinetic energy is the dominating term in the total energy, obtaining internal energy ϵ, using eq. (2.7) can lead to significant errors in pressure and temperatures. Therefore, to avoid this problem in FLASH, the internal energy (ϵ) is separately evolved in time using eq. (2.8), while the pressure and temperature are calculated using the internal energy (ϵ) obtained directly from eq. (2.8). In addition, in regions where the internal energy (ϵ) falls below 10^{-4} of the kinetic energy $\left(\frac{1}{2}|\mathbf{v}|^2\right)$, the total energy (E) is recalculated using eq. (2.5), with the internal energy from eq. (2.8), and velocities from momentum equations.

$$\frac{\partial \rho\epsilon}{\partial t} + \nabla.[(\rho\epsilon + P)\mathbf{v}] - \mathbf{v}.\nabla P = 0 \tag{2.8}$$

2.1.2 Numerical method

The numerical simulations were performed using FLASH [69], a finite volume Eulerian code, which includes capabilities such as Adaptive Mesh Refinement (AMR), split and unsplit hydrodynamic solvers, WENO [71, 72] and Piecewise Parabolic Method (PPM) [72, 73], and approximate Riemann solvers. For this work, the inviscid Euler equations (eqs. (2.1)-(2.4) and (2.8)) were solved numerically, without mass diffusivity and thermal conductivity effects, using an unsplit solver, coupled with an HLLC Riemann solver. Reaction libraries were developed as described in [70], and capable of solving multi-species and multistep reaction networks, with

variable specific heat capacities modeled using NASA temperature polynomials [74]. Finally, to simulate the solid objects, used to model discrete injectors in RDE, a 2^{nd} order accurate, immersed boundary method [75] was implemented in FLASH.

2.2 IMPACT

Multi-material compressible flows occur in several applications of practical importance such as combustion [22, 26, 28], cavitation [76] and shock lithotripsy [77, 78]. In order to solve such flows numerically with improved efficiency and accuracy, the use of Ghost Fluid Method (GFM) [79, 80] and its derivatives [38, 81-86] have been widely used. Our in-house code, IMPACT [87] is a sharp interface, multi-material shock-physics code, capable of solving numerically challenging problems such as high Mach number ($\sim > 5$) shock-droplet interaction under reaction conditions and shock-bubble interaction. In IMPACT, the interface between the liquid and gaseous phase is tracked using the Level Set method [88, 89], and a Riemann Solver based Ghost Fluid Method (RS-GFM) [85, 86] integrated with a multi-medium exact Riemann solver [38, 85, 86] is used to couple the two phases. In order to achieve higher order accuracy, a 5^{th} order WENO [71, 90] scheme is used along with Adaptive Mesh Refinement (AMR) capabilities on a block-structured mesh (implemented using an Open MPI AMR library PARAMESH [91, 92]). In addition, IMPACT incorporates temperature-dependent correlations to model the thermodynamic [93, 94] and transport properties [93, 95] of multispecies gases, multiple Equation of State (EOS) such as the ideal gas equation for the gas phase and the Stiff Gas equation [86] and Tait's equation [38] for the liquid phase, Schrage-Knudsen evaporation law [96] for interphase mass transfer and one step gas phase reaction [93]. Additional details of the numerical methods used in IMPACT are given below.

2.2.1 Governing Equations

For both the gas and liquid phases, the 2D axisymmetric inviscid equations given below were solved. The details of the governing equations for each phase are described below eq. (2.9):

Gas Phase Equations

The gas phase is represented by the multispecies Euler equations, with thermal and mass diffusion effects, as shown in eq. (2.9):

$$\begin{gathered}
\frac{\partial(\rho Y_i)}{\partial t}+\frac{\partial(\rho u Y_i)}{\partial x}+\frac{\partial(\rho v Y_i)}{\partial y}+\eta\frac{\rho v Y_i}{y}=-\frac{\partial J_{x,i}}{\partial x}-\frac{1}{y^\eta}\frac{\partial(y^\eta J_{y,i})}{\partial y}+\dot{\omega}_{i,evap}+\dot{\omega}_{i,rxn}\,, \\
i=O_2, C_{12}H_{26}, Pr \\
\frac{\partial(\rho u)}{\partial t}+\frac{\partial(\rho u^2+p)}{\partial x}+\frac{\partial(\rho v u)}{\partial y}+\eta\frac{\rho v u}{y^\eta}=0 \\
\frac{\partial(\rho v)}{\partial t}+\frac{\partial(\rho u v)}{\partial x}+\frac{\partial(\rho v^2+p)}{\partial y}+\eta\frac{\rho v^2}{y^\eta}=0 \\
\frac{\partial(\rho E)}{\partial t}+\frac{\partial\big(u(\rho E+p)\big)}{\partial x}+\frac{\partial\big(v(\rho E+p)\big)}{\partial y}+\eta\frac{v(\rho E+p)}{y^\eta} \\
=-\frac{\partial q_x}{\partial x}-\frac{1}{y^\eta}\frac{\partial(y^\eta q_y)}{\partial y}+\dot{Q}_{evap}
\end{gathered} \tag{2.9}$$

where, Y_i, u, v, p and E are the species mass fractions, axial and radial velocities, pressure and specific total energy. The species source terms due to evaporation, reactions and energy source term are represented by $\dot{\omega}_{i,evap}$, $\dot{\omega}_{i,rxn}$ and $\dot{Q}_{evap}$ in eq. (2.9). The variable η denotes the coordinate system for the problem, where η = 0 or 1 select 2D Cartesian or axisymmetric coordinates respectively. The gas phase is composed of three species, $O_2, n-Dodecane$ $(C_{12}H_{26})$ and $Prod$ which represents the mixture-averaged single species of $C_{12}H_{26}-O_2$ combustion products based on the JetSurF-2.0 [97] detailed reaction mechanism outlined in [93]. Specific heat capacity $(C_{p,i})$ for all the species were modeled using NASA7 temperature polynomials [93, 94]. Sutherland's law [93] was used to represent the temperature-dependent thermal conductivity (λ_i) of O_2 and $Prod$, while $C_{12}H_{26}$ was modeled using a three-coefficient

polynomial for thermal conductivity [93]. The mass diffusion coefficient ($D_{i,mix}$) for each species was taken to be that of the $O_2 - C_{12}H_{26}$ binary system ($D_{O_2,C_{12}H_{26}}$), evaluated here using the Chapman-Enskog approach [95]. Additional details of the temperature-dependent correlations for $C_{p,i}$, λ_i and $D_{i,mix}$ can be found in [93].

We model the evaporation of liquid fuel into the gas phase using the Schrage-Knudsen evaporation law [96]:

$$\dot{m}''_{l,evap} = \frac{2a}{2-a}\sqrt{\frac{Mw_l}{2\pi R_u}}\left(\frac{p_{sat}(T_{l,int})}{\sqrt{T_{l,int}}} - \frac{p_{vap,int}}{\sqrt{T_{g,int}}}\right) \tag{2.10}$$

where $\dot{m}''_{l,evap}$, Mw_l, R_u, $p_{sat}(T_{l,int})$, $p_{vap,int}$, and $T_{g,int}$ are the evaporation mass flux, fuel molecular weight, universal gas constant, saturation pressure of the liquid at the interfacial liquid temperature $T_{l,int}$, vapor partial pressure at the interface and gas temperature at the interface respectively. The condensation coefficient a in eq. (2.11) is given by,

$$a = \left(1 - \left(\frac{\rho_{g,int}}{\rho_{l,int}}\right)^{\frac{1}{3}}\right)\exp\left(-\frac{1}{2\left(\frac{\rho_{l,int}}{\rho_{g,int}}\right)^{\frac{1}{3}} - 2}\right) \tag{2.11}$$

while $\rho_{g,int}$ and $\rho_{l,int}$ are the gas and liquid densities at the interface. In Appendix § A, we present results from validation of the evaporation model using data from molecular dynamics simulations.

A single-step, irreversible reaction mechanism as described in [93] is used to model the gas phase ($C_{12}H_{26} - O_2$) combustion process:

$$C_{12}H_{26} + 18.5\ O_2 \rightarrow 32.9\ Prod \tag{2.12}$$

The rate of reaction is determined using the Arrhenius law, leading to the following equation for the fuel ($C_{12}H_{26}$) consumption rate:

$$\frac{dY_{C_{12}H_{26}}}{dt} = -\frac{\rho^{(a+b)}}{Mw^{a}_{C_{12}H_{26}} Mw^{b}_{O_2}} A\, exp\left(-\frac{E_A}{R_u T}\right) Y^{a}_{C_{12}H_{26}} Y^{b}_{O_2} \tag{2.13}$$

In eq. (2.13), a and b are the rate constants corresponding to the $C_{12}H_{26}$ and O_2 species, and $Mw_{C_{12}H_{26}}$ and Mw_{O_2} the molecular weights. The coefficients of the above reaction rates are given in Table 1.

Table 1: Arrhenius rate law parameters for $C_{12}H_{26} - O_2$ single step reaction mechanism.

$E_A(cal/mol)$	A	a	b
46500	1.21×10^{10}	1.0	0.75

Liquid phase Equations

For the liquid phase, the single species, inviscid Euler equations were solved with thermal diffusion effects by setting $Y_i = 1$ for liquid $n - Dodecane$ in eq. (2.9), while the mass diffusion and source terms were set to zero. The liquid fuel is modeled as a stiff fluid using Tait's EOS (eq. (2.14)), with the relevant coefficients listed in Table 2.

$$\frac{p + B}{p_\infty + B} = \left(\frac{\rho}{\rho_\infty}\right)^N \tag{2.14}$$

The liquid fuel properties were taken to be constant, independent of Temperature variations within the liquid, and were evaluated as the $n - Dodecane$ properties at $T_{avg} = 0.5(T_0 + T_{crit})$, where $T_0 = 460K$ is the initial temperature of the liquid phase used in all the simulations. For liquids, $h = e + pv \approx e$, therefore following [38] the energy transport in the liquid phase due to thermal diffusion and fluid motion is handled by modeling the liquid phase energy equation as an advection-diffusion equation of the sensible energy e given by $e = e_{ref} + C_v(T - T_{ref})$.

Table 2: List of liquid phase $n-Dodecane$ properties.

$B\ (Pa)$	$p_\infty (Pa)$	$\rho_\infty \left(\frac{kg}{m^3}\right)$	N	$C_v \left(\frac{J}{kgK}\right)$	$\lambda \left(\frac{W}{mK}\right)$	$Mw \left(\frac{kg}{kmol}\right)$
1.0×10^5	1.99×10^8	516.50	7.15	3275.0	0.08387	170.33

2.2.2 Numerical method

The governing equations described above eq. (2.9) are solved using IMPACT [87], a finite volume, multiphase, shock physics code. For the hyperbolic terms, a 5^{th} order WENO method [90] is applied in a direction-by-direction manner to reconstruct cell-face quantities from their cell-centered counterparts, while the Lax-Fredrich (LF) method [98] is used to compute intercell fluxes. In contrast, the parabolic terms are discretized using a 2^{nd} order central differencing scheme similar to [38]. The above discussed spatial discretization is applied to each phase independently, following the ghost cell interpolation step described in § 2.3.

The governing equations for each phase are advanced in time, using an operator splitting method similar to [38], using a third-order TVD-RK method [99]. The time steps Δt were chosen according to $\Delta t = \min(\Delta t_{hyp}, \Delta t_{par})$, where Δt_{hyp} is the timestep obtained from the CFL condition associated with the hyperbolic operator, while Δt_{par} is the timestep dictated by the parabolic operator (for the micron-sized droplets studied here, we typically obtained $\Delta t_{par} \sim \frac{\Delta t_{hyp}}{10}$ to ensure numerical stability). Finally, the source terms $(\dot{m}_{i,evap})$ due to evaporation, were added in a single time step, without requiring any inner time iterations (sub-stepping).

2.2.3 Interface treatment

Levelset

The interface between the liquid and gas phase is tracked through the level set method, by solving the following level set (LS) equation:

$$\frac{\partial \phi}{\partial t} + \vec{V}.\nabla\phi = 0 \tag{2.15}$$

where ϕ is the level set function, which in this case is taken as a signed distance function. Thus, $\phi = 0$ represents the interface, while negative (positive) values correspond to the liquid (gas) regions. The interface velocity $\vec{V}$ in eq. (2.15) is obtained by solving a 1D interface-normal, multi-medium Riemann problem [38, 85, 87]. As described in [87], a reinitialization procedure is applied to ensure the LS function remains a signed distance function, while the fast local level set method of Peng et al. [88] is used, in which the LS calculations are performed over a narrow band of thickness $6dx$ on either side of the interface.

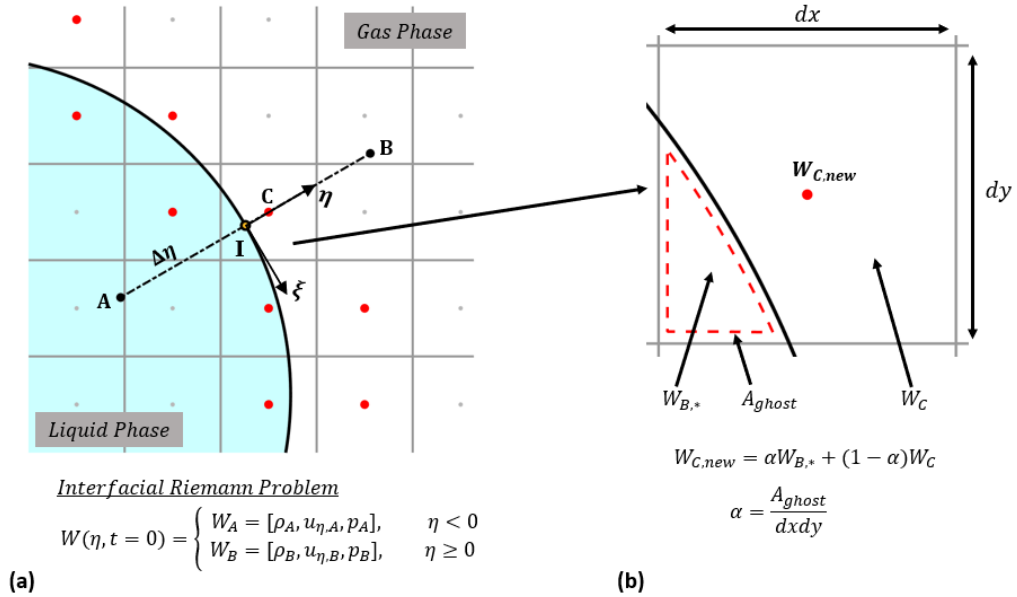

Fig. 2.1: (a) Construction of interfacial Riemann problem by extracting liquid (W_A) and gas (W_B) flow field values, using numerical probes of length $\Delta\eta = 1.5dx$ (dashed lines) extending into each medium; point "C" represents the cell center of the cut cell, point "I" is on the interface, while cells marked in red are the interfacial cells (b). Area-weighted averaging of star

$(W_{B,*})$ and current time step (W_C) values is performed to obtain a new state $W_{C,new}$ in the cut cell C.

Interface coupling

The coupling between the two phases is established through the Riemann solver based ghost fluid method (RS-GFM) [85, 86] (Fig. 2.1), where the ghost cells are populated with the solution to the interfacial Riemann Problem $(W_{A,*}, W_{B,*})$. The RS-GFM is a variation of the general Ghost Fluid Method [79, 80] in which the interface between two media is represented by a layer of fictitious or ghost cells (Fig. 2.1a), which are populated according to the interface boundary conditions and EOS properties in each medium. A cut cell version [100] of the RS-GFM approach is implemented, in which the cut cell values (shown as cell C in Fig. 2.1) are obtained as the area-weighted average of their star state $(W_{B,*})$ and current time step values (W_C):

$$W_{C,new} = \alpha W_{B,*} + (1-\alpha) W_C \tag{2.16}$$

In eq. (2.16), α is the fraction of the cut cell in the ghost region. The above defined cut cell modification in eq. (2.16) implicitly includes the information of the interface shape in the flow field, and results in a smooth representation of the interface [100].

The boundary conditions for the interface-normal mass diffusion fluxes $J''_{i,\eta}\left(\frac{kg}{m^2 s}\right)$ resulting from evaporation, on the gas phase side of the interface are given by [38, 101]

$$J''_{i,\eta} = -Y_i \dot{m}''_{l,evap} + \dot{m}''_{i,evap}\,, \tag{2.17}$$

where $\dot{m}''_{i,evap}$ is the mass production rate due to the i^{th} gas phase species. Since the interface is not always aligned with the cartesian grid, the flux terms $J''_{i,\eta}$ are converted into volumetric mass source terms $\dot{\omega}_{i,evap}\left(\frac{kg}{m^3 s}\right)$ and added to the gas phase equations eq. (2.9):

$$\dot{\omega}_{i,evap} = \begin{cases} J''_{i,\eta}/dx\,, & \phi \leq dx \\ 0, & \phi > dx \end{cases} \tag{2.18}$$

Defining species source terms $\dot{\omega}_{i,evap}$ using eq. (2.19) , adds species mass in a layer of thickness dx adjacent to the interface $(0 < \phi \leq dx)$, and in the real gas phase region. Consequently, the energy source terms $\dot{Q}_{evap}\left(\frac{J}{m^3 s}\right)$ due to evaporation can be estimated as:

$$\dot{Q}_{evap} = \sum \dot{\omega}_{i,evap} h_i \tag{2.19}$$

In the rest of the paper, the subscript $'evap'$ will be dropped, so that $\dot{m}''_{l,evap}$ and $\dot{m}''_{i,evap}$ will be represented by $\dot{m}''_l$ and $\dot{m}''_i$.

A static partial differential equation (PDE) based approach [102] implemented using a fast-sweeping method, is used to extrapolate the flow field variables from interfacial cells into the ghost region. Further implementation details about the interface coupling are given in Appendix § B.

Finally, note that specifying the corresponding interfacial properties using the RS-GFM approach [85] by extracting values along an interface normal (Fig. 2.1) can lead to errors in the interface temperatures $T_{l,int}$ and $T_{g,int}$, particularly during the early stages of droplet evolution. We attribute this to the presence of large temperature gradients between the hot post-shock gasses and the liquid phase, immediately following shock impact. Instead, we compute the evaporation rate in eq. (2.10) by taking $T_{l,int} = T_{g,int} = T_f$ at the interface, where the film temperature T_f was obtained from:

$$T_f = \frac{T_{l,int}\sqrt{\lambda_{l,int}\rho_{l,int}C_{v,l,int}} + T_{g,int}\sqrt{\lambda_{g,int}\rho_{g,int}C_{v,g,int}}}{\sqrt{\lambda_{l,int}\rho_{l,int}C_{v,l,int}} + \sqrt{\lambda_{g,int}\rho_{g,int}C_{v,g,int}}} \tag{2.20}$$

The above equation represents the instantaneous film temperature that is realized at an interface, as two materials at different temperatures are brought in contact [103]. In eq. (2.20), the

interfacial liquid properties, (subscripts l, int) are extracted using the numerical probe labeled A in Fig. 2.1, while the interfacial gas properties (subscripts g, int) are extracted using probe B.

CHAPTER 3:MODE TRANSITION IN ROTATING DETONATION ENGINES

3.1 Simulation setup

A 2D unrolled geometry of an RDE was modeled as shown in Fig. 3.1, with a uniform mesh resolution of 0.025cm in both directions. Discrete injectors were modeled as the negative space between solid objects represented using an Immersed Boundary Method, with a corresponding open area ratio for fuel-air mixture injection of 1/3. The region below the inlet plenum was modeled as a thick layer of a viscous zone, to damp reflected shocks from reentering the chamber and influencing the formation of micro-detonations. A 7-species, 16-step, H_2-O_2 reaction mechanism [104] suitable for high pressure combustion, was used to simulate chemical reactions, while the working fuel was diluted with Nitrogen in the simulations. All the RDE simulations were initialized with the 'fundamental' mode (1 DW) established by inlet conditions of 5 moles of N_2 dilution. The simulations were run for several cycles before data collection, to ensure that the RDE was operating at a steady state. The plenum pressure was kept constant at 5 atm for all the cases simulated, and mode transition was triggered by varying the N_2 dilution in the injected mixture. Due to a decrease in N_2 dilution, the reactivity of the injected mixture increases, which can result in the formation of micro-detonation (MD) in the combustion chamber, triggering mode transition.

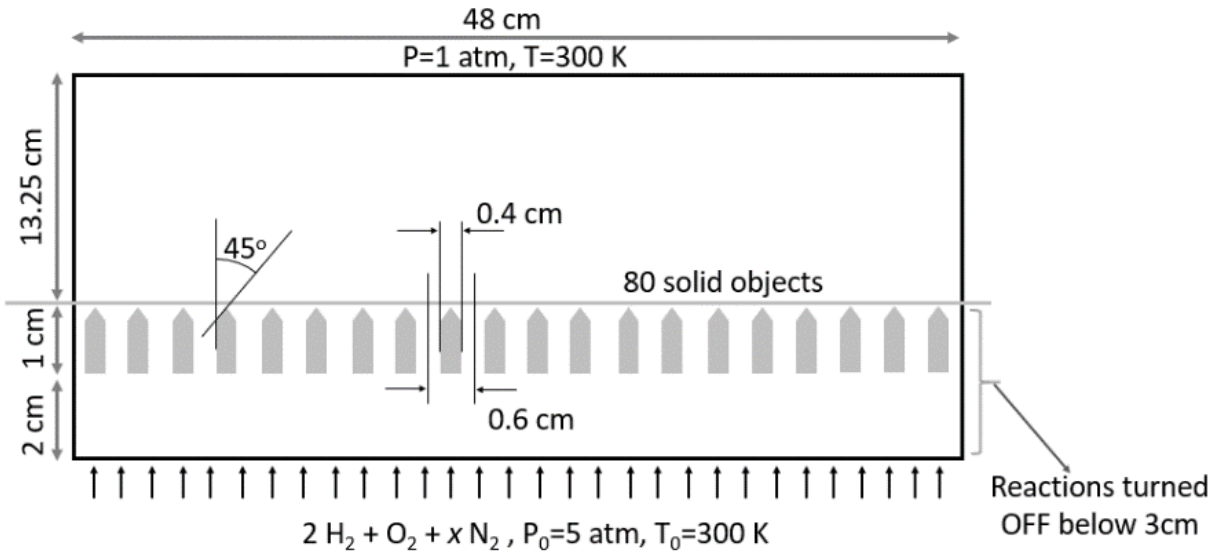

Fig. 3.1 2D unrolled RDE geometry employed in FLASH simulations.

3.2 Qualitative results

Mode transition in RDE can occur due to a change in fuel reactivity, mass flow rate or plenum pressure. Variations in fuel reactivity can occur due to changes in nitrogen dilution or the equivalence ratio; similarly, the mass flow rate can vary due to changes in the plenum pressure. In this study, a stoichiometric mixture of H_2 and O_2 was chosen as the working fuel with N_2 as the diluent, while mode transition was initiated by varying the fuel reactivity, which can be achieved by changing the number of moles of N_2 per mole of O_2 in the injected fuel mixture. All the simulations were performed in a 2D unrolled geometry with premixed fuel mixture. A total of ten cases were simulated and are outlined in Table 3. In cases 1 - 9, the N_2 concentration was changed from an initial value of 5.0 moles to the different terminal values listed in Table 3 through a single, large perturbation; In case 10, starting from the same initial value, the [N_2] perturbation was increased gradually and incrementally, thus representing an approximation of a continuous trajectory in [N_2] space. Thus, the perturbation path applied in this case mimics the variation of [N_2] in experiments, while also serving to examine if the mode transition observed in our

simulations was sensitive to the specific trajectory along which the perturbations were varied. The rest of the article is organized as follows: First, a description of the simulation setup and initial conditions is presented in § IVA, followed by a detailed discussion of mode transition for a single case discussed in § IVB. Results from cases 1 - 9 are presented in sections IVC, while case 10 is summarized in IVD. Quantitative results describing changes to the performance of the RDE are presented in § V, while the findings are summarized in § VI.

Table 3 Variation in Nitrogen concentration [N_2] and number of detonation waves nW observed in cases 1 - 10.

$Case\ No.$	$Change\ in\ [N_2]$	$Number\ of\ detonation\ waves\ observed, nW$	$Phase\ Reversal$
1	$5.0 \rightarrow 3.5$	1	N
2	$5.0 \rightarrow 3.0$	1	Y
3	$5.0 \rightarrow 2.5$	2	Y
4	$5.0 \rightarrow 2.0$	2	Y
5	$5.0 \rightarrow 1.5$	3	N
6	$5.0 \rightarrow 1.0$	3	N
7	$5.0 \rightarrow 0.75$	4	N
8	$5.0 \rightarrow 0.5$	5	N
9	$5.0 \rightarrow 0.0$	5	Y
10	$5.0 \rightarrow 3.5$	1	N
	$3.5 \rightarrow 3.0$	1	N
	$3.0 \rightarrow 2.5$	2	N
	$2.5 \rightarrow 2.0$	2	N
	$2.0 \rightarrow 1.5$	2	N
	$1.5 \rightarrow 1.0$	2	N
	$1.0 \rightarrow 0.5$	4	N
	$0.5 \rightarrow 0.0$	4	N

3.2.1 Initial conditions/ Base case

Fig. 3.2 shows results from a baseline simulation, and represents an RDE operating in one detonation wave mode under the following conditions: a plenum pressure P_0 of 5 atm, total

temperature T_0 of 300 K, stoichiometric H_2-O_2 fuel mixture at the inlet with 5.0 moles of N_2 per mole of O_2 used as a diluent. The results are presented in terms of temperature, pressure and energy release rate contours, while the array of blocks between y = 2.0cm and y = 3.0cm, represents the solid objects used to model nozzle injectors. Fig. 3.2(d) is a lineout of pressure at y = 3.25cm, where the detonation wave is visible as the pressure spike at x ~ 18 cm. From Fig. 3.2(a), the region containing the cold, unreacted mixture has a reaction rate that is nearly zero, so that no energy is released in the cold mixture region (Fig. 3.2 (c)). The rate of reaction is highest at the DW, which is marked by a thin red line in the contours of the energy release rate and the several blue thin lines in Fig. 3.2(c) represents a mild negative energy release rate, which usually happens due to reverse reactions in a multi-step reaction mechanism. Immediately behind the DW front, the high pressures (~20 atm) prevents cold mixture from entering the chamber. At an additional distance of approximately the height of DW (h), the pressure falls below the plenum pressure. Eventually, at a distance $2h$ behind DW, the pressure drops below the choking pressure, resulting in choked flow in over ~70% of the fuel injectors. Therefore, the cold unburnt fuel mixture enters the combustion zone inside the RDE geometry through an array of weakly supersonic jets. The pressure inside the plenum is highly variable and modulated by pressure waves emanating from the high pressure DW, which are in turn reflected off the bottom surface of the RDE and back into the combustion chamber.

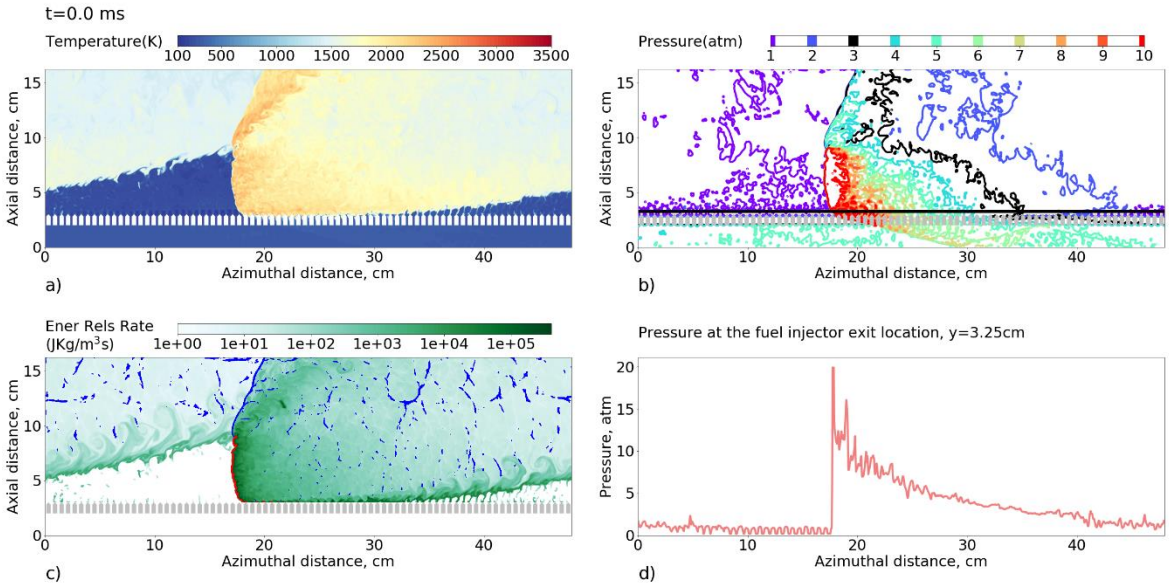

Fig. 3.2 Contours of temperature (a), pressure (b), energy release rate (c) from the baseline simulation operating in 1 DW mode and 5.0 moles of N2. Figure (d) shows a lineout of pressure at y = 3.25cm (visible as a black horizontal line at the bottom of the DW

3.2.2 Variation of [N_2] from 5.0 moles → 1.0 moles:

Starting from conditions corresponding to the baseline discussed in the previous section, the N_2 concentration in the fuel mixture was reduced from 5.0 moles to 1.0 mole (case 6 in Table 3). The resulting large and abrupt change in reactivity of the fuel mixture initiates a sequence of events leading to mode transition: As the more reactive fresh mixture enters the combustion chamber (Fig. 3.3(a)), an increase in the local temperature is observed in the regions now occupied by the newly admitted mixture. Since the Chapman–Jouguet velocity increases with the reactivity (or energy density) of the mixture, the lower segment of the DW is observed to accelerate ahead of the rest of the wave resulting in a deviation from the planar shape. The variability in pressure discussed earlier results in corresponding variations in the inlet mass flow rate of the more reactive fuel. For instance, injectors at locations farther away from the DW (in units of h) see greater hot spot activity (red circles) due to the increased presence of the highly reactive fuel.

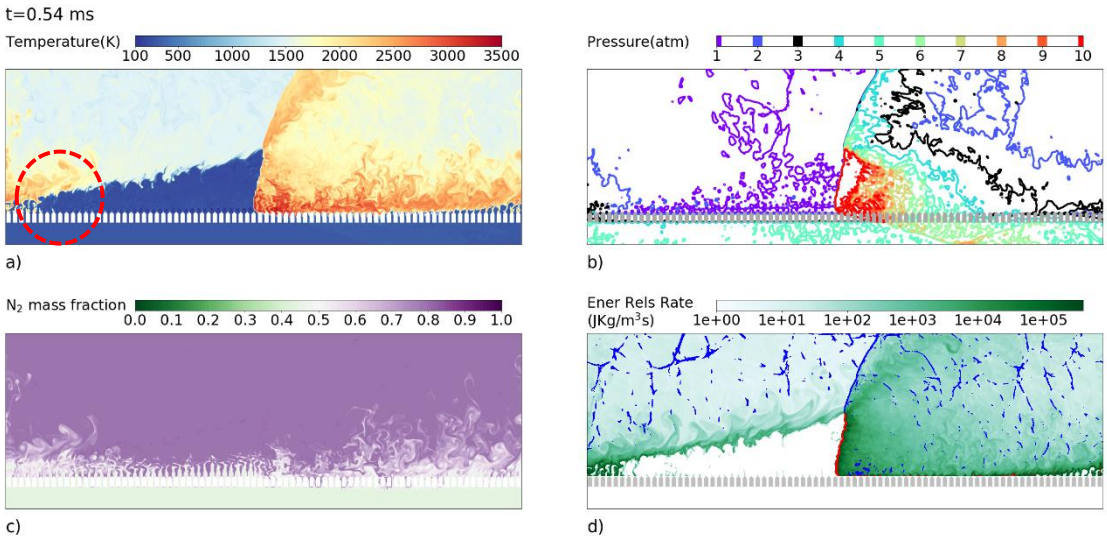

Fig. 3.3 Contours of temperature (a), pressure (b), N2 mass fraction (c) and energy release rate (d) showing DW acceleration, where the more reactive mixture entered the combustion chamber and the appearance of new hot spots (red circles).

As the DW traverses the RDE chamber, the pressure is observed to decrease in trailing regions farther away from the detonation front (Fig. 3.4). Due to the lower pressures, fresh mixture is admitted in these regions through supersonic jets impinging on the cloud of hot burnt gases. This results in the formation of intermingling finger-like structures of hot and cold gases as seen in Fig. 3.4(a) and (d)). These conditions are conducive to a deflagration-to-detonation transition (DDT), and are similar to the flame acceleration stages observed in other DDT studies [105-108]. In DDT simulations [109-111], the formation of a flame brush is followed by a corresponding increase in the total surface area of the flame and has been observed to lead to sudden flame acceleration and the transition to a detonation. Similarly, in the RDE combustion chamber, the mixing of hot burnt gases with cold incoming jets results in a pressure buildup and is highlighted using the red circles overlaid on the pressure iso-contours in Fig. 3.4(b). The red circles in Fig. 3.4(d) highlight the corresponding increase in the reaction rates, and hence the energy release rate in these mixed turbulent regions. A spherically expanding flame acceleration zone forms initially but is transformed to a horizontally propagating planar wave due to the absence of unburnt mixtures near

the top of the chamber. While the new mixture has not completely filled the combustion chamber (evident from N_2 contours in Fig. 3.4(c)), the newly formed hot spots are already observed to undergo merging, indicating these events occur over timescales that are very short when compared with the flow scales. The energy release rate in the flame merger region (Fig. 3.4 (c)) reaches levels comparable to the DW, indicating that a blast wave can form locally.

In the region where the flame merger is most aggressive, a sudden amplification in pressure is observed, and is visible as the red spot in the pressure and energy release rate contours (Fig. 3.4(b)). This high-pressure region further increases the rate of reactions, resulting in a local explosion. Note that since this *microdetonation* (MD) event occurs before the arrival of the primary DW, it can potentially develop into a second detonation. In contrast, at lower reactivities of the new mixture, the mixing of hot and cold jets might not lead to a detonation, if it occurs on a timescale greater than the arrival time of the primary DW. In that scenario, the mixed gases would be consumed by the primary DW, and no mode transition would be observed. Thus, mode transition is expected when the newly admitted fuel jets are of sufficient reactivity that the runaway process described above can occur over a timescale shorter than the time period of the primary DW. In Fig. 3.5 the development of the MD event into two new detonation fronts can be observed in the contours of temperature, pressure and energy release rate.

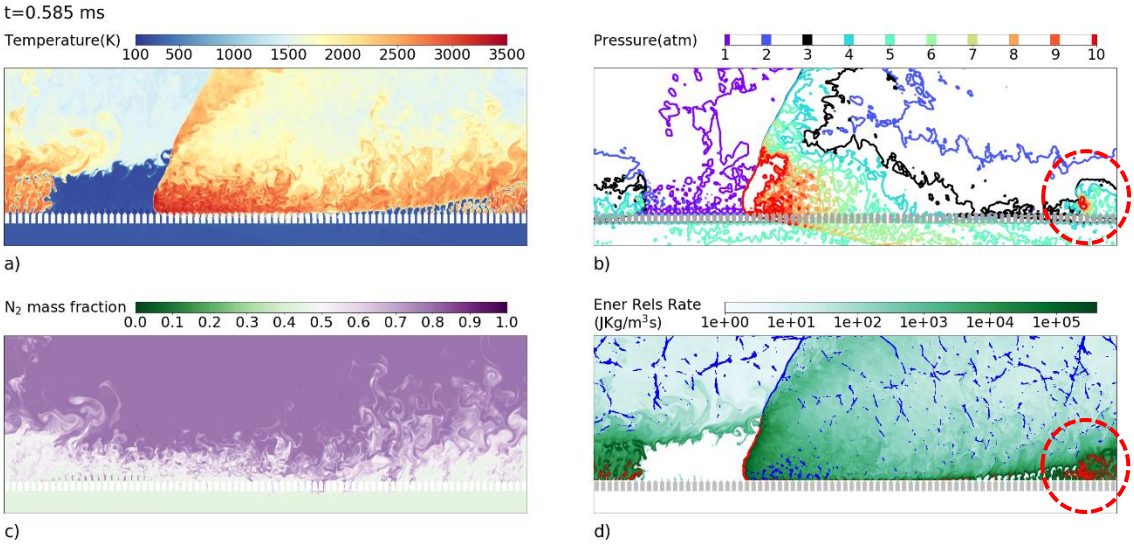

Fig. 3.4 Formation of finger-like structures of hot and cold gas jets. Pressure amplification due to mixing and the appearance of a local blastwave visible as a red spot in the pressure and energy release rate contours.

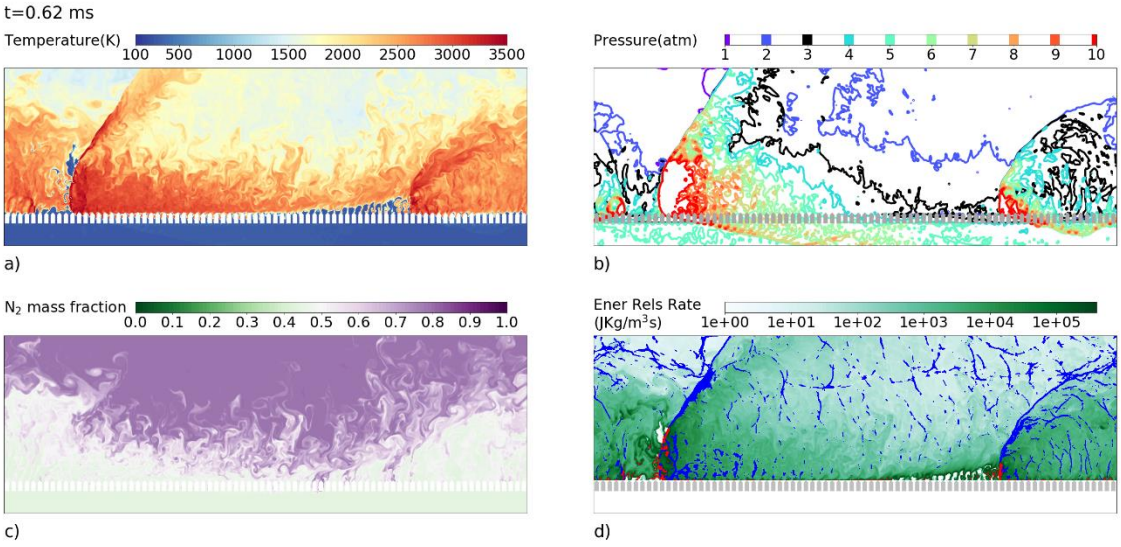

Fig. 3.5 At t = 0.62 ms, two microdetonations are observed in the pressure contours, in addition to the primary DW.

The above events are followed by a transient phase of mode transition, in which several additional detonation waves are formed, and propagate in either direction (Fig. 3.6). The microdetonations seeding these detonations grow and interact with the primary DW, while additional MD events might occur as more reactive mixture is admitted into the plenum.

Eventually, the newly formed waves undergo additional transformations as they split further or merge with other waves, eventually reaching a steady-state configuration with three detonation waves in this case (Fig. 3.7). In addition to the three DWs, significant regions of deflagration are observed in the regions ahead of the detonation fronts in Fig. 3.7 suggesting the system might have equilibrated to a higher number of waves for a more reactive mixture.

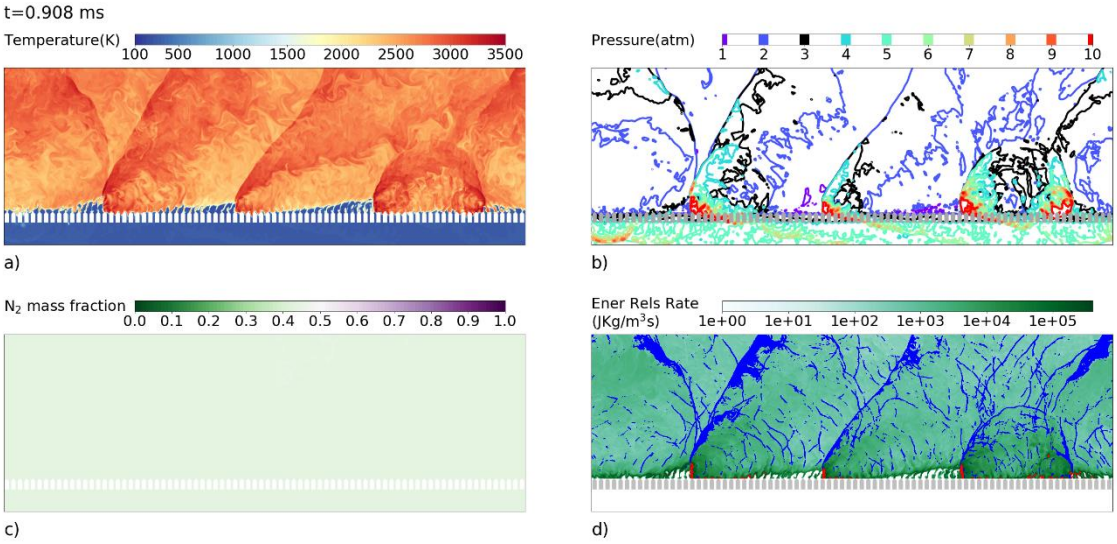

Fig. 3.6 Transient phase of mode transition characterized by formation and merger of multiple detonation.

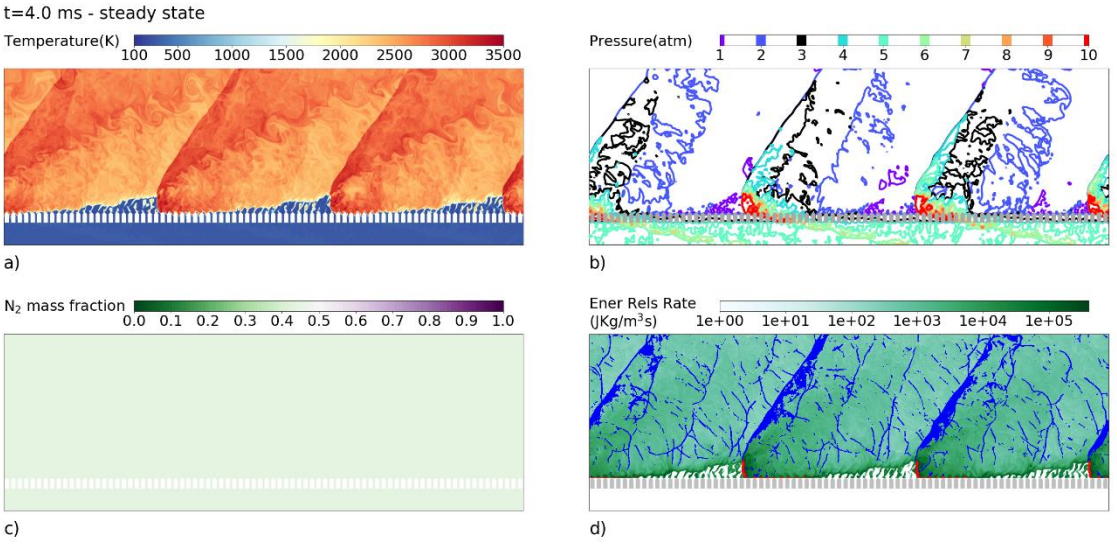

Fig. 3.7 At steady state following mode transition, three DWs are observed in the simulation in which the N2 concentration was varied from 5.0→1.0 moles.

3.2.3 Simulations with large perturbations in [N_2]:

In the simulations described in this section (cases 1-9), a large perturbation in [N_2] was always applied from an initial value of 5.0 moles. Thus, these simulations examine the stability of the terminal state of the RDE in each case without consideration of the specific path taken to achieve it. The questions of dependence on the perturbation size and path are addressed in the next section (case 10).

When [N_2] was changed from 5.0→3.5 moles (case 1), the mixture in the end state was not sufficiently reactive to trigger formation of a microdetonation. As a result, for this scenario no mode transition was observed (Fig. 3.8a), while the RDE continued to operate in one DW mode with slightly larger pre-burnt zones. For the remaining cases in Table 3, the end states were sufficiently reactive to trigger mode transition which followed the sequence of events described earlier: development of hot spots from vigorous mixing of reactive jets with burnt material, formation of microdetonations and intensification to a DW. Temperature contours from cases 4, 7, and 9 (corresponding to [N_2] transitions of 5.0→2.0, 5.0→0.75 and 5.0→ 0.0) are shown in Fig. 3.8 (b), (c), (d), and result in the formation of 2, 4 and 5 DWs respectively. Results from case 6, for an [N_2] variation of 5.0→1.0, which resulted in the formation of 3 DWs were already discussed in the last section, and are therefore not repeated here. Mode transition is accompanied by a reversal in the direction of propagation of the newly formed DWs in cases 4 and 9 (corresponding to [N_2]:5.0→2.0 and 5.0→0.0). The transient phase of mode transition involves formation, splitting and merging of several new DWs, and can be accompanied by a phase reversal in the direction of the newly formed waves in some cases.

In Fig. 3.9 and Fig. 3.10, we provide additional details of the events leading to mode transition in a specific case, viz. case 2 ([N_2]: 5.0→3.0). This case may be treated as being close to

a marginal stability limit for mode transition, and results in a delayed transition to a new detonation structure. This is in contrast to cases 3-9 in which the end states of [N_2] achieved by the perturbation were more reactive and led to the immediate transition in the number of DWs. In case 2 shown in Fig. 3.9, once the newly admitted reactive mixture completely filled up the combustion chamber, deflagration zones in the form of large finger-like structures of mixed hot and cold gases are visible in the temperature contours. Following a transient phase that lasted several cycles, a mode transition to 1 DW (Fig. 3.10) propagating in the opposite direction is observed. The simulations were not run to sufficiently late times to investigate the stability of the new configuration for this case. However, the initiation of a new microdetonation is seen in Fig. 3.10(b), which could develop into a second wave, or be consumed by the primary wave.

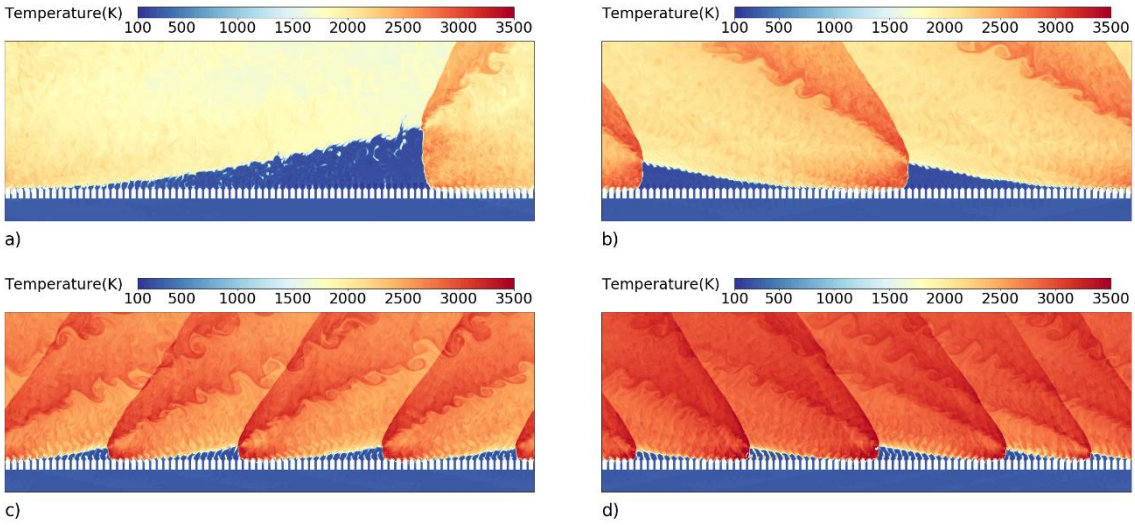

Fig. 3.8 Late-time plots of temperature contours from case 1 (a), case 4 (b), case 7 (c) and case 9 (d) leading to 1, 2, 4 and 5 DWs respectively.

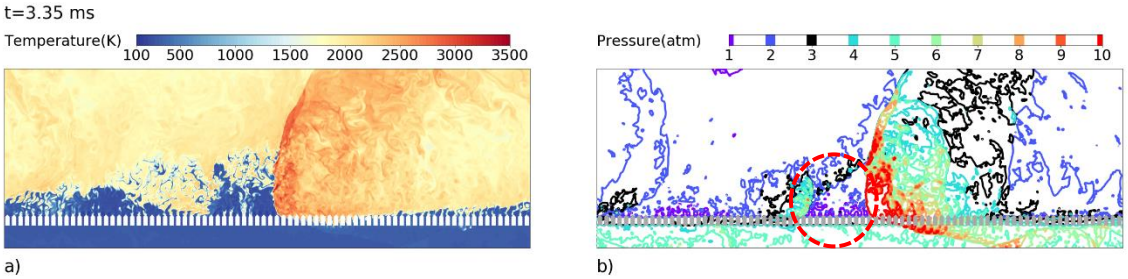

Fig. 3.9 Temperature and pressure contours from [N2]: 5.0→3.0 perturbation simulation (case 2) showing large deflagration structures that eventually transition to a weak detonation wave.

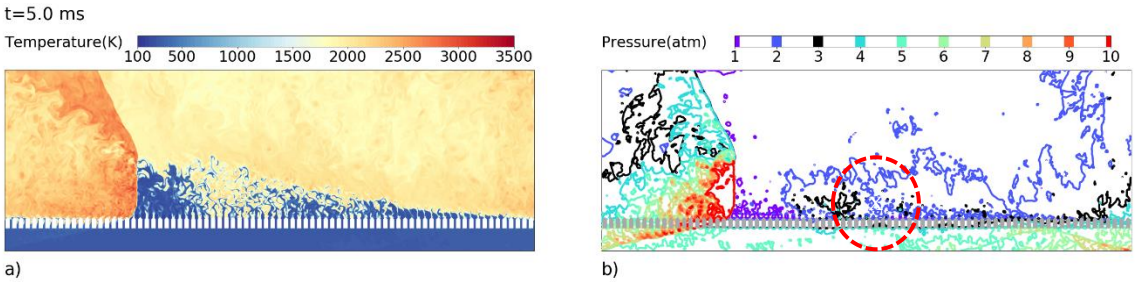

Fig. 3.10 Reversal in the propagation direction of the detonation observed in case 2 as a result of mode transition. This configuration is unstable, as seen in the formation of a new microdetonation in the pressure contours.

3.2.4 Simulations with decremental perturbations to [N_2]:

The simulation described in this section involved perturbations in [N_2] applied as a staircase function with a step size of 0.5. The purpose of the simulation is to investigate the effect of [N_2] perturbation trajectory on the mode number obtained following the change in N_2 concentration. This approach is similar to experiments [12] in which the N_2 concentration is often varied gradually. Consistent with the results discussed above, the perturbation [N_2]:5.0 → 3.5 did not lead to mode transition, since the inlet mixture was not sufficiently reactive in the perturbed state. When the number of moles of N_2 was decreased further from 3.5 to 3.0 (figure not shown), large deflagration zones appeared and led to the formation of a microdetonation, a transient phase that lasted for several cycles of revolution and eventually mode transition to 1 DW without phase reversal. As the [N_2] concentration was decreased further, the number of waves in each transitioned state differed for some cases from the observations in § C. Following [N_2] variation of 3.0 → 2.5

moles, the number of DWs increased to 2. In Fig. 3.11, we show the results of decreasing [N_2] from 2.0 to 1.5 moles (Fig. 3.11a) and then to 1.0 mole (Fig. 3.11b). The perturbations in these cases only resulted in an increase in the size of the hot spots observed in the triangular region of fresh mixture, but the RDE continued to operate in 2DW mode without mode transition. Two detonation waves were observed for these values of [N_2], in contrast to three waves observed in cases 5 and 6 for the same end states of [N_2]. The 2 DW system obtained here was found to be highly stable, so that for a variation of [N_2] moles as 2.5→2.0→1.5→1.0 did not alter the number of waves.

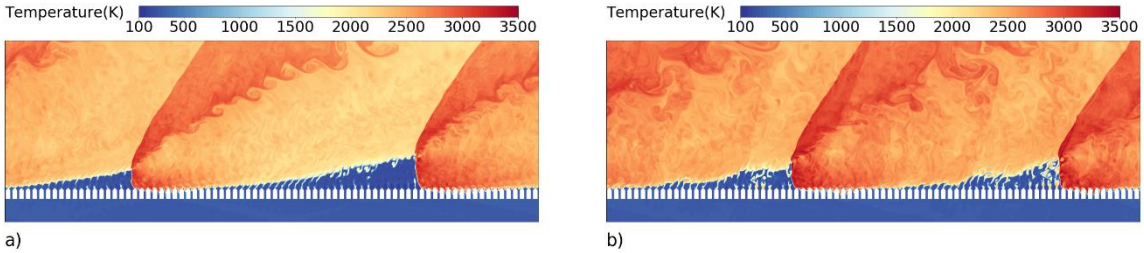

Fig. 3.11 Temperature contours from simulations with the following perturbations in [N2]: 2.0→1.5 (a) and (b) 1.5→1.0.

As the number of N_2 moles is further reduced to 0.5 (Fig. 3.12(a)), the mixture reactivity increases to a point at which large hot spots form and transition to a microdetonation before they can be swept up by the two primary DWs. The formation of this microdetonation finally breaks the 2DW system and triggers mode transition, leading to 4DWs in the eventual steady state (Fig. 3.12(a)), less than the five wave system reported in case 8 for 0.5 moles of N_2. This difference in the number of waves formed between simulations reported here and in the previous section suggest a dependence on the form of the perturbation function as well as the initial configuration. For the simulations shown in Fig. 3.12(a), the initial configuration had 1.0 mole of N_2 and 2 DWs, while case 8 was initialized with 5.0 moles and 1 DW. These dependencies suggest the final mode number is determined by the state of turbulent mixing, so that perturbations to the flow field can

produce ± 1 variation in end state mode number. These issues will be addressed in greater detail in future investigations. Finally, decreasing [N_2] from 0.5 moles to 0.0 moles (Fig. 3.12(b)) did not result in a mode transition. This is likely due to the corresponding modest increase in reactivity applied to a stable configuration of 0.5 moles of N_2 and 4 DWs.

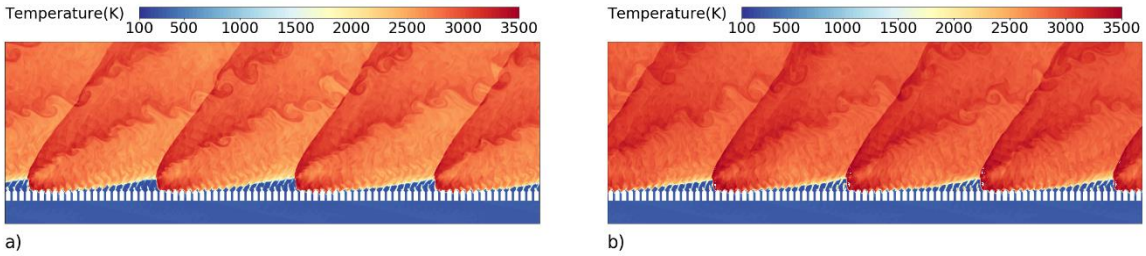

Fig. 3.12 Temperature contours from simulations with the following perturbations in [N2]: (a) 1.0→0.5 and (b) 0.5→0.0.

3.2.5 Summary of Mode transition mechanism

Fig. 3.13 shows the process of mode transition as observed in case 7, when the number of moles of N_2 in the injected mixture (x_{N2}) is decreased from 5 moles to 0.75 moles. The formation of the micro-detonation is taken as corresponding to $t = 0$ in these figures. As seen in Fig. 3.13(a), the entry of the fresh, more reactive mixture corresponding to x_{N2} = 0.75 moles is visible in the form of a dense array of hot and cold finger-like structures. Significant mixing occurs locally in this region, leading to enhanced reactions, culminating in the formation of a micro-detonation among the deflagrative structures. Note that in this case, since the timescale of formation of the micro-detonation τ_{MD} is less than the time of revolution τ_L of the parent DW, the micro-detonation is allowed to grow and transition into a second detonation wave in the system. From analyzing the simulations listed in Table 3, we found the condition $\tau_{MD}<\tau_L$ represented a necessary condition for mode transition in all the cases. We define the time of revolution of the parent wave as $\tau_L = L/V_D$, where L is the circumferential length, and V_D is the detonation wave speed, while a

methodology for estimating τ_{MD} is discussed in the next section. If the above condition is not satisfied, then the parent DW will consume the fuel mixture in the region of the hot spot, before it can transition into a micro-detonation and secondary wave. The flowchart in Fig. 3.13(b) summarizes the steps in the above mechanism to mode transition, while Fig. 3.13(c) shows through temperature contours, the transitioned end states from different simulation cases in which x_{N2} was perturbed by different amounts.

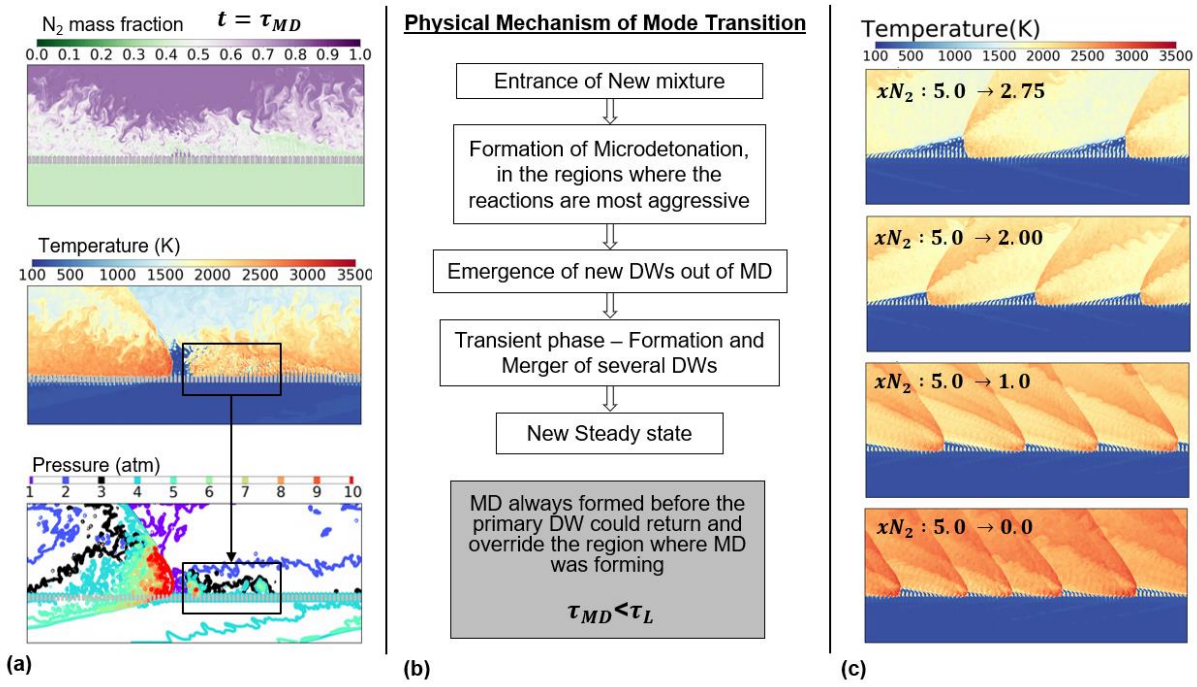

Fig. 3.13 (a) Formation of hot and cold, finger-like structures that seed hot spots which eventually transition to detonation waves (b) Flowchart showing sequence of events leading to mode transition (c) Temperature contours obtained at steady-state following mod

3.3 A simple model for mode transition

Results from the simulations described in Table 4 are used to develop a simple model for mode transition. Non-integer values of the mode number in the table correspond to averaged values from multiple simulation runs for the same initial conditions, differing only in the time ($\boldsymbol{\tau_{perturb}}$) at which the perturbation to the injected flow was applied. By varying $\tau_{\boldsymbol{perturb}}$ in the range 1 - 5

τ_L in these simulations, we have verified the observed mode transition mechanism and the proposed criteria are robust, and independent of the flow conditions present in the detonation chamber at the onset of inlet flow perturbation.

Table 4 List of RDE Simulations

$Case\ No.$	$x_{N2}\ \ of\ the\ new\ mixture$	$Number\ of\ detonation\ waves, nW$
$1a$	$5.0 \rightarrow 3.5$	1
$1b$	$5.0 \rightarrow 3.25$	1
$2a$	$5.0 \rightarrow 3.0$	1
$2b$	$5.0 \rightarrow 2.75$	2
$3a$	$5.0 \rightarrow 2.5$	2.33
$3b$	$5.0 \rightarrow 2.25$	2
$4a$	$5.0 \rightarrow 2.0$	2.8
$4b$	$5.0 \rightarrow 1.75$	3
$5a$	$5.0 \rightarrow 1.5$	3.66
$5b$	$5.0 \rightarrow 1.25$	$N.A$
$6a$	$5.0 \rightarrow 1.0$	4.2
$7a$	$5.0 \rightarrow 0.75$	4
$8a$	$5.0 \rightarrow 0.5$	4.2
$8b$	$5.0 \rightarrow 0.25$	4.33
$9a$	$5.0 \rightarrow 0.0$	4.66

Estimation of $\boldsymbol{\tau_{MD}}$ from simulation data:

The proposed criteria was validated using simulation data spanning a wide range of conditions, and the results of this analysis will be presented in the full paper along with a predictive model for the number of detonation waves for a given perturbation to the inlet flow conditions. Here, we briefly describe our methodology for computing τ_{MD} , the timescale for the growth and transition of a local hot spot into a detonation wave. We obtain τ_{MD} in our simulations as the timescale over which the peak pressure within the hot spot increases from the choking pressure p_{chk} to the CJ pressure p_{CJ}. The peak pressure relevant to the hot spot was obtained by tracking a

moving window of dimensions 6 cm x 3 cm in the (x, y) directions, and centered around the hot spot.

To reduce noise in the peak pressure timeseries, data from multiple micro-detonation events were averaged after timeshifting, by aligning the times at which the CJ pressures were reached in each case (more details in Appendix § C). Simulation results from multiple cases plotted in Fig. 3.14 (a) show the pressure within the hot spot increases according to $p(t) = At^n$, consistent with the formation of a self-similar detonation wave. From this data, the timescale τ_{MD} is obtained as the time required for the peak pressure to increase from the choking pressure to the CJ pressure. In Fig. 3.14(b), we compare τ_{MD} with τ_L obtained from the FLASH simulations for different inlet flow conditions. In Fig. 3.14(b), data from simulations at different xN_2 are used to obtain a linear fit for τ_{MD} in the range $xN_2 \in (0,2.5)$.

$$\tau_{MD}(xN_2) = 34.49\, xN_2 + 35.44,\ xN_2 \in (0,2.5) \tag{3.1}$$

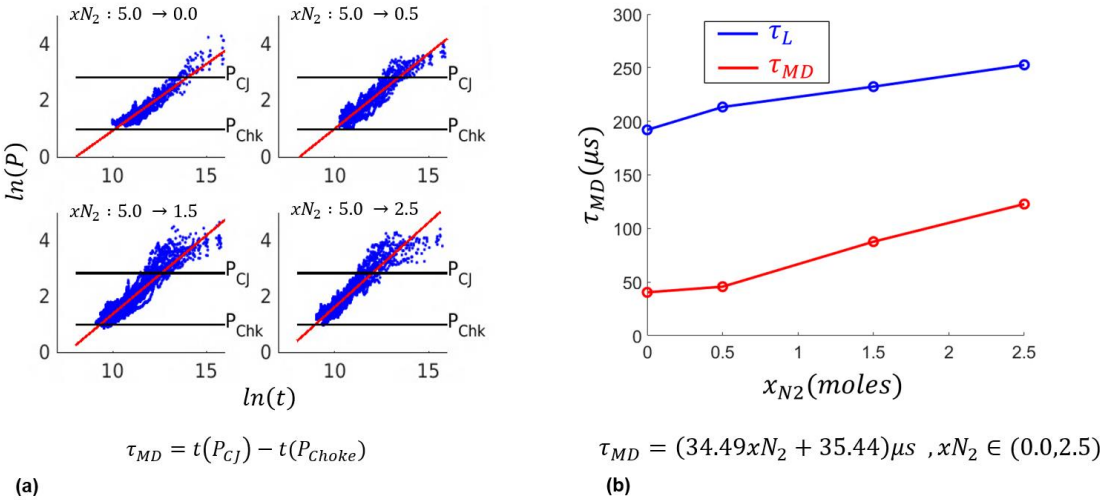

Fig. 3.14 (a) Estimation of τ_{MD} from timeseries data of peak pressure within the hot spot region (b) Comparison of the micro-detonation timescale with the times of revolution of the parent wave from multiple simulations.

Based on the above observations, we propose a simple relationship to predict the number of DWs following mode transition. As discussed earlier, for mode transition to occur, the time required for micro-detonation to form, τ_{MD}, must be less than the time required for the parent DW to complete one revolution, τ_L, i.e. $\tau_{MD}<\tau_L$. If this condition is not satisfied, the unreacted mixture around the hot-spot will instead be consumed by the parent DW. We propose that if $\tau_{MD}<\tau_L$, the number of DWs following mode transition is given by:

$$nW = round\left(\frac{c\tau_L}{\tau_{MD}}\right), c \leq 1 \tag{3.2}$$

In eq. (3.2), all the variables are obtained at the new steady state condition after mode transition, while c is a coefficient that represents the ratio of number of unblocked fuel injectors to the total number of fuel injectors. For instance, in the high-pressure region behind the DW, a fraction of fuel injectors are blocked from injecting fresh fuel into the combustion chamber, and c ~0.75 in this region. The time-to-detonation τ_{MD} is a function of the fuel reactivity, which in this work is varied through the N_2 concentration of the injected mixture. For different N_2 dilution of the injected mixture, we obtain τ_{MD} from the linear fit given in eq. (3.1). Fig. 3.15shows the comparison between eq. (3.2) and simulation results, where "Simulation-Avg" correspond to data points obtained by averaging over multiple simulations, with the multiple simulations differing only in the time at which new mixture was injected (the N_2 dilution in the new injected mixture was kept the same in the simulations); Also, in Fig. 3.15, datapoints labeled "Simulation" represent data obtained from individual simulations without averaging. From Fig. 3.15, it can be seen that the number of waves obtained following mode transition in our simulations is in good agreement with the relationship proposed in eq. (3.2).

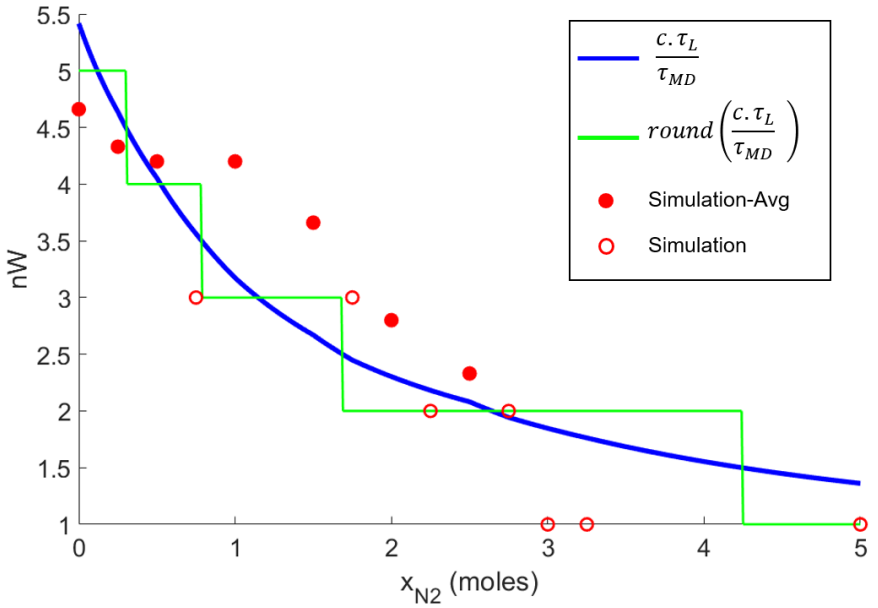

Fig. 3.15 Comparison of the micro-detonation timescale with the times of revolution of the parent wave from multiple simulations.

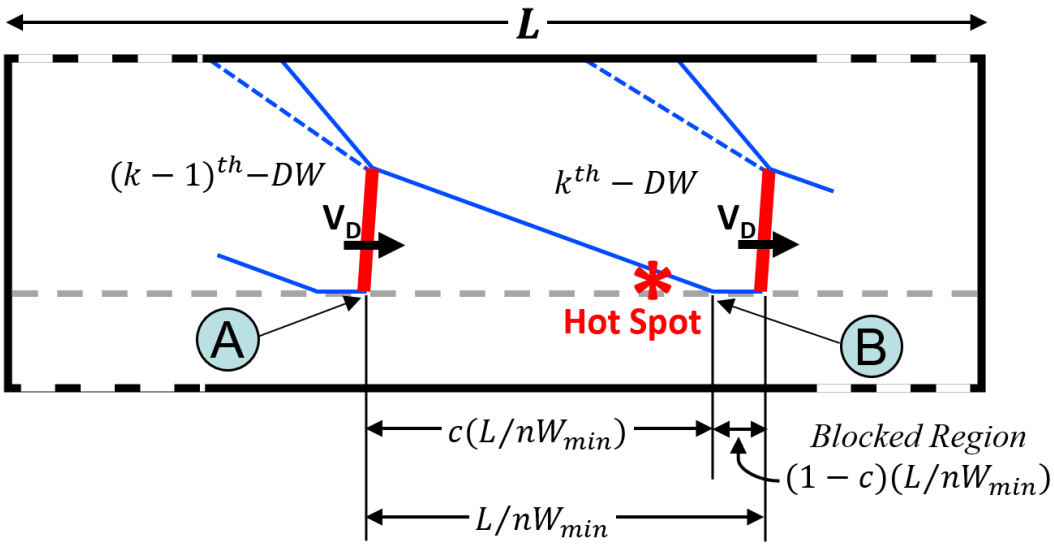

Fig. 3.16 Estimation of τ_{MD} from timeseries data of peak pressure within the hot spot region

Fig. 3.16 shows the mechanism by which eq. (3.2) predicts the number of detonation waves formed nW. Following a mode transition event from a given number of DWs, we may assume a new stable state is established, requiring a minimum of DWs nW_{min} to ensure that no new hot

spots form. Thus, assuming that all DWs are identical, then we require that following the formation of the k^{th} DW, $\tau_{MD} > t_{AB}$, where t_{AB} is the time required for the $(k-1)^{th}$ DW to travel the distance $c(L/nW_{min})$, and τ_{MD} is the formation time for a new microdetonation. This condition ensures that the hot-spot (formed behind the k^{th} DW) is consumed by the $(k-1)^{th}$ DW arriving at that point, before it can use the unreacted mixture available around it to form a new micro-detonation. Since $t_{AB} = cL/(V_D.nW_{min}) = c\tau_L/nW_{min}$, we can write this condition as

$$\tau_{MD} > c\tau_L/nW_{min}. \tag{3.3}$$

Conversely, since τ_{MD} is fixed for a given N_2 dilution of the newly injected fuel mixture, for a system with $(nW_{min}-1)$ DWs, the time-of-revolution would increase to $t_{AB} = cL/(V_D(nW_{min}-1)) = c\tau_L/(nW_{min}-1)$, resulting in $\tau_{MD} < t_{AB}$, so that a hot spot formed behind the k^{th} DW will transition into a micro-detonation before the $(k-1)^{th}$ DW can arrive:

$$\tau_{MD} < c\tau_L/(nW_{min}-1) \tag{3.4}$$

Combining, eq. (3.3) and eq. (3.4) gives

$$c.\tau_L/nW_{min} < \tau_{MD} < c\tau_L/(nW_{min}-1) \tag{3.5}$$

$$(nW_{min}-1) < (c\,\tau_L/\tau_{MD}) < nW_{min} \tag{3.6}$$

$$nW_{min} = round\left(\frac{c\tau_L}{\tau_{MD}}\right) \tag{3.7}$$

Thus, eq. (3.7) gives the minimum number of DWs that should form after mode transition.

3.4 RDE Thrust analysis

In Fig. 3.17, we plot time series plots of thrust, mass flow rate and the specific impulse from cases 9 (5.0→0.0), case 2 (5.0→3.0) and case 1 (5.0→3.5). These quantities were computed as follows:

$$F_R(t) = \int_{\partial\Omega} [\rho v^2 + (p - p_b)] \, \mathrm{dA} \tag{3.8}$$

$$\dot{m}_R(t) = \int_{\partial\Omega} \rho_R v \, \mathrm{dA} \tag{3.9}$$

$$I_{sp}(t) = \frac{F(t)}{g_0 \dot{m}_R(t)} \tag{3.10}$$

In eqs. (3.8)-(3.10), F_R is the total thrust produced by the RDE, which includes both the momentum thrust and the pressure thrust, represented by the first and second terms on the right hand side of eq. (3.8); $\dot{m}_R$ is the total mass flow rate of the fuel mixture (H_2, O_2 and N_2) injected from the bottom boundary of the RDE; I_{sp} is the specific impulse of the engine which is calculated by dividing the total thrust F_R by the total mass flow rate $\dot{m}_R$. The above parameters are calculated at the exit boundary of the RDE, with an assumed difference in the radius of inner and outer annulus of RDE of 1cm, and a cross sectional area A of 48 cm^2. The transient phase of mode transition is visible in these plots, marked by short bursts of large fluctuations in these quantities. For example, for case 9, the fluctuations are observed at ~1 ms, while similar fluctuations were observed in the corresponding time series for cases 3-8. Following the transients, the RDE equilibrates to a new steady state with a change in *nW*, and is visible in the plots in Fig. 3.17 as a quiescent stage (after ~2 ms in case 9). Similarly, for case 2, when the N_2 dilution is changed to 3.0 moles, several weak local explosions are observed which last for several revolutions of the primary DW, followed by a microdetonation of moderate strength and mode transition. Once again, the formation of the microdetonation is marked by a significant spike in the time series plots of the above quantities at ~4 ms. In contrast to case 9, these fluctuations persist in case 2 even after the mode transition, and correspond to additional microdetonations which might have led to further transitions in *nW* had the simulations extended to later times. Finally, no local explosions were

observed in case 1 signifying the absence of mode transition, and evident in the time history of key quantities in Fig. 3.17 which remain flat.

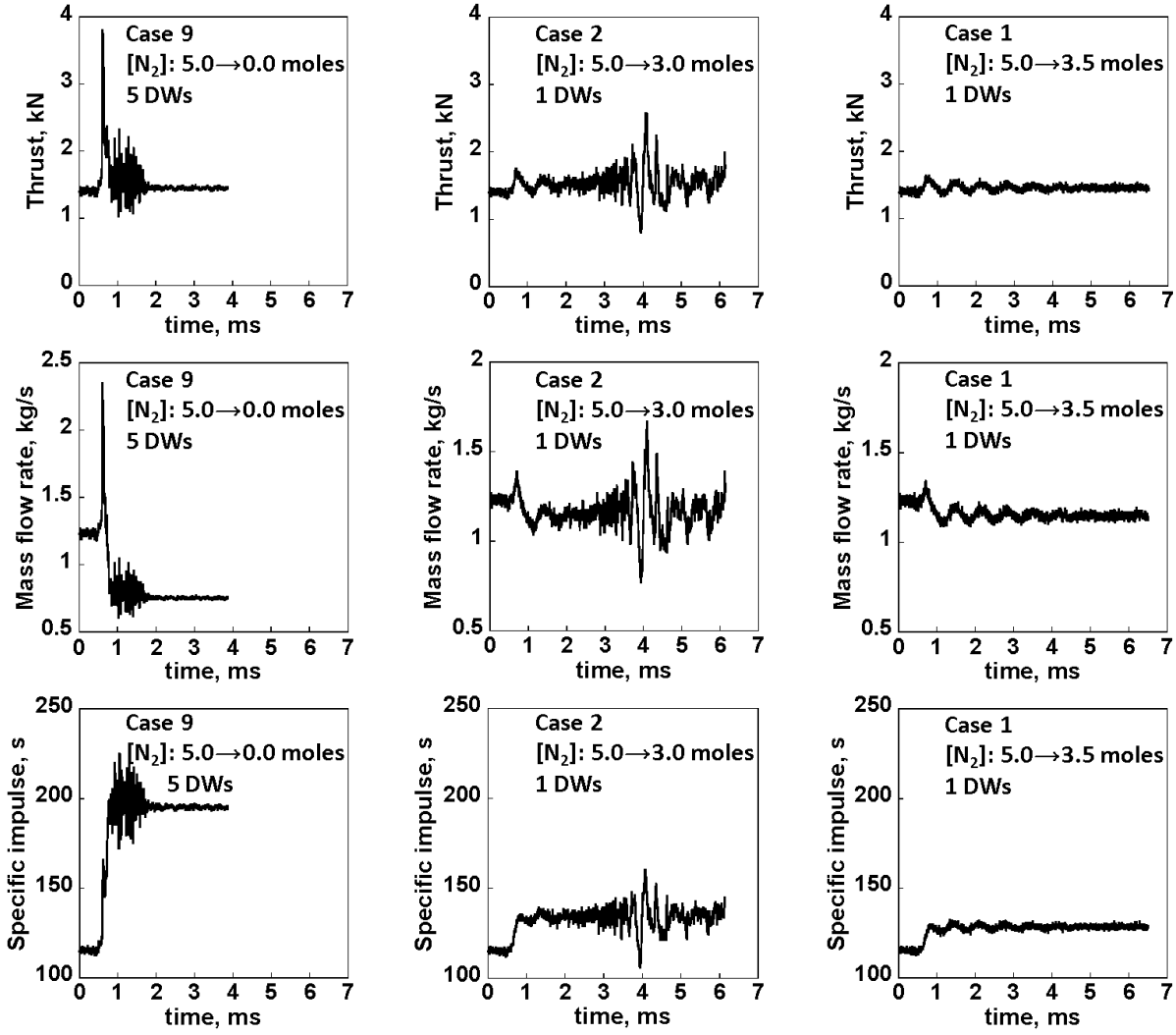

Fig. 3.17 Time series plots of thrust, mass flow rate and specific impulse from cases 9, 2 and 1.

In Fig. 3.18, the variation of engine performance parameters with N_2 reactivity is plotted for cases 1-9. We find the thrust varies weakly with N_2 dilution, in spite of accompanying changes to the detonation mode number discussed earlier. While an increase in fuel reactivity (i.e. decrease in N_2 concentration) should result in an increase in thrust, this effect is countered in our simulations by two countervailing factors: first, the total mass flow rate is reduced (Fig. 3.18(b)) with the

decrease in N_2 concentration, while the fraction of less efficient, deflagrative combustion increases. We discuss these issues in greater detail below.

The mass flow rate in the simulations can be approximated from the isentropic, choked mass flow equation (eq. (3.11)). At the fuel mixture injection boundary, the temperature is <= 300K, so that the ratio of specific heats γ of the inlet mixture can be taken as ~ 1.4 corresponding to a diatomic gas. For all the cases, P_0, T_0, and γ remain fixed, while the average molecular weight $\bar{W}$ of the mixture will decrease with decreasing [N_2]. Therefore, the mass flow rate should decrease with N_2 concentration according to

$$\dot{m} = \frac{A\,P_0}{\sqrt{T_0}}\sqrt{\frac{\gamma\,\bar{W}}{R_u}}\left(\frac{\gamma+1}{2}\right)^{-\frac{(\gamma+1)}{2(\gamma-1)}}. \tag{3.11}$$

From the above equation, the ratio of choked mass flow rates at 0.0 and 5.0 moles of N_2 is 0.75. In comparison, from the mass flow rates plotted from FLASH simulations in Fig. 3.18(b), the ratio of mass flow rates between 0 and 5 moles of N_2 is 0.62. These trends in combination with the tendency toward more deflagrative combustion at higher fuel reactivity leads to a modest variation in the total thrust. The increase of total mass flow rate with the N_2 concentration, while maintaining a nearly constant engine thrust results in a decrease in the specific impulse of the RDE in Fig. 3.18(c). Finally, the Chapman-Jouget velocity V_{CJ} (blue markers in Fig. 3.18(d)), obtained from 1D detonation tube simulations using the multi-step reaction mechanism, decreases with increase in N_2 concentration. This is in agreement with the theoretical V_{CJ} trend obtained for a single γ, single-step reaction mechanism, which predicts a decrease of V_{CJ} with decreasing energy density of the fuel. The 1D detonation tube simulations were performed at 1 atm and 300 K, and closely resemble the conditions ahead of the DWs in RDE in our 2D simulations. Contrary to the stagnant and uniform conditions in the 1D simulations, the flow field ahead of the DW in the 2D

RDE simulations had a velocity fluctuation of ~300m/s and contains hot patches of burnt mixture. Together, these factors render the detonative burning non-uniform and less efficient, due to which the DW velocity V_D from the 2D RDE simulations (black curve in Fig. 3.18(d)) is lower than that obtained from the corresponding 1D simulations (V_{CJ}).

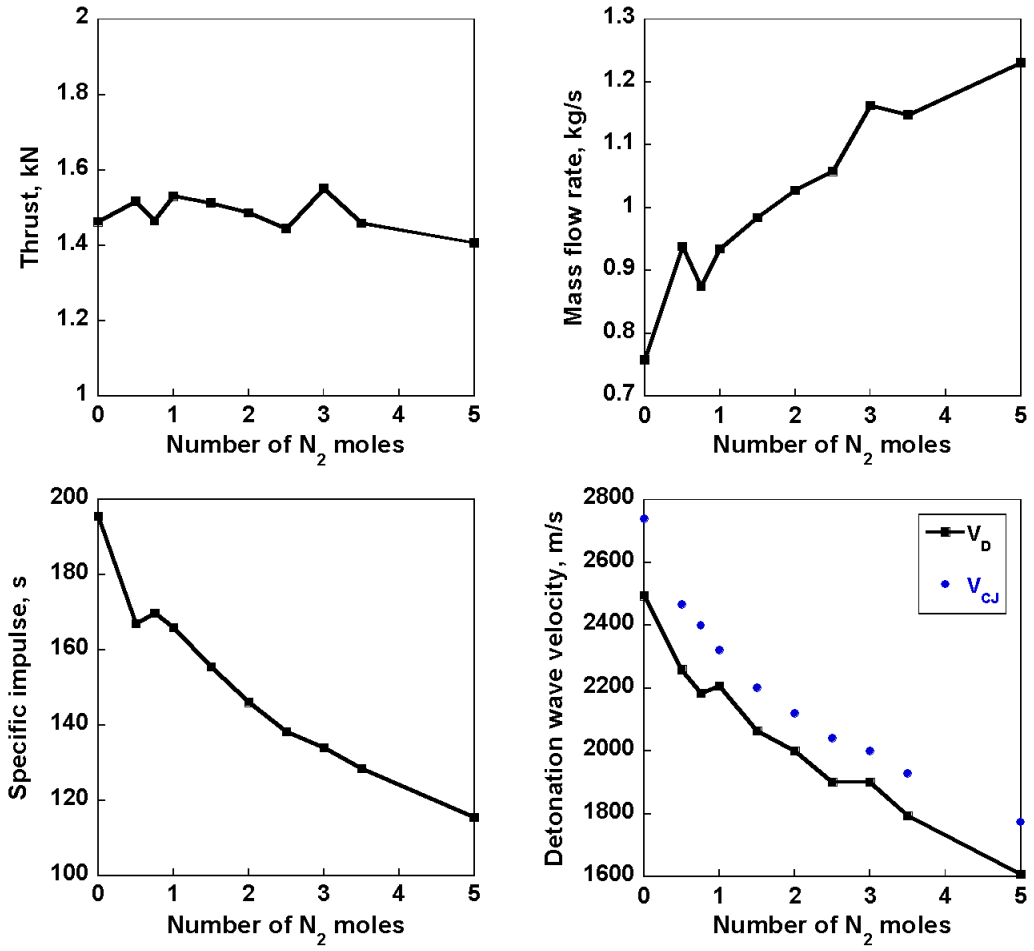

Fig. 3.18 Variation of engine performance parameters with fuel reactivity (cases 1 – 9).

Time series plots of the total thrust, mass flow rate and specific impulse from case 10 are shown in Fig. 3.19. Note that in case 10, the [N_2] perturbation trajectory followed the pathway (5.0→3.5→3.0→2.5→2.0→1.5→1.0→0.5→0.0 moles). In Fig. 3.19, large amplitude spikes in time series plots of thrust, mass flow rate and specific impulse, are observed only at $\sim 7\ ms$ and $\sim 19\ ms$, corresponding to mode transitions from 1 DW to 2 DW ([N_2]: 3.0 → 2.5 moles) and from

2 DW to 4 DW ($[N_2]$: 1.0 → 0.5) respectively. The weak fluctuations observed elsewhere in Fig. 3.19, for instance following the variation of $[N_2]$ from 3.5 moles to 3.0 moles at ~ 4 ms are due to the formation of local explosions, similar to those observed in case 2. It is not clear if the absence of mode transition at other values of $[N_2]$ was due to the next perturbation in fuel reactivity being applied before the transients could be replaced by a new steady state with a different number of modes. The variation of different engine performance parameters (thrust, specific impulse, mass flow rate and detonation velocity) with $[N_2]$ is shown in Fig. 3.20 for case 10. Similar to Fig. 3.18, the total thrust is weakly dependent on the fuel reactivity, while the mass flow rates are observed to increase. This results in an increase in the specific impulse as the fuel reactivity is reduced. Finally, the similarity in qualitative trends between Fig. 3.18 and Fig. 3.20 suggests the behavior of engine parameters are independent of the path taken in reaching a specific fuel reactivity value.

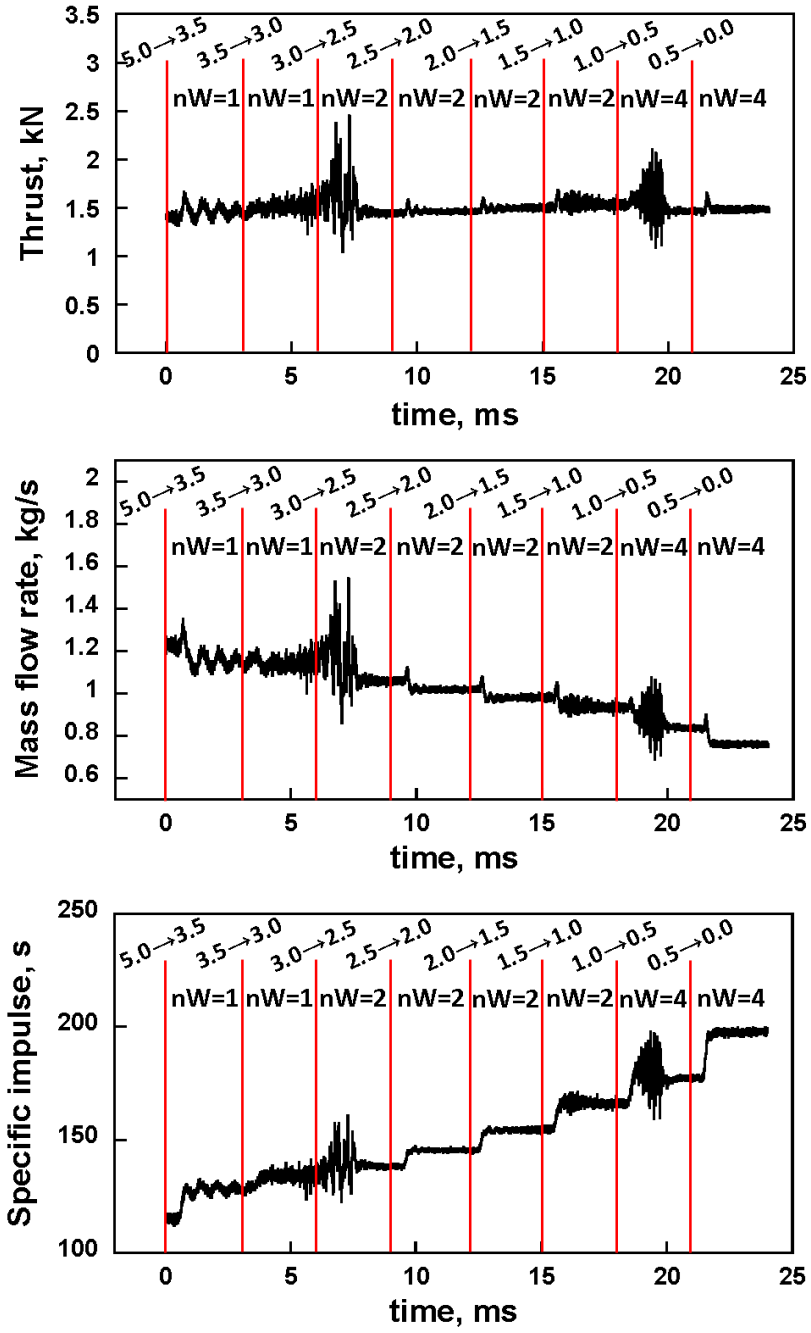

Fig. 3.19 Time series plots of thrust, mass flow rate and specific impulse from case 10.

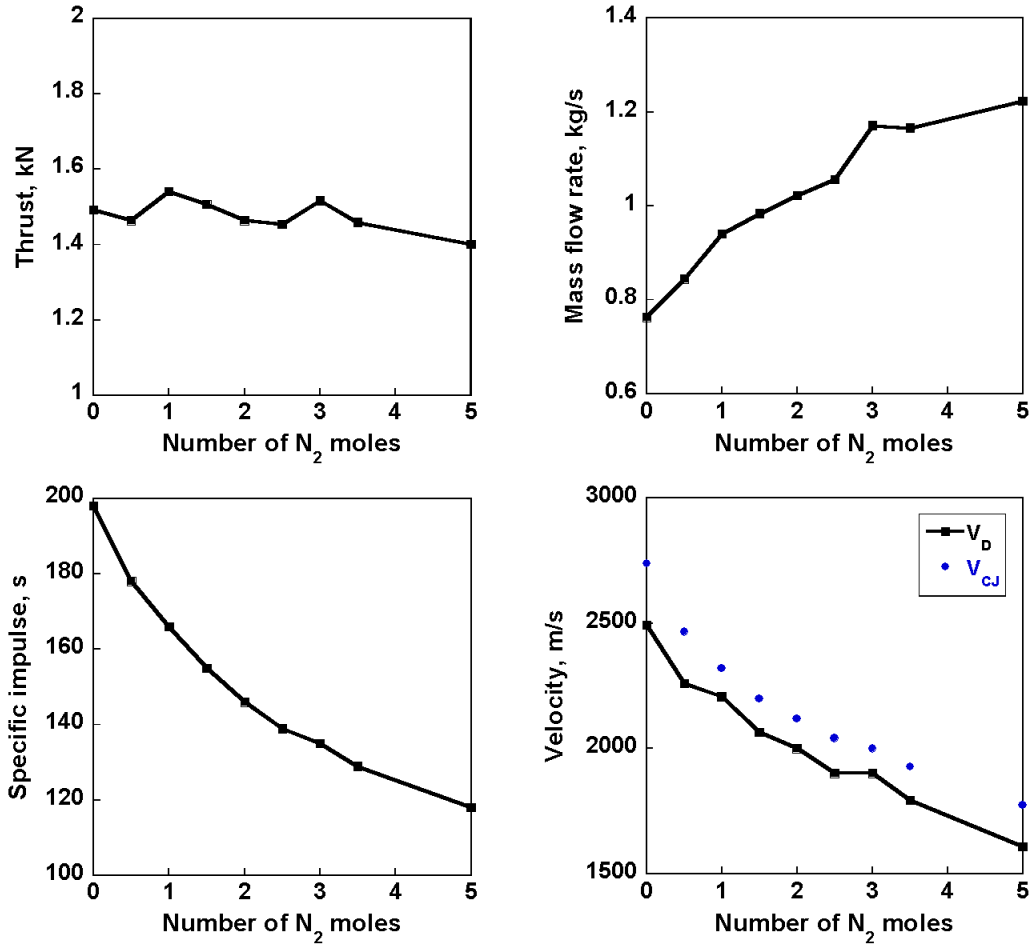

Fig. 3.20 Variation of engine performance parameters with fuel reactivity from case 10.

CHAPTER 4: NUMERICAL SIMULATIONS OF A SHOCK-DRIVEN LIQUID FUEL DROPLET

4.1 Simulation setup

Fig. 4.1 shows a schematic of the simulation setup for the 2D axisymmetric fuel droplet under high Mach number shock conditions simulated in this work. With the exception of the axis of symmetry, all boundaries were modeled as zero gradient surfaces. The use of preheated liquid fuel and preheated oxidizer is known to increase the combustion efficiency in detonation engines [26, 112, 113]. Therefore, in all the simulations, a $5\mu m$ liquid $n-Dodecane$ droplet at a preheated temperature of $460\ K$ was used, while the gas phase consisted of pure O_2 at $1\ atm$ pressure and $700\ K$ preheated temperature. The droplet was impacted by a Mach 5 shock, and the post-shock flow resulted in a Weber number of 500. Under the extreme conditions encountered under a Mach 5 post-shock flow, the droplet deforms, evaporates and can also autoignite. To isolate the effect of evaporation and reactions on the droplet deformation, three different cases were simulated which are labeled as Inert (non-reacting, non-evaporating), Evaporating (non-reacting) and Reacting. For all three cases, the 2D droplet was initialized with a layer of fuel vapors of thickness $0.05D$ to minimize initial impulsive evaporation. For all the simulations, a mesh resolution of 512 cells per diameter (CPD) was used. Finally, a non-dimensional time $t^* = \frac{t}{\tau}$ is defined [114], where $\tau = \frac{D}{u_{g,ps}}\sqrt{\frac{\rho_l}{\rho_{g,ps}}}$ and $u_{g,ps}$ and $\rho_{g,ps}$ are post-shock gas velocity and density respectively.

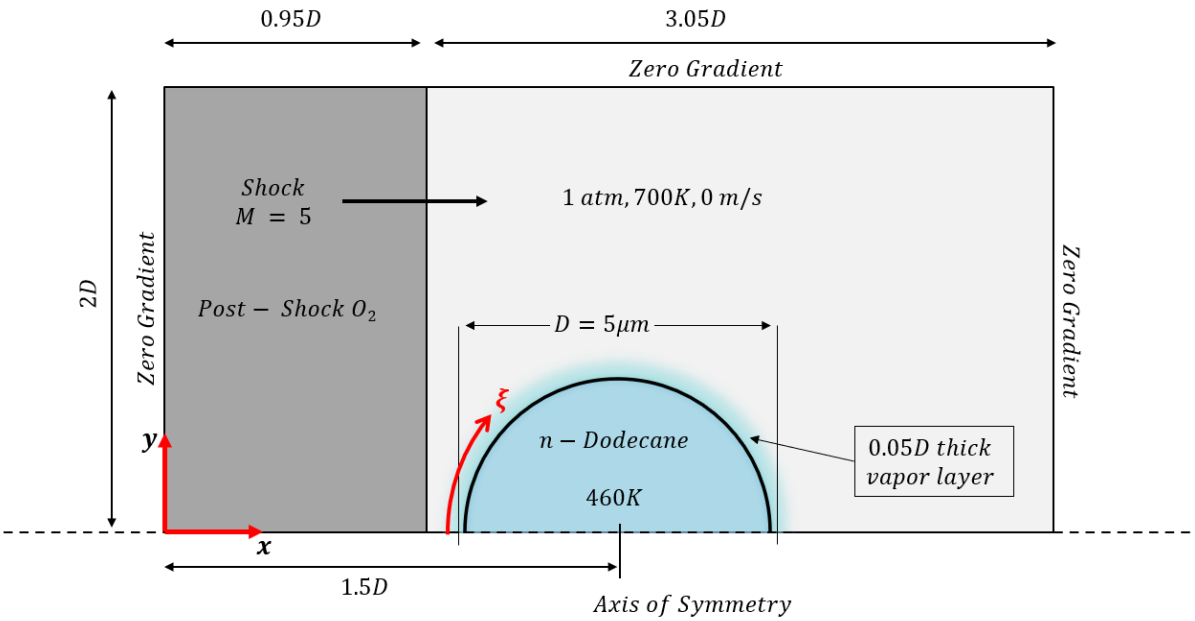

Fig. 4.1: Schematic for 2D, axisymmetric shock-droplet simulations.

4.2 1D simulations of a gas-liquid interface

We first describe 1D simulations of a gas-liquid interface, under conditions corresponding to the post-shock states of the shock-droplet problem described in §2.4. The purpose of these simulations is to analyze the evaporation, reaction and heat conduction processes at the gas-liquid interface, in the absence of the effects of the complex, deforming droplet geometry. The simplified 1D setup is shown in Fig. 4.2, and involves a domain of length $5.5D$, while the liquid phase region occupies a length of $0.5D$. The initial pressure and temperature in the gas phase (Fig. 4.2) were taken to match the post-bowshock conditions observed in the 2D, Mach 5 shock-droplet interaction problem (§2.4), while the liquid region was preheated to $460\ K$. A mesh resolution of 1280 cells per diameter, with $D = 5\mu m$ was used in the 1D simulations.

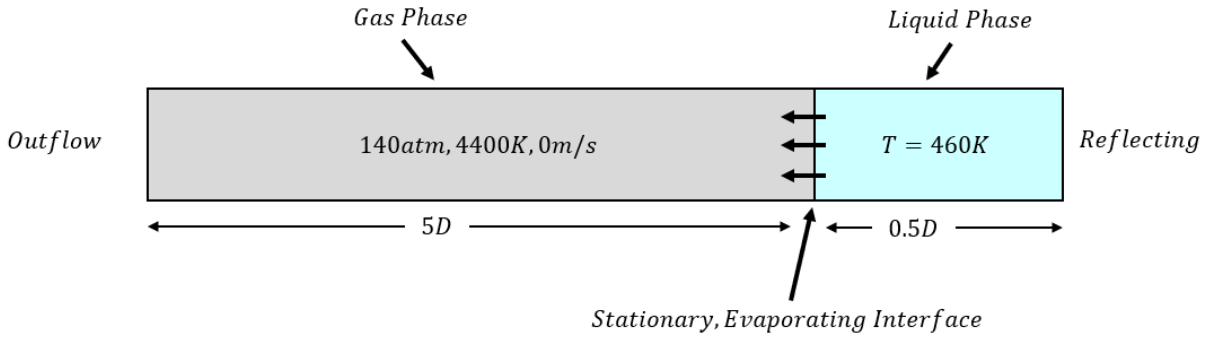

Fig. 4.2: Initial conditions and problem setup for 1D liquid evaporation into a post Mach 5 reflected shockwave flow field.

The corresponding fuel and product mass fraction profiles are shown in Fig. 4.3 (b). The observed peak in temperature profile Fig. 4.3 (a), and the presence of high mass fraction of reaction products $\left(Y_{prod}\sim 0.6\right)$, indicates the reactions have progressed significantly, under these high pressure and temperature conditions. Defining the flame location as the x-location of the maximum rate of reaction, we obtain $\frac{x_{flame}}{D}\sim -0.16$ for the 1D simulations shown here (Fig. 4.3). The flame location is thus closer to the cold droplet surface than the temperature peak which occurs at $\frac{x}{D}\sim -0.15$, since the reaction rate depends both on the temperature and the fuel mass fraction (eq. (2.13)) with the latter reaching a maximum concentration at the interface $\left(\frac{x}{D}=0\right)$. The reactive simulation (Fig. 4.3 (b)) shows almost complete consumption of the fuel vapors, with Y_{fuel} dropping to ~ 0.001 for $\frac{x}{D}<-0.3$, indicating that the reactions are primarily limited by the production of fuel vapors through evaporation. The relatively high value of product mass fraction at the interface (only $\sim$10% less than its peak value), is attributed to diffusion from the flame site, since the interface film temperature is not high enough to sustain reactions.

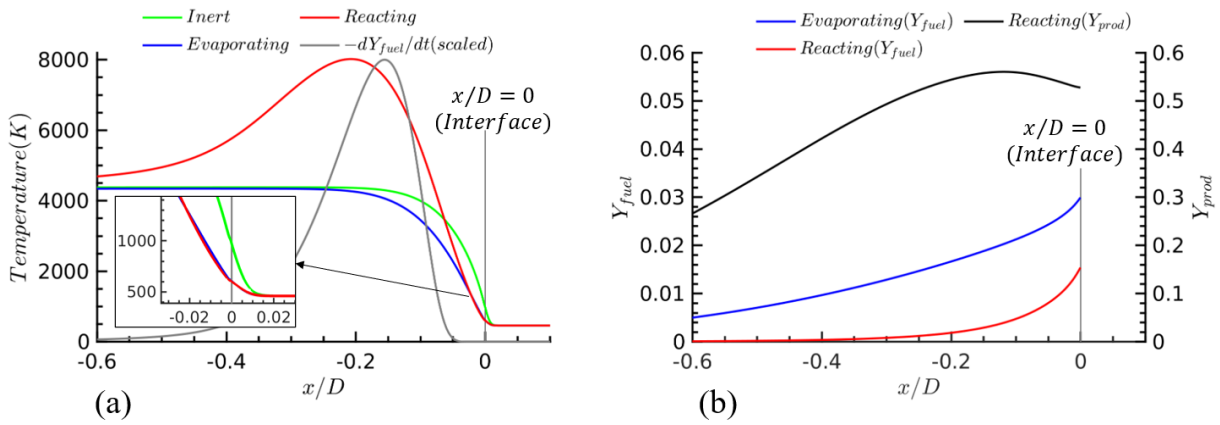

Fig. 4.3: x-profiles of (a) Temperature, (b) fuel- and product mass-fractions from 1D inert, evaporating, reacting simulations at $t^* = 0.25$. Interface is initially located at $x/D = 0$.

The corresponding time evolution of the film temperature and evaporation mass flux at the interface are shown in Fig. 4.4 (a) - (b). At $t^* = 0$, the temperature gradient between the liquid and gas phase is theoretically infinite, resulting in an impulsive heat transfer, following which the film temperature rapidly reaches a steady state by $t^* \sim 0.02$. The film temperatures in the evaporating and reacting droplet cases are lower than in the inert simulation, due to convective cooling by the fuel vapors and blow-off from Stefan flow of incoming hot post-shock gasses which substantially reduce the liquid interface heating. As the film temperature gradually decreases by $\sim 60\ K$ over a time of $t^* = 0.25$, the corresponding saturation pressure drops from $18\ atm$ to $8\ atm$; as a result, the evaporative mass flux, which is proportional to the saturation pressure, continues to decline significantly. The decline in the mass flux is also driven by the gradual buildup of fuel vapor concentration adjacent to the interface.

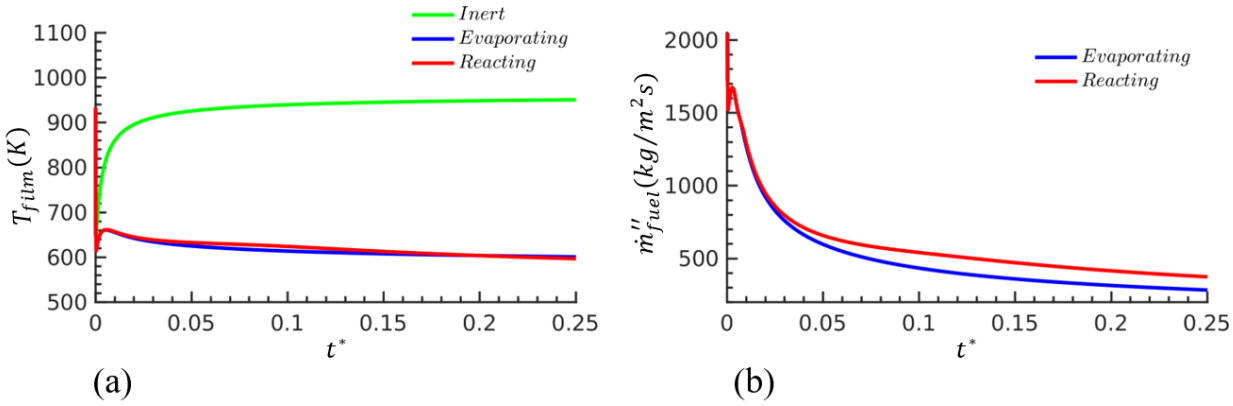

Fig. 4.4: Time evolution of (a) the film temperature and (b) evaporation mass flux evolution at the 1D gas-liquid interface for the inert, evaporating and reactive cases.

4.3 Mach 5, We=500, 5μm shock-droplet interaction

4.3.1 Droplet surface morphology:

In this section, we present results from simulations of a notional $n-Dodecane$ fuel droplet, impacted by a Mach 5 shock under surrounding conditions that could be relevant to detonation engine operation. The simulations were run to a time $t^* = 1.0$, which we take to represent a nominal breakup time as suggested in [??-Need to find this reference]. Numerical Schlieren images from the Mach 5, 5μm ($We = 500$) droplet simulations are shown in Fig. 4.5 for the inert, evaporating and reacting cases at different time instances. At early times ($t^* = 0.02$, Fig. 4.5 (a)), the shock locations and droplet shapes are similar in all three cases. The appearance of KH instability waves at the droplet surface can be seen in all three cases by $t^* = 0.25$ (Fig. 4.5b). By $t^* = 0.5$, the colder fuel vapors generated in the evaporating and reacting cases are visible as the darker regions in Fig. 4.5(c), while a diffusion flame is seen in the reacting case (shown in the inset) located at $\frac{x}{D} \sim -1.2$. The expansion of gas mixture in the windward side of the reacting droplet displaces the upstream bowshock away from the droplet, relative to the inert and evaporating droplets.

At $t^* = 0.5$, while differences in the droplet surface morphology increase, the bulk structure is largely similar between the three cases, and includes a flattened droplet core attached to a thin and elongated sheet at the equator. The thin sheet at the equatorial region appears to be formed from an impulsive ejection mechanism, that occurs as a result of the large velocity difference between the windward and leeward sides immediately following shock impact. The variations in liquid phase density remained negligible throughout the simulations, and the oscillations inside the liquid droplet seen in Fig. 4.5(b) and (c) result from (i) continuous reflections of compression and rarefaction waves at the gas-liquid interface, and (ii) through surface tension-generated pressure waves resulting from local changes in droplet surface curvature. The gas phase shock structure and droplet shape in the leeward side remained similar in all three droplet cases. As the droplet deforms, the radius of curvature of the windward side of the droplet decreases causing the upstream bowshock to move away from the droplet surface (Fig. 4.5 (a)-(b)). The location of the bowshock in Fig. 4.5, and its dependence on the evolving droplet diameter is in agreement with the empirical relation for bowshock stand-off distance for flow around a sphere given by $\delta = 0.0715D \times e^{3.25/M_\infty^2}$ [115].

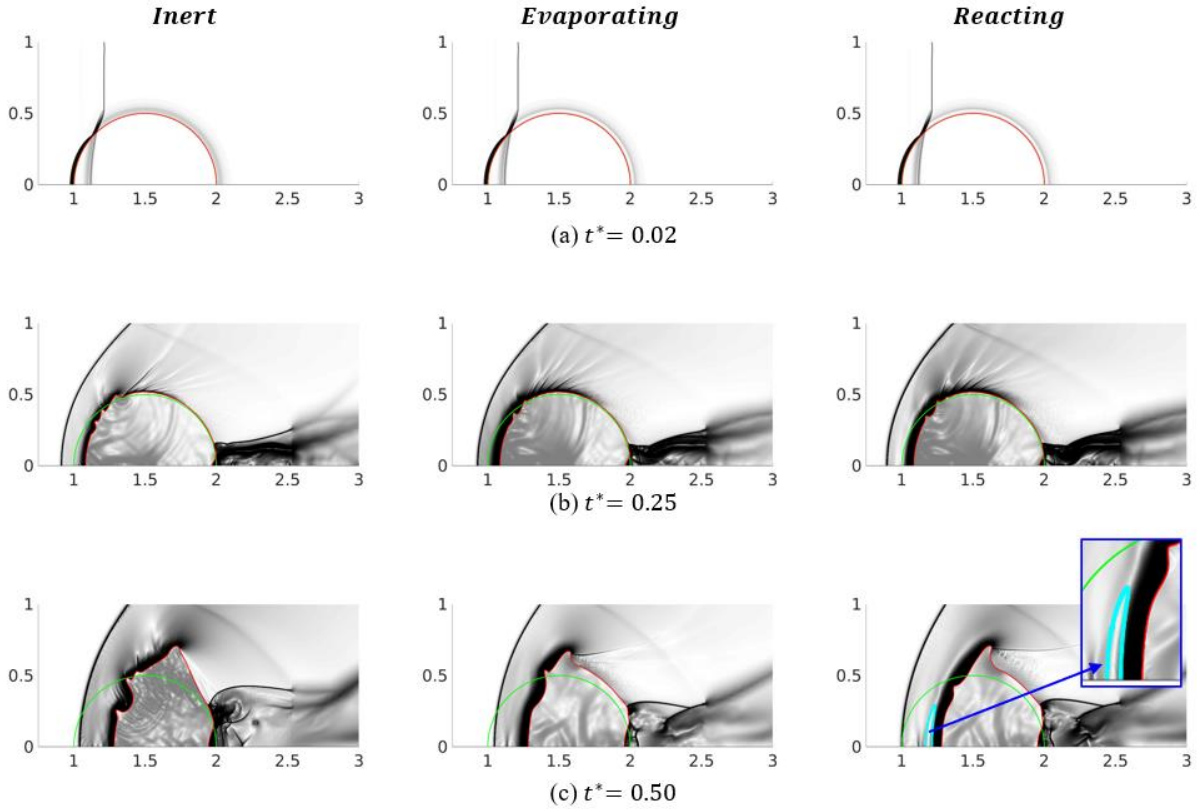

Fig. 4.5: Numerical Schlieren images for a $5\mu m$ $(We = 500)$, shock-droplet interaction, showing the evolution of inert (left), evaporating (middle) and reacting (right) cases. Droplet interface at $t^* = 0$ is shown as the green line, while the cyan outline in the inset in fig. (c) bottom right indicates the presence of the diffusion flame.

To explain observed differences in droplet surface morphology, we examine the behavior of flow quantities plotted along the droplet surface coordinate $\frac{\xi}{\pi D}$. In Fig. 4.6(a), we plot a normalized local Weber number $\left(\frac{We_\xi}{We_\infty} = \frac{\rho_\xi u_\xi^2}{\rho_\infty u_\infty^2}\right)$ along $\frac{\xi}{\pi D}$ at $t^* = 0.25$, where the subscripts 'ξ' and '∞' indicate quantities evaluated at the droplet surface and the freestream respectively. As the shock wave traverses over the droplet, the post-shock gasses mix with the lower-momentum vapor layer resulting in a lower local Weber number for the evaporating and reacting cases relative to the inert droplet. In addition, the high-speed streamlines corresponding to the flow of post-shock gasses are displaced farther away from the droplet surface by the fuel vapors in the evaporating

and reacting cases, lowering the near-surface local Weber numbers in those simulations. The local normalized Weber number is essentially a normalized momentum transfer flux in the tangential direction, and determines the rate at which interfacial perturbations grow due to Kelvin-Helmholtz instability. These differences in early-stage KH growth also explain differences in the structure and orientation of the thin liquid sheet pulled from the equatorial region of the droplet in Fig. 4.5(c), since the KH waves appear to provide the perturbation seed for the thin sheet ejection.

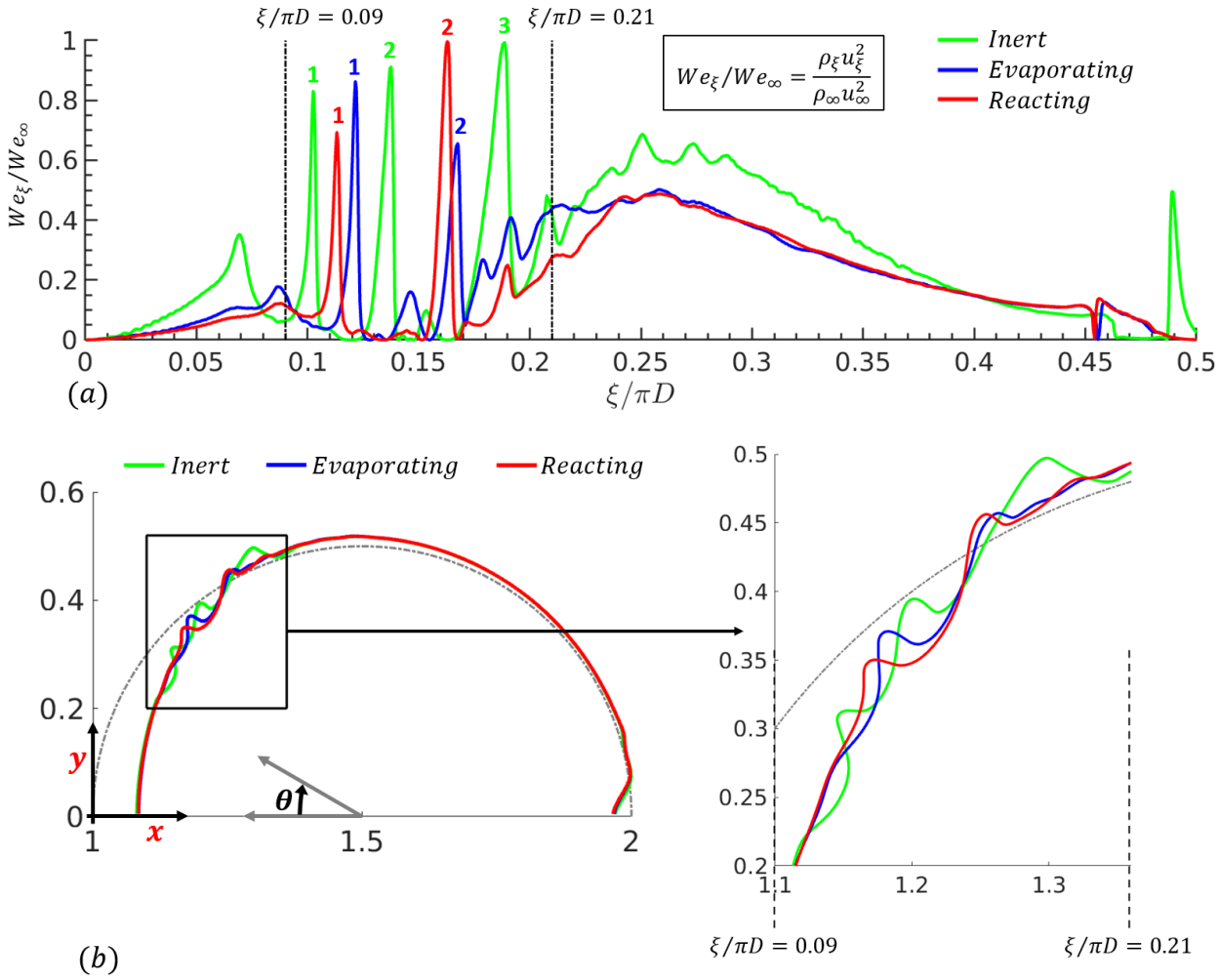

Fig. 4.6 (a) Normalized local Weber number plotted against the interfacial coordinate at $t^* = 0.25$. (b) Zoomed in view of the interface shows KH instability waves in the inert, evaporating and reacting droplet cases.

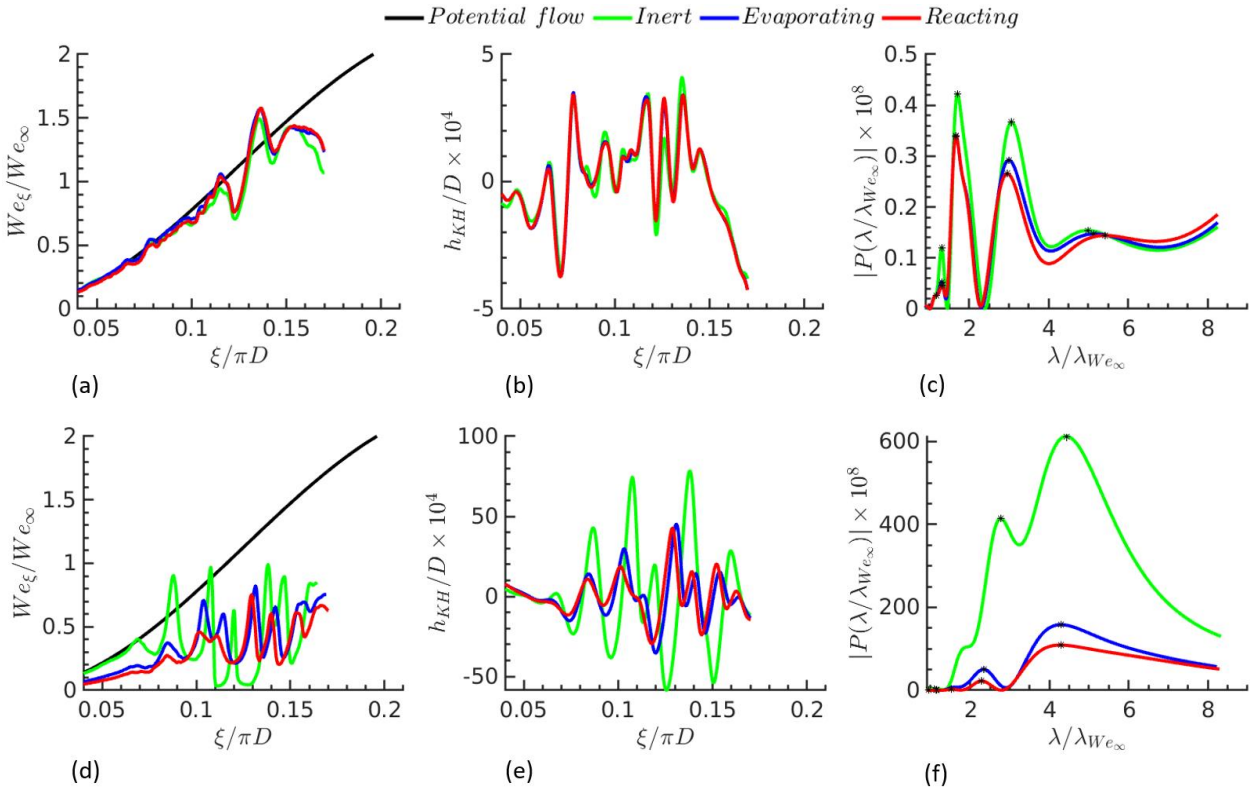

Fig. 4.7: Top and bottom row correspond to $t^* = 0.044$ and $t^* = 0.128$ respectively. (a,d) Normalized local Weber number along the interface coordinate $\xi/\pi D$, (b,e) normalized KH instability amplitude, and (c,f) corresponding power spectra for KH instability amplitude

It is thus important to understand the properties of early-time KH growth on the droplet, since it affects late-time droplet features. We analyze simulation images from $t^* = 0.044 - 0.128$, in the KH-active region $\frac{\xi}{\pi D} \in [0.04, 0.19]$. During this time window, the KH perturbation amplitudes satisfied $\frac{h_{KH}}{\lambda_{KH}} \ll 1$, and hence can be considered to be in the linear regime. In Fig. 4.7(a), we plot the normalized local Weber number defined as $\frac{We_\xi}{We_\infty}$ at $t^* = 0.044$ along the interface coordinate $\frac{\xi}{\pi D}$, for the inert, evaporating and reacting cases. We also plot a scaled local Weber number computed based on velocities obtained from potential flow theory for flow around a smooth, spherical droplet, and obtain $\frac{We_{\xi-potn.\ flow}}{We_\infty} = 2.25sin^2(\theta)$. At $t^* = 0.044$ Fig. 4.7(a), the

local Weber number from the three simulations were observed to be in good agreement with the potential flow theory estimate for a smooth sphere, consistent with the presence of small-amplitude KH perturbations at this time.

The corresponding KH amplitudes are shown in Fig. 4.7(b), and show no significant differences between the inert, evaporating and reacting droplet cases at this early time. We plot the amplitude power spectrum $\left|P\left(\frac{\lambda_\xi}{\lambda_{We_\infty}}\right)\right|$ in Fig. 4.7(c), which shows the presence of dominant modes occurring at $\frac{\lambda_\xi}{\lambda_{We_\infty}} = 1.87$ and $\frac{\lambda_\xi}{\lambda_{We_\infty}} = 3.21$, where

$$\lambda_{We_\infty} = \frac{3\pi D}{We_\infty} \tag{4.1}$$

is the most unstable mode predicted by the model of [1, 2], and evaluated for freestream conditions (the corresponding KH growth rate for these conditions is given by $\gamma_{We_\infty} = \frac{2}{3\sqrt{3}}\sqrt{\frac{\sigma}{D^3\rho_l}}We_\infty^{1.5}$). While we see a local peak in the amplitude power spectrum at $\frac{\lambda_\xi}{\lambda_{We_\infty}} \sim 1$, the modes corresponding to longer waves are dominant at this early time. We attribute this behavior to the differences between the local Weber number and the freestream value, where for a significant portion of the droplet surface $We_\xi < We_\infty$, so that according to eq. (4.1), $\lambda_\xi > \lambda_{We_\infty}$.

By $t^* = 0.128$, as KH perturbations continue to grow, significant deviations from the potential flow (smooth sphere) can be observed (Fig. 4.7(d)), seen in the decrease in the local weber number We_ξ obtained in the simulations relative to $We_{\xi-potn.\ flow}$. We also note that $We_\xi < We_\infty$ throughout the KH-active region of the droplet surface, indicating that KH perturbation amplitudes have grown (Fig. 4.7(e)) to significantly obstruct the local tangential flow velocities. As a result of the decrease in the local Weber number We_ξ, the amplitude power spectrum (Fig. 4.7(f)) now show dominant modes at even longer wavelengths with peaks

corresponding to $\frac{\lambda_\xi}{\lambda_{We_\infty}} = 2.64$ and $\frac{\lambda_\xi}{\lambda_{We_\infty}} = 4.72$ (consistent with the inverse Weber number dependence suggested by eq. (4.1)). In contrast to the early-time behavior (Fig. 4.7(b)-(c)), the amplitudes of the KH perturbations in the inert case was nearly twice as large as the reacting and evaporating cases (Fig. 4.7(e)). This faster growth of KH amplitudes in the inert case compared to the evaporating/reacting cases, is due to the higher local Weber number experienced by the inert droplet, described below.

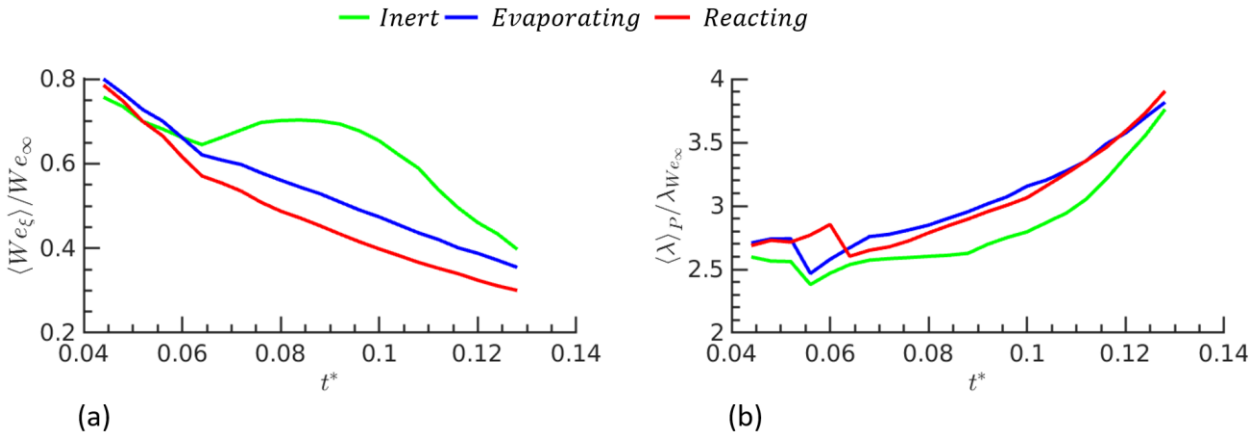

Fig. 4.8: Time evolution of (a) surface-averaged normalized local Weber number along the interface and (b) power-weighted average wavelength.

The time evolution of ξ-averaged, local Weber number denoted by $\langle We_\xi \rangle$ in eq. (4.2), is shown in Fig. 4.8(a), where we define $\langle We_\xi \rangle$ according to

$$\langle We_\xi \rangle = \frac{\int_{\xi_1}^{\xi_2} We_\xi d\xi}{\int_{\xi_1}^{\xi_2} d\xi}. \tag{4.2}$$

In eq. (4.2), ξ_1 and ξ_2 represent the limits of the KH-active region on the droplet surface. Fig. 4.8 (a) shows the inert droplet experiences a higher local Weber number compared to the evaporating/reacting droplets. In the reacting/evaporating droplets, there is a continuous supply of heavy fuel vapor that retards the tangential flow near the droplet surface, leading to the lower Weber numbers seen in Fig. 4.8 (a). In Fig. 4.8 (b), we plot the time evolution of $\frac{\langle \lambda \rangle_P}{\lambda_{We_\infty}}$, where $\langle \lambda \rangle_P$

is a measure of the dominant wavelength in the KH wavepacket called the power-weighted, average wavelength and defined according to:

$$\langle\lambda\rangle_P = \frac{\int_0^\infty \lambda|P(\lambda)|d\lambda}{\int_0^\infty |P(\lambda)|d\lambda} \tag{4.3}$$

Fig. 4.8 (b) shows that in time, as the local Weber number decreases, longer KH wavelengths are selected for growth. Furthermore, since the reacting and evaporating droplets are in a lower local Weber number environment, slightly longer KH modes are observed in those simulations (compared with the inert baseline). Finally, the power-weighted average wavelength from the simulations were compared with corresponding predictions from the model of [1, 2], i.e. eq. (4.1) computed for local flow conditions at the droplet surface ($\langle We_\xi \rangle$), and found to be in reasonable agreement, with $\frac{\langle\lambda\rangle_P}{\lambda_{\langle We_\xi\rangle}}$ varying as 1.75 ± 0.13, 1.61 ± 0.23 and 1.43 ± 0.30 for the inert, evaporating and reacting cases respectively.

4.3.2 Gas phase flowfield:

In Fig. 4.9(a) - (c), we compare contours of pressure, temperature and density respectively for the inert, evaporating and reacting droplets at $t^* = 0.5$. While pressure and density contours are qualitatively similar between the three simulations, significant differences in the temperature field are observed. Lower temperature regions ($\sim 800K$) are observed in the immediate windward and leeward sides of the reacting and evaporating droplets, in contrast to the inert droplet where these regions are at much higher temperatures ($\sim 2000K$). These differences in the temperature field can be attributed to the additional convective cooling and Stefan cooling due to cold fuel vapors generated in the evaporative and reactive cases. While the inert droplet is largely cooled through conductive heat transfer near the surface, cooler fuel vapors generated at a film temperature of $T_f \approx 650K$ in the reacting and evaporating droplets have a higher specific heat

capacity (~ three times that of the post-shock gasses), and drive additional convective cooling of the droplets. The effect of convective cooling is more pronounced on the leeward side, where the gas pressure of $\sim 0.5\ atm$ is only slightly higher than the saturation pressure $p_{sat} = 0.47\ atm$ of the preheated liquid $n - Dodecane$ droplet at 460 K. As a result, high mass fraction of fuel vapors of Y_{fuel}~0.4 (Fig. 4.10 (a)-(b),) is observed, reducing the gas phase temperature to $\sim 700K$ on the leeward side.

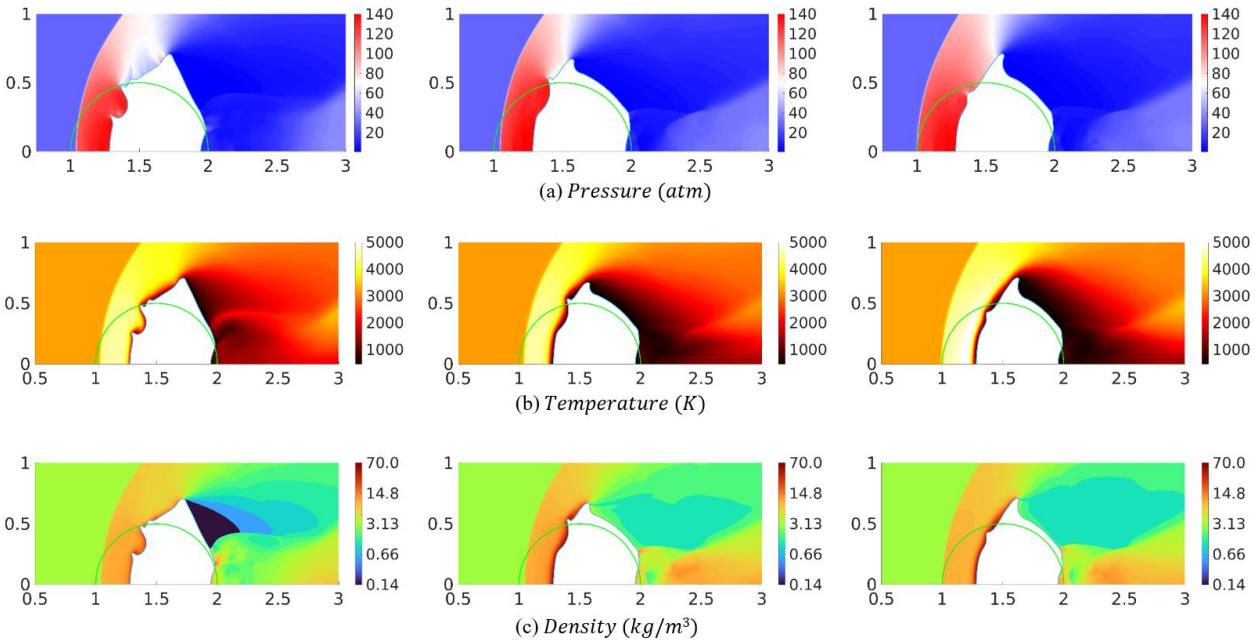

Fig. 4.9: Pressure, temperature and density contours at $t^* = 0.5$ from simulations of a 5 μm (We=500), shock-droplet interaction, showing the evolution of inert (left), evaporating (middle) and reacting (right) cases.

In Fig. 4.9 (c), a diffusion flame is visible as the light region of high temperature ($\sim 5000K$) gasses on the windward side of the reacting droplet, resulting from the reaction of evaporated fuel vapors and pure oxygen present in the post-shock gasses. A low fuel mass fraction of Y_{fuel}~$0.05 - 0.10$ in this region (Fig. 4.10 (a),(b)) represents a fuel-lean, $n - Dodecane\text{-}O_2$ mixture, so that the chemical reactions increase the gas temperature by only ~ 1000 K. However,

the presence of a high mass fraction of products $Y_{prod.} > 0.12$ in Fig. 4.10 (c) indicates the reactions have progressed significantly. The contours of the rate of reaction in Fig. 4.10(d) shows the windward side of the droplet, where pressure and temperature are highest is also the most active site for reactions (the cloud of reaction products observed in the droplet wake are transported from the windward side by the post-shock flow). Finally, the region of high reactivity in the downstream region (Fig. 4.10 (d)) can be attributed to secondary burning of accumulated fuel vapors in the droplet wake through reactions with the hot post-shock gasses and hot mixture transported from the windward side.

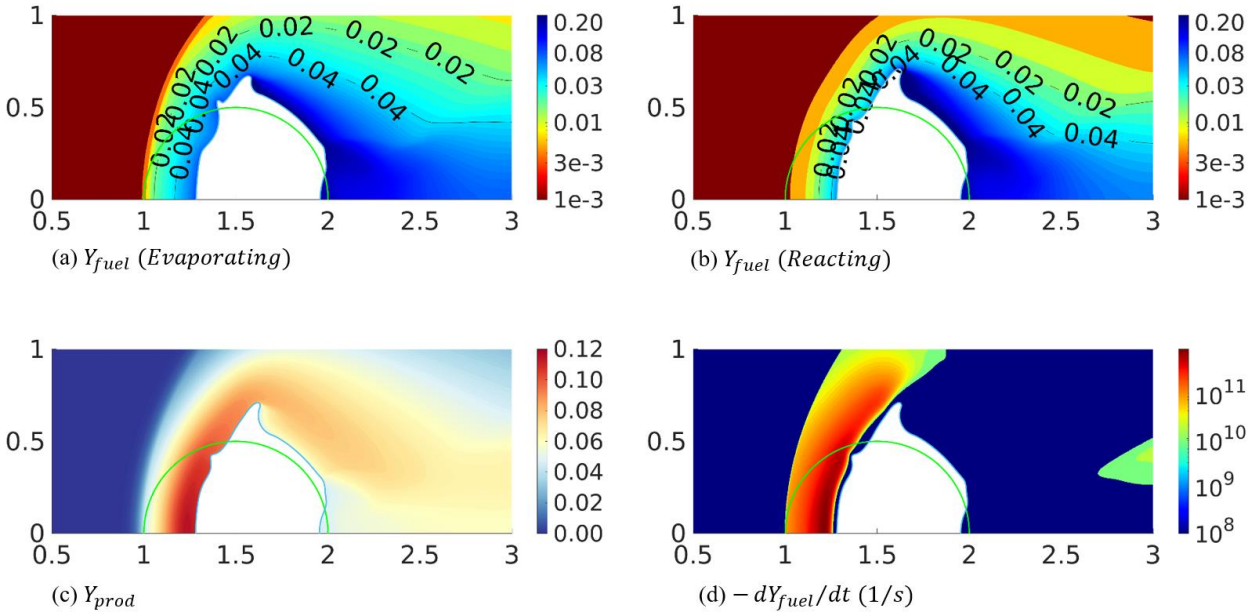

Fig. 4.10: Contours of fuel vapor mole fraction in evaporating (a) and reacting (b) droplets, reaction product mass fraction (c) and the normalized reaction rate (d) for a $5\mu m$, $We = 500$ shock-droplet interaction. t^*=0.5.

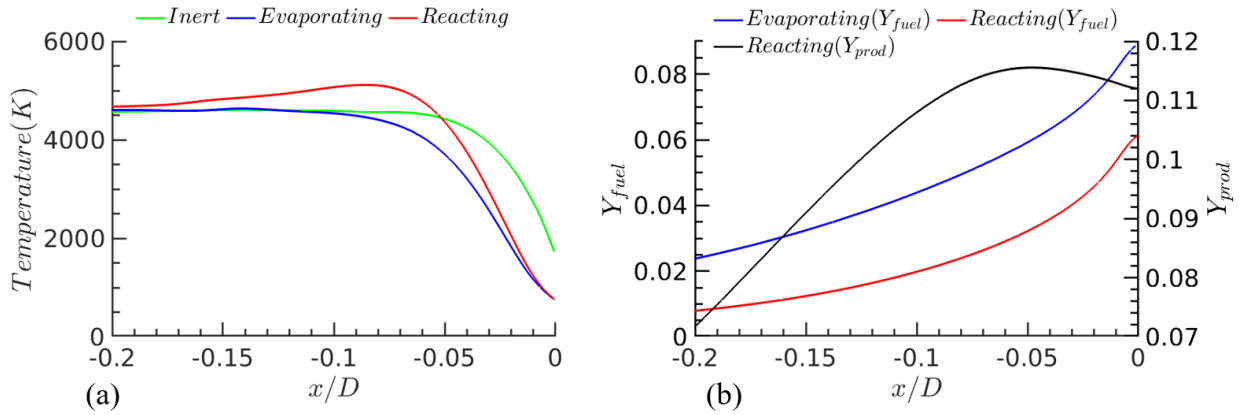

Fig. 4.11: Line plots of Temperature (a) and mass fractions (b) along the axis of symmetry and in the droplet windward region ($\frac{x}{D} < 0$). t^*=0.5.

In Fig. 4.11, we plot x-profiles of temperature, and fuel and product mass fractions along the axis of symmetry, and in the windward region of the droplet ($\frac{x}{D} < 0$). For the reacting droplet, it is evident that the heat of reaction has resulted in a temperature increase of ~1000 K at the flame site upstream of the droplet. However, temperatures for both the reacting and evaporating droplets approach similar values (~ 800 K) at the interface $x/D \rightarrow 0$), suggesting the presence of the flame did not result in significant droplet heating. Since the product mixture ($Prod + O_2$) has thermal conductivities much lower than the fuel vapors ($0.22 \leq \frac{\lambda_{O_2+Prod}}{\lambda_{fuel}} < 1$ for $T_{f,windward} \leq T < T_{bowshock}$, where $T_{f,windward} \sim 560K$ and $T_{bowshock} \sim 4400K$), as the reactions convert fuel vapors into product (Fig. 4.11 (b)), the thermal conductivity of the mixture decreases resulting in less heating of the reacting droplet relative to the evaporating case. This decrease in thermal conductivity of the gas mixture results in a lowering of the film temperature on the windward side, further decreasing the evaporation rate of the reacting droplet (Fig. 4.12 (b)). Since burning in these simulations occur under fuel-lean conditions, the reactions did not produce sufficient energy to heat the droplet significantly, thereby further decreasing the evaporation rate over time.

The film temperature, evaporation rate, and fuel mass fraction are plotted along the interface coordinate $\frac{\xi}{\pi D}$ for the evaporating and reacting droplets in Fig. 4.12 at $t^* = 0.5$. The temperature Fig. 4.12 (a) and mass fraction (Fig. 4.12 (b)) profiles are similar for the two cases, due to convective cooling and Stefan flow effects discussed earlier, which dominate heat transfer in both the reacting and evaporating droplets. In addition, the increase in product mass concentration in the reactive simulation decreases the thermal conductivity of the gas mixture, resulting in a slight decrease in the film temperature and a corresponding decrease in the evaporation rate, observed on the windward side, especially in the region $\frac{\xi}{\pi D} < 0.1$. The presence of entrapped, pre-shock, cold gasses and a low pressure region on the leeward side ($\frac{\xi}{\pi D} > 0.25$) leads to substantially lower heating of the interface and significantly lower evaporation rates at that site. In Fig. 4.12 (c), we also plot profiles of the fuel mass fraction $\left(Y_{fuel}\right)$ and mass density ρY_{fuel} along the interface coordinate at $t^* = 0.5$. We find the higher evaporative mass flux in the evaporating droplet case increases the fuel vapor density near the interface, according to $\frac{d(\rho Y_{fuel})}{dt} \propto \dot{m}''_{fuel}$. In contrast, the fuel mass fraction is higher in the wake of the reacting droplet, since $\frac{dY_{fuel}}{dt} \propto \frac{\dot{m}''_{fuel}}{\rho_g}$ and the gas density decreases sharply beyond the equatorial point due to flow separation which is more pronounced in the reacting case.

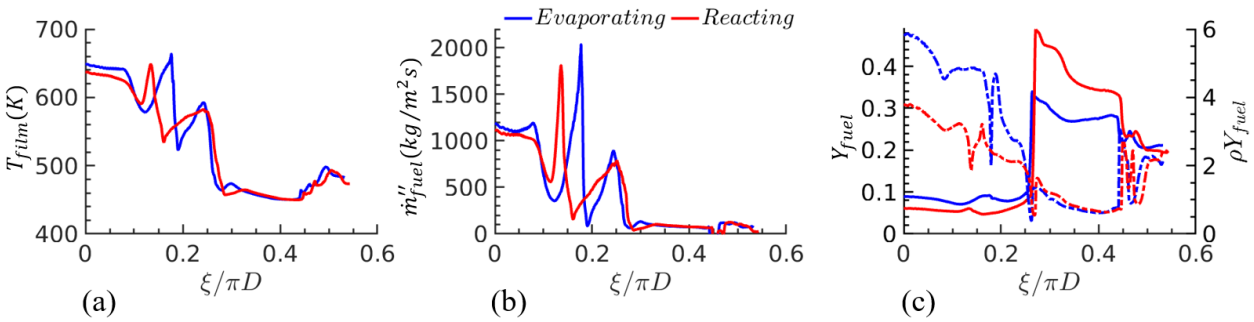

Fig. 4.12: Plots of film temperature (a), evaporation mass flux (b) and fuel mass fraction (c) along the interface coordinate $\frac{\xi}{\pi D}$ for the reacting and evaporating droplets at $t^* = 0.5$. The dashed lines in fig. (c) corresponds to fuel vapor density (ρY_{fuel}) distribution.

4.3.3 Liquid droplet flowfield:

The flowfield within the liquid fuel droplet is shown for the inert, evaporating and reacting droplet cases, at $t^* = 0.5$ and $t^* = 1.0$ in Fig. 4.13, and show qualitatively similar features. The temperature contours (Fig. 4.13 (a)) in the liquid region reveal that only a narrow interfacial layer in the vertical windward side of the droplet is heated by the hot post-shock gasses by $t^* = 1.0$. As previously discussed, this heating is predominantly the result of the intense pressure and temperature experienced by the droplet in this region. For the inert droplet, this interfacial liquid region is heated to $1400\ K$ by $t^* = 1.0$, whereas in the case of evaporating and reacting droplets, the interfacial temperature is substantially lower at $584\ K$ by t^*=1.0 due to convective cooling by the vapors. On the windward side of the inclined thin structures, a similar heating pattern, though to a diminished extent, can be observed.

For the evaporating and reacting droplets, we thus find only a thin layer within the droplet core is heated to a temperature $> 500K$ by t^*=1.0, while nearly 50% of the droplet volume is deformed into thin sheet structures. By t^*=1.0, these sheet structures were observed to travel at a velocity of ~ 300 m/s relative to the droplet core, and will continue to stretch, eventually detaching

from the droplet or puncturing through KH or RT instabilities. Thus, for these conditions, we expect that for $t^* > 1.0$, the fuel droplet will fragment through instabilities before a significant portion of the droplet core can heat up and evaporate. Estimating a thermal penetration depth (δ_p) of the droplet based purely on 1D heat conduction gives $\delta_p = \sqrt{\frac{t\lambda_l}{\rho_l C_{p,l}}}$, which over a parent droplet lifetime ($t = \tau$) gives $\frac{\delta_p}{D} = \sqrt{\frac{\lambda_l}{\rho_l C_{p,l} u_{ps} D \sqrt{\frac{\rho_l}{\rho_g}}}}$. Thus, for the $5\mu m$ droplet under these conditions, we obtain $\frac{\delta_p}{D} = 0.0086$ by $t = \tau$, so that the droplet core will not be heated sufficiently to undergo extensive evaporation, and will first deform into thin sheet structures before fragmenting. Conversely, the time required for the droplet core to be heated can be estimated from the above expression by taking $\delta_p = D/2$, to give $t^*_{\delta_p = D/2} = \frac{D C_{p,l}}{4\lambda_l} u_{g,ps} \sqrt{\rho_{g,ps} \rho_l}$. Thus, as the parent droplet fragments, we expect the smaller child droplets to undergo heating of the core over a timescale $t^* \sim D$, eventually reaching a limit where the droplets heat up and evaporate before undergoing further breakup.

The corresponding velocity contours (Fig. 4.13 (b)) indicate that the core region of the droplet achieves considerably high axial velocities of approximately $150\ m/s$ on the windward side by $t^* = 0.5$, while velocities on the leeward side are only $\sim 10\ m/s$. This relative difference in the axial velocities between the windward and leeward sides compresses the droplet in the axial direction, and contributes to the ejection of a thin sheet from the equatorial region of the droplet (Fig. 4.13 (b)). Due to the significant relative velocity difference between the droplet core ($\sim 200\ m/s$) and the thin sheets ($\sim 650\ m/s$), the sheet structures continue to stretch and become thinner. As the sheets expand further, they eventually pinch off and detach due to surface tension (shown in the inset in Fig. 4.13 (b)) in our axisymmetric simulations. While the droplet core

appears similar in all three cases, distinct differences in the morphology of the thin sheet structures are visible, and attributed to a combination of KH instabilities, internal velocity flow field of the droplet, the high momentum of the post-shock gasses and evaporation.

The corresponding pressure distribution within the droplet is shown in Fig. 4.13 (c), and displays strong oscillations, including several regions of negative pressures ($\sim -200\ atm\ to\ -500\ atm$). The observed oscillations and regions of negative pressure arise due to the compression and rarefaction waves generated and reflected within the highly distorted droplet. Note that the presence of negative pressures in the liquid region is indicative of the presence of tensile strain, and the potential for cavitation which is not modeled in our simulations.

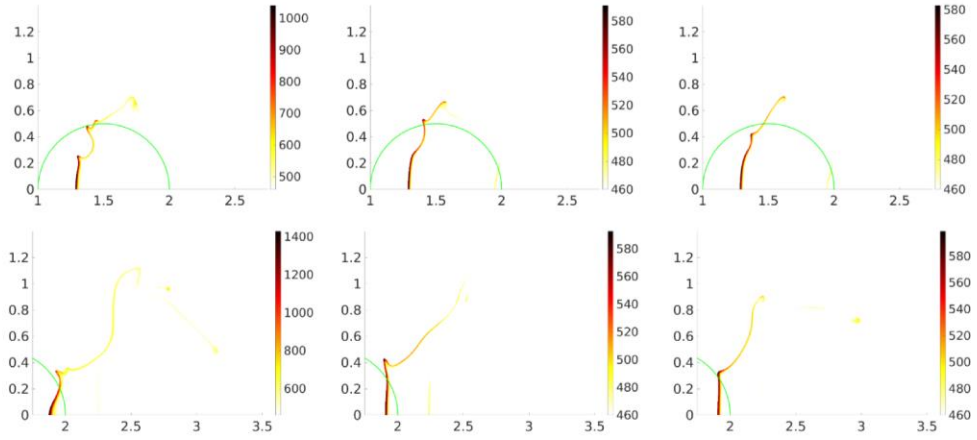

(a) $Temperature\ (K), t^* = 0.5\ (top), t^* = 1.0\ (bottom)$

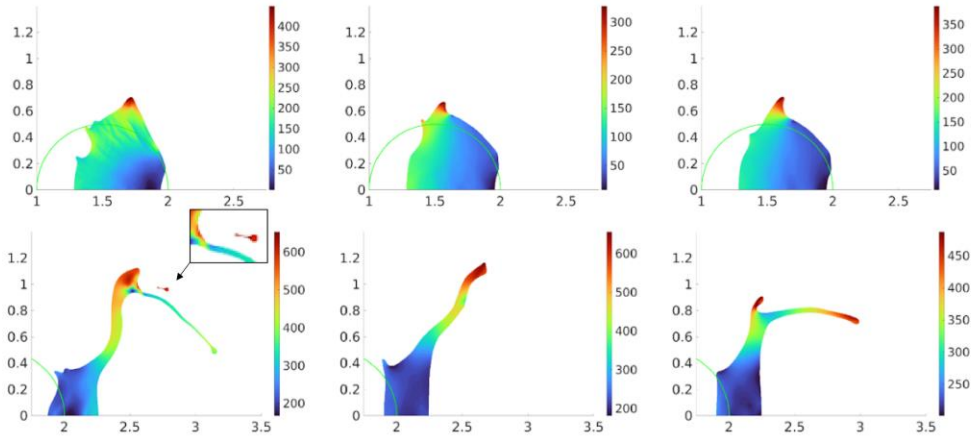

(b) $Velocity\ (m/s), t^* = 0.5\ (top), t^* = 1.0\ (bottom)$

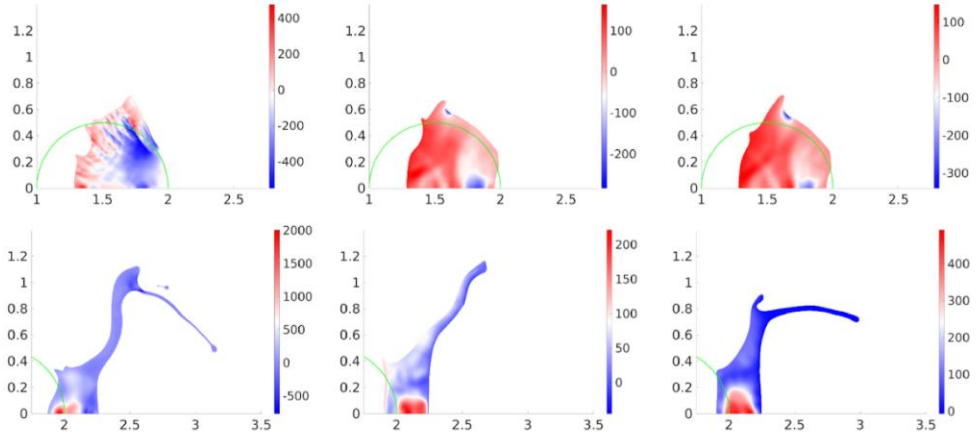

(c) $Pressure(atm), t^* = 0.5\ (top), t^* = 1.0\ (bottom)$

Fig. 4.13: Contours of droplet (a) temperature (b) axial velocity and (c) pressure at $t^* = 0.5$ and $t^* = 1.0$, for the inert (left column), evaporating (middle column) and reacting (right column) cases.

In Fig. 4.14, we plot the time evolution of surface-integrated properties, namely the normalized total surface area $\frac{A(t^*)}{A_0}$, total evaporation rate $\dot{m}_{fuel}(kg/s)$, and the average evaporation rate $\overline{\dot{m}''_{fuel}}(kg/m^2s)$ as defined below:

$$A(t^*) = \int_0^{\xi_{max}} 2\pi y(\xi, t^*) d\xi \tag{4.4}$$

$$\dot{m}_{fuel}(t^*) = \int_0^{\xi_{max}} \dot{m}''(\xi, t^*) 2\pi y(\xi, t^*) d\xi \tag{4.5}$$

$$\overline{\dot{m}''_{fuel}}(t^*) = \frac{\dot{m}_{fuel}(t^*)}{A(t^*)} \tag{4.6}$$

In eqs. (4.4)-(4.6), the integral is performed along the droplet interface coordinate ξ, from $\xi = 0$ at the windward side ($y = 0$) to $\xi = \xi_{max}$ at the leeward side ($y = 0$), while y represents the radial coordinate position of interface element $d\xi$, and $A_0 = \pi D^2$.

Fig. 4.14(a) exhibits a monotonic increase over time in all three cases. For $t^* < 0.4$, droplet surface area growth is dominated by small-scale KH instabilities, while the overall shape remains spherical or elliptic. By $t^* = 0.6$, the thin sheets have pinched off in all three cases, which are then extensively stretched by the post-shock gasses and correspond to the faster growth rate of the normalized area. As discussed earlier, a layer of heavy vapors surrounds the evaporating and reacting droplets, resulting in slower initial growth of interfacial KH instabilities, followed by slower stretching of the droplet at late times, compared to the inert droplet case. At late times ($t^* = 1.03$), the thin sheet structures attached to the inert droplet undergo breakup, resulting in the sudden increase in $\frac{A(t^*)}{A_0}$.

The time evolution of the total evaporation rate and surface-averaged evaporation rates are shown in Fig. 4.14 (b)-(c) for the evaporating and reacting droplet cases. The negative evaporation

rates observed at early times correspond to condensation on the droplet surface, due to the high-pressure, post-shock gasses immediately surrounding the droplet. Due to the intense heating of the windward side of the droplet, the film temperature rises significantly $(T_f = 650K)$, resulting in positive total and average evaporation rates by $(t^* = 0.1)$. The windward side of the droplet experiences the most intense heating, and is the most active site of evaporation, while the ejected thin sheets are more aligned with the gas flow and do not experience significant heating or evaporation. Thus, the active site of vapor production (windward surface) experiences only a modest increase in area, in contrast to the thin sheets which grow rapidly without contributing significantly to vapor production. As a result, in Fig. 4.14 (b)-(c), for $(t^* > 0.6)$, the total evaporation rate increases gradually, while the surface-averaged evaporation rate decreases over time.

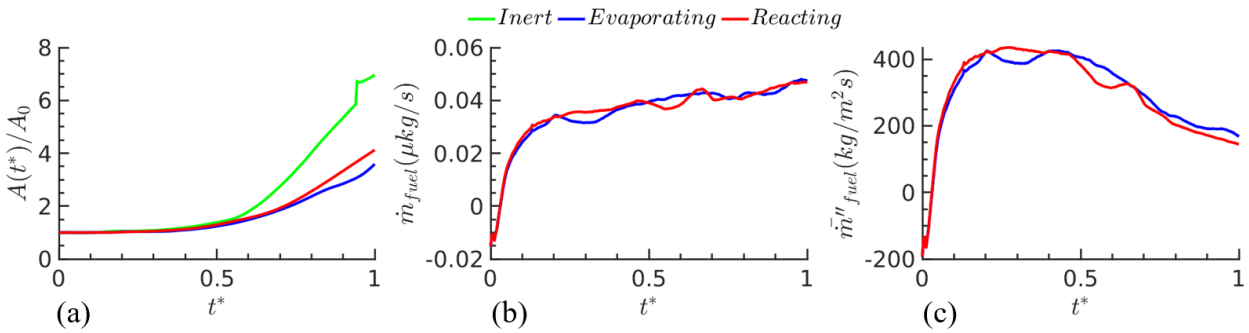

Fig. 4.14: Time evolution of (a) normalized total surface area of the droplet (b) total fuel evaporation rate and (c) surface-averaged evaporation rate.

4.4 Effect of Damkohler number

We have performed simulations in which the reaction rates associated with the Arrhenius rate law (eq. (2.13)) have been varied from the baseline case, yielding Damkohler numbers Da of 0.24, 2.4 and 24. In the context of the shock-droplet interaction investigated here, the Damkohler number can be defined as $Da = \frac{\tau_{flow}}{\tau_{ind}}$, where $\tau_{flow} = \frac{D}{u_{ps}}$ refers to the flow time scale and the induction time τ_{ind} represents a chemical timescale. Due to the spatial inhomogeneities in pressure

and temperature fields as well as the gas phase velocities observed in detonation engines, Da associated with droplet burning can vary significantly with the local environment and fuel properties. Thus, the objective of these simulations is to isolate the effect of chemical reactivity on droplet evaporation, combustion and breakup characteristics.

Contour plots of temperature, fuel and product mass fractions, and normalized reaction rate from the reactivity-variation study are shown in Fig. 4.15, and correspond to $t^* = 0.5$. Line plots of these quantities are plotted along the axis of symmetry, and in the region immediately upstream of the droplet ($\frac{x}{D} < 0$) in Fig. 4.16. With increase in chemical reactivity, the flame temperature on the windward side was observed to increase, reaching $T_{flame} = 5117\ K, 5506\ K,$ and $5752 K$ (Fig. 4.16 (a)); the observed increase in flame temperature results directly from a corresponding increase in the amount of fuel burnt by $t^* = 0.5$ (Fig. 4.16(c)) through higher reaction rates, releasing greater energy. Similarly, the leeward-side cold flow region (dark red color in Fig. 4.15 (a)) high in fuel mass fraction at cooler temperatures, was observed to shrink with increasing Da, as more of the fuel in this region undergoes combustion.

The flame temperatures in Fig. 4.16 (a) are lower than the corresponding values from the 1D simulations described in § 3.1, which is attributed to the continuous removal of unburnt fuel vapors and hot burnt products from the flame site by the post-shock flow. In the 1D simulations (§ 3.1), the flame also continued to drift away from the interface due to Stefan flow and volume expansion. In contrast, in the 2D axisymmetric simulations, the flame site remains at a fixed distance from the windward side interface ($x_{flame}/D \sim -0.03$). The fuel mass fraction at the flame site is nearly constant as fuel vapors reach the flame due to advection and diffusion, but are also transported away to the leeward side by the interface tangential velocity.

We also note from the reaction rate contours (Fig. 4.15 (b)), that the chemically active region upstream of the droplet is more diffuse for the less reactive case ($Da = 0.24$), whereas at higher reaction rates ($Da = 24$), this region substantially thins to a narrow region of high intensity reactions. This trend is broadly consistent with laminar diffusion flame theory [116, 117], which predicts that as Da is varied from the frozen chemistry limit ($Da \to 0$) to infinitely fast chemistry ($Da \to \infty$), the flame thickness decreases to an infinitesimally thin flame. (In the $Da \to 0$ limit, reaction rates are low and the flame thickness is large, with the fuel and oxidizer diffusing into each other, while as the $Da \to \infty$ limit is approached, the fuel and oxidizer streams mix and react instantaneously, across an infinitely thin flame).

As Da is increased and the reactions become diffusion-limited, the flame temperature reaches the adiabatic flame temperature values, while shifting towards the deficient reactant side [116, 117]. This is shown in the line plots of the rate of reaction (Fig. 4.16 (b)), where we observe that as the chemical reactivity increases, the flame site moves closer to the droplet. Consistent with observed trends in the temperature contours, the windward and leeward regions that are occupied by unreacted fuel vapors (Fig. 4.15 (c)) were found to decrease with increasing chemical reactivity. At $Da = 0.24$ for instance, a significant amount of the unreacted fuel (partially produced on the windward side) was transported downstream, and reacted at a distance ~ $2D$ from the droplet; at higher reactivity ($Da = 24$), this burnoff distance decreases to $0.5D$, indicating that with the increase in the Damkohler number, the detached leeward flame moves closer to the droplet (for the $Da = 24$ case, the leeward side flame was observed to propagate upstream and become attached to the droplet by $t^* = 0.8$ (not shown), and in the process burning a significant amount of leeward side unreacted fuel). The fuel mass fraction line plots (Fig. 4.16 (c)) show that the windward cutoff location beyond which no fuel exists (due to being consumed in reaction),

decreased to $x = -0.14D$ and $-0.06D$ from the droplet for the Da = 2.4 and Da = 24 cases respectively. The amount and distribution of reaction products show the greatest sensitivity to variations in Da, as the product mass fraction increases from ~0.1 to ~0.4 as seen in the contour (Fig. 4.15 (d)) and line plots (Fig. 4.16 (d)), along with significant secondary burning observed downstream of the droplet in the more reactive cases.

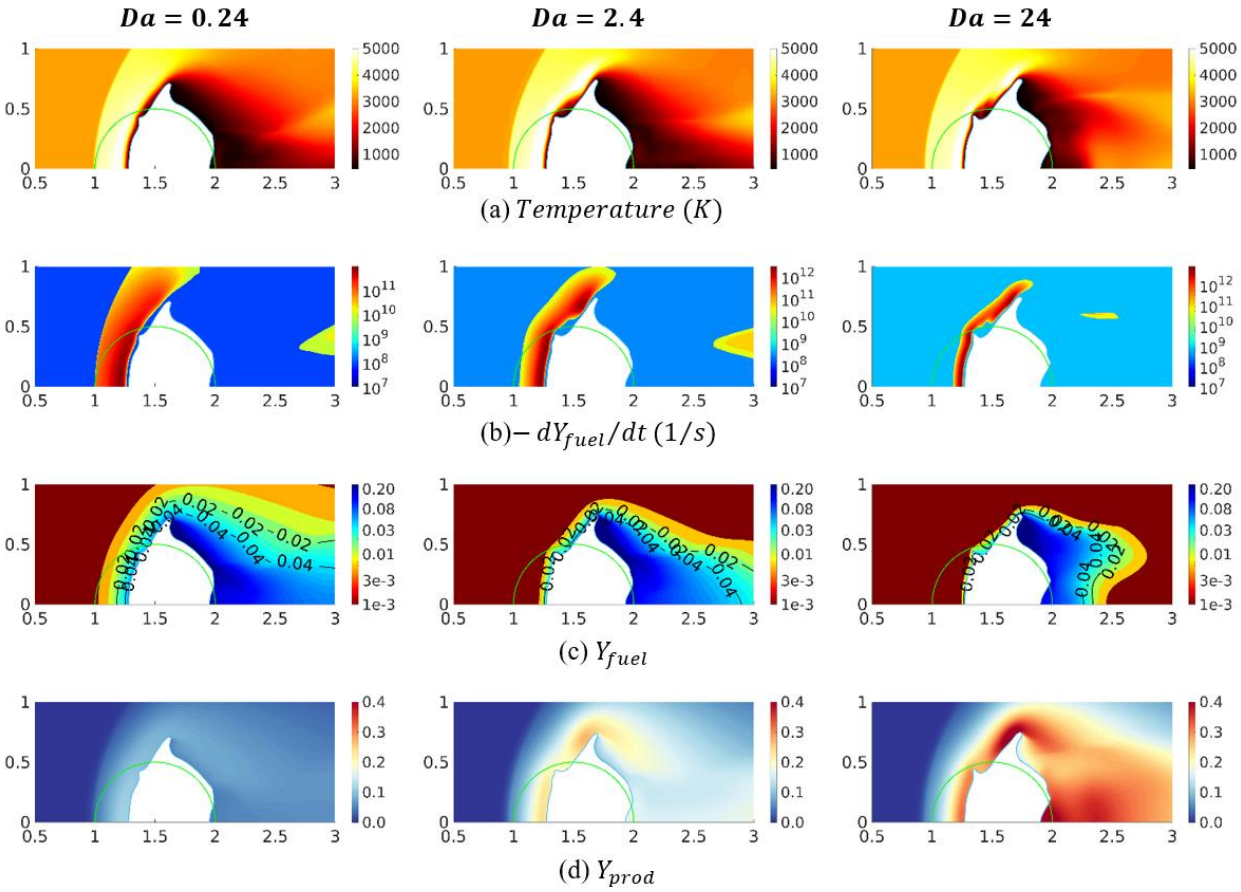

Fig. 4.15: Temperature, reaction rate, fuel and product mass fraction contours at $t^* = 0.5$ corresponding to different values of reactivity (Da = 0.24, Da = 2.4, Da = 24.0).

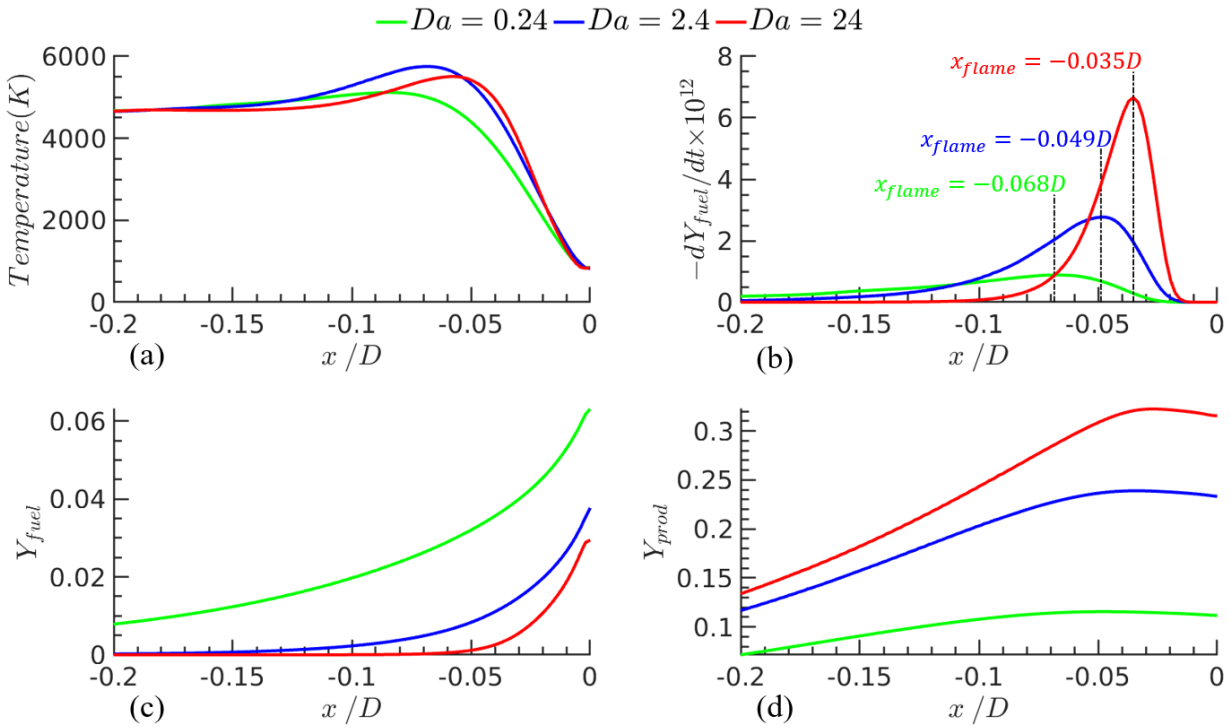

Fig. 4.16: Line plots at $t^* = 0.5$ of temperature (a), reaction rate (b), fuel (c) and product (d) mass fraction along the axis of symmetry, and plotted upstream of the droplets ($\frac{x}{D} < 0$), corresponding to different values of reactivity (Da=0.24, Da=2.4, Da=24.0).

The liquid temperature and velocity flow field contours for the above simulations are shown in Fig. 4.17 for $t^* = 0.5$ (top row) and 1.0 (bottom row). The heating patterns within the droplet (Fig. 4.17 (a)) exhibited similar behaviors in all three cases representing the Da variation, with the maximum heating occurring on the vertical windward side of the droplet, and reaching a value of $\sim 585\ K$. For the $Da = 0.24$ and 2.4 cases (also visible in Fig. 4.16 (a) at $\frac{x}{D} = 0$), the leeward side experienced significantly lower heating, resulting in a liquid temperature increase of only $\sim 10\ K$. For the $Da = 24$ droplet, the fuel mixture in the leeward side had auto-ignited by $t^* = 0.8$, as it mixed with the hot gasses transported from the windward region resulting in a thin layer of high temperature liquid ($\sim 500K$). In contrast, the thin structures ejected from the droplet are aligned with the gas flow at late times, and consequently do not experience stagnation flow

heating, reaching temperatures of only $\sim 460\ K$ (Fig. 4.17 (a)) by $t^* = 1.0$. As chemical reactivity increases, the heavy fuel vapor surrounding the droplet is consumed at a faster rate depleting this region of the high-density vapor. This in turn leads to a higher growth rate of the ejected sheets (the sheet tip velocities at $t^* = 1.0$ were observed to increase from $\sim 450\ m/s$ to $\sim 600\ m/s$ as Da is varied from 0.24 to 24), while the sheet length increases nearly twofold by the end of the simulations.

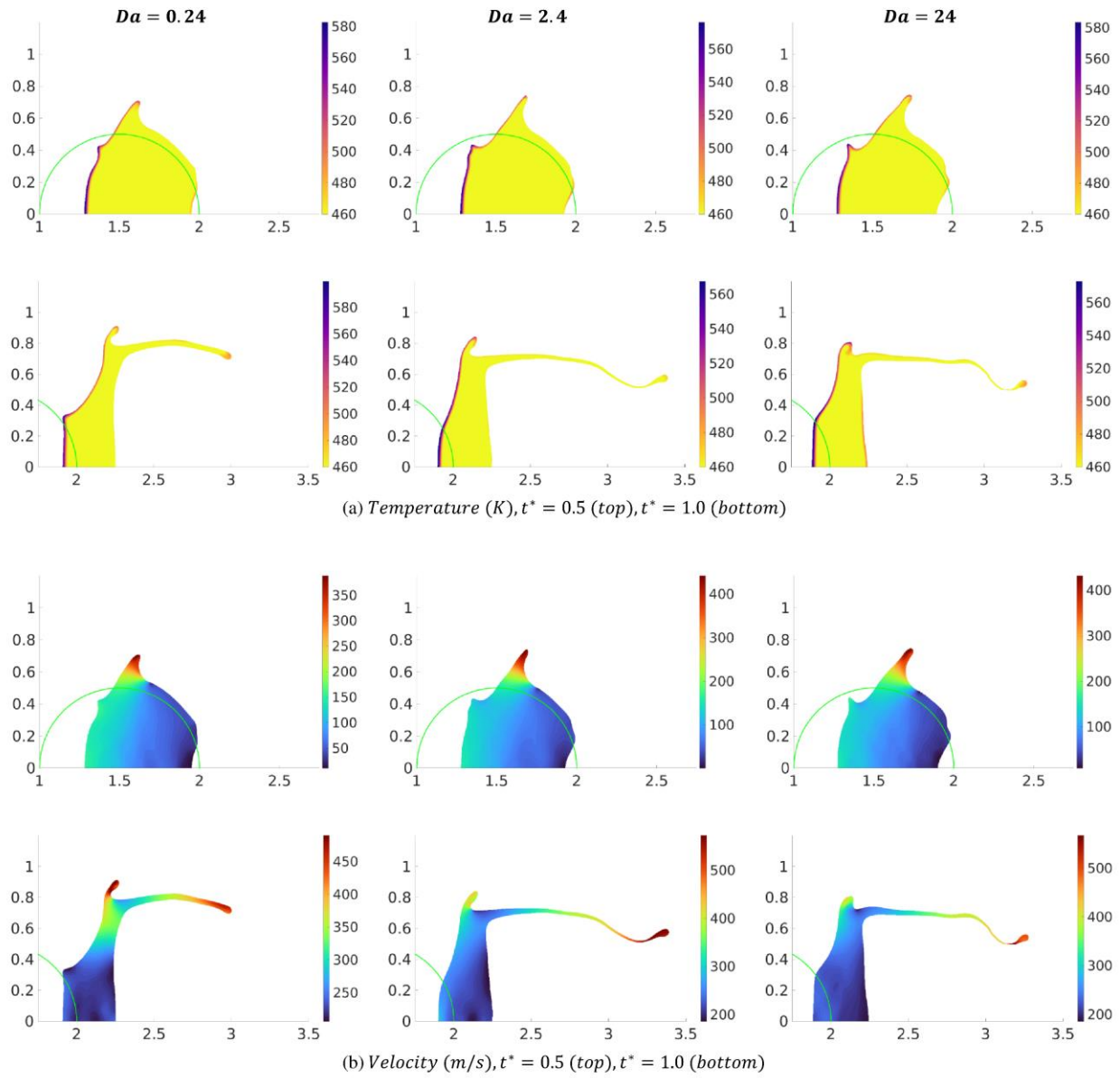

(a) $Temperature\ (K), t^* = 0.5\ (top), t^* = 1.0\ (bottom)$

(b) $Velocity\ (m/s), t^* = 0.5\ (top), t^* = 1.0\ (bottom)$

Fig. 4.17: Contours of droplet (a) temperature and (b) velocity magnitude flow field at time $t^* = 0.5$ and $t^* = 1.0$, for different reactivity (Da=0.24, Da=2.4, Da=24.0) cases.

In Fig. 4.18 (a) - (d), we plot the film temperature, evaporation rate, fuel and product mass fractions along the droplet interface for different Da conditions, and at $t^* = 0.5$. From Fig. 4.18 (a), the film temperature shows only slight variations with reaction rates, in accordance with a modest 10% increase in the flame temperature as Da is varied from 2.4 to 24. This is partly explained as the effects of the strong convective and Stefan cooling, which counter the heating

effects of the flame on the droplet. The liquid saturation pressure (which depends on the film temperature), also showed little variation in these simulations, resulting in very similar evaporation rate profiles seen in Fig. 4.18 (b).

The interfacial fuel mass fraction profiles (Fig. 4.18 (c)), show different behaviors in the windward ($\frac{\xi}{\pi D} < 0.25$) and the equatorial-leeward $\left(0.25 < \frac{\xi}{\pi D} < 0.45\right)$ regions. On the windward side, the fuel mass fraction decreases with increase in Da (from Y_{fuel}~0.061 at $Da = 0.24$ to Y_{fuel}~0.031 at $Da = 24$), due to greater fuel consumption at the flame site at higher reaction rates. However, on the equatorial-leeward region of the droplet, the opposite trend is observed with peaks in Y_{fuel} increasing with Da. The latter trend is due to flow separation behind the equatorial KH crest, visible in all three reactive droplet simulations at $t^* = 0.5$ (Fig. 4.15 (c)). In the flow separation region, the low pressures ($1 - 2\ atm$) and preheated liquid temperatures of $\sim 460\ K$ leads to a higher evaporation rate, and higher fuel mass fraction. Furthermore, the pressure in this flow separation region is highly sensitive to the amplitude of the KH wave crest, which was observed to increase with increase in Da. The reaction product mass fractions are plotted in Fig. 4.18 (d) along the interfacial coordinate, and show greater reaction products produced at higher Da conditions.

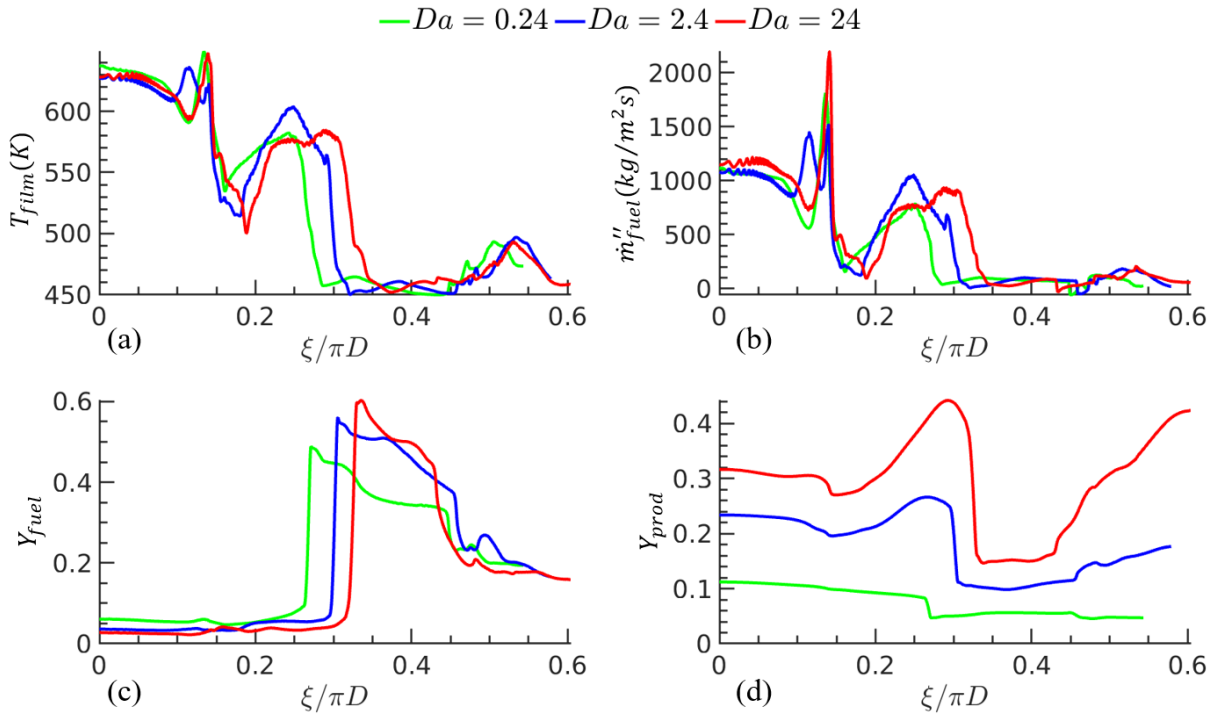

Fig. 4.18: Plots of (a) film temperature (b) evaporation rate (c) fuel mass fraction and (d) product mass fraction along the interface at $t^* = 0.5$, for different reactivity ($Da = 0.24$, $Da = 2.4$, $Da = 24.0$) cases.

In Fig. 4.19, we plot the time evolution of the normalized droplet surface area, total evaporation rate, and surface-averaged evaporation rates as defined in eq. (4.4)-(4.6). The evolution of the total surface area with time (Fig. 4.19 (a)) reflects droplet stretching features similar to those observed in Fig. 4.17 (a)-(b) - initial period of constant total area corresponding to a droplet that is nearly spherical, followed by increase due to KH instabilities and thin sheet formation. The area growth rates for the $Da = 2.4$ and $Da = 24$ cases are similar, and show a sudden increase at $t^* = 0.4$ in the higher reactivity simulation, corresponding to the breakup of the more unstable droplet (i.e. $Da = 24$ at $t^* = 1.03$) in that case. The droplet in the low reactivity case ($Da = 0.24$) is surrounded by a relatively thick layer of unburnt heavy fuel vapors that slows growth rate of KH instabilities and surface area. The total evaporation rate (Fig. 4.19 (b)) is proportional to the droplet surface area, and is thus higher for the most reactive simulation ($Da =$

24). The evaporation rate on the whole appears only weakly dependent on reactivity, since the cooling effects of the Stefan flow and convective flow on the droplet dominates over variations in heating by the flame. In contrast, the surface-averaged evaporation rate which accounts for variation in droplet surface area with reactivity, shows similar trends for all three cases.

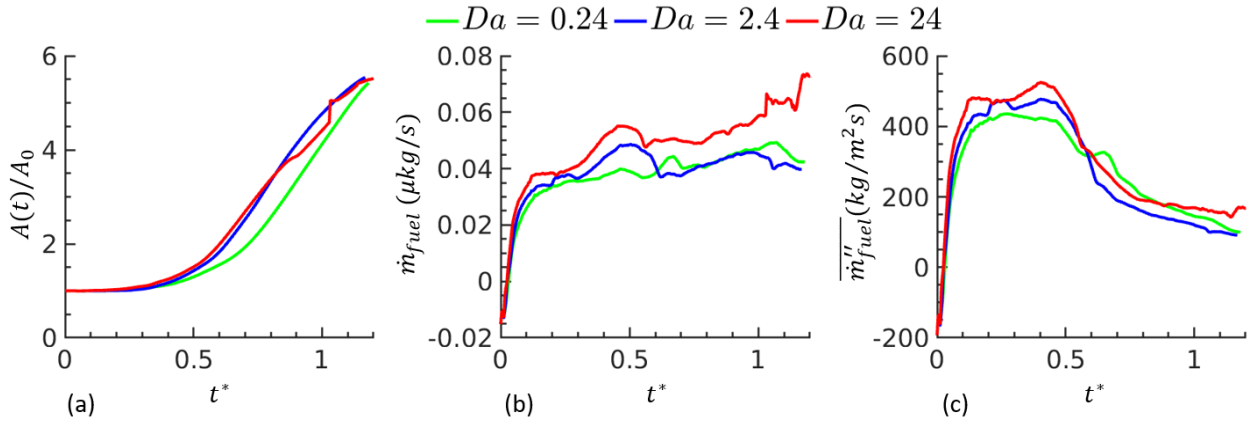

Fig. 4.19: Plots of (a) normalized surface area (b) total evaporation rate (c) surface-averaged evaporation rate for different reactivity (Da = 0.24, Da = 2.4, Da = 24.0) cases.

In Fig. 4.20 (a) and (b), we plot the time-averaged flame temperature $\bar{T}_{flame}$ and flame position $\bar{x}_{flame}$, computed using eqs. ((4.7)-(4.8)) and along the axis of symmetry. The total fuel vapors produced over the course of the simulation, Δm_{fuel} (eq. (4.9)) and total reaction products produced Δm_{prod} (eq. (4.10) are obtained by integrating eqs. (4.9)-(4.10) from $t = 0$ to τ, and shown in Fig. 4.20 (c)-(d). Note that $\dot{m}_{fuel}(t)$ in eq. (4.9) is the instantaneous surface-integrated fuel mass production rate from eq. (4.5). In eq. (4.10), the first term on the rhs is a surface integral of product species mass flux from the simulation domain boundaries, while the second term represents the difference in the total amount of products present in the solution domain between $t = 0$ and $t = \tau$.

$$\bar{T}_{flame} = \frac{\int_0^\tau T_{flame}(t)dt}{\int_0^\tau dt} \tag{4.7}$$

$$\frac{\bar{x}_{flame}}{D} = \frac{1}{D}\frac{\int_0^\tau x_{flame}(t)dt}{\int_0^\tau dt} \tag{4.8}$$

$$\frac{\Delta m_{fuel}}{m_0} = \frac{1}{m_0}\frac{\int_0^\tau \dot{m}_{fuel}(t)dt}{\int_0^\tau dt} \tag{4.9}$$

$$\frac{\Delta m_{prod}}{m_0} = \frac{1}{m_0}\int_0^\tau \oint \rho Y_{prod}\vec{u}.\overrightarrow{dA}\,dt + \frac{1}{m_0}\left[\oiint \rho Y_{prod}dV\right]_{t=0}^{t=\tau} \tag{4.10}$$

As the Damkohler number is increased, the higher reaction rates lead to greater fuel vapor consumption at the flame site and heat release, resulting in higher flame temperatures seen in Fig. 4.20 (a). Since the evaporation mass flux (Fig. 4.18 (b)) and the velocity of the corresponding fuel vapors approaching the flame remain approximately the same for the three cases, increasing the reaction rates resulted in the flame site moving closer to the droplet surface (Fig. 4.20 (b)) in accordance with classical jet diffusion flame theory [116, 117]. As shown in Fig. 4.20 (c), increasing the Damkohler number by two orders of magnitude in our simulations resulted in an increase of ~25% in total fuel vapor mass produced. The higher reaction rates result in faster consumption of fuel vapors and the formation of a vapor-deficient region near the droplet surface, thereby increasing the evaporation rate. Since more fuel vapors were produced as Da was increased, and were nearly completely consumed in the reactions, an increase in total reaction products produced was observed with reactivity (Fig. 4.20 (d)).

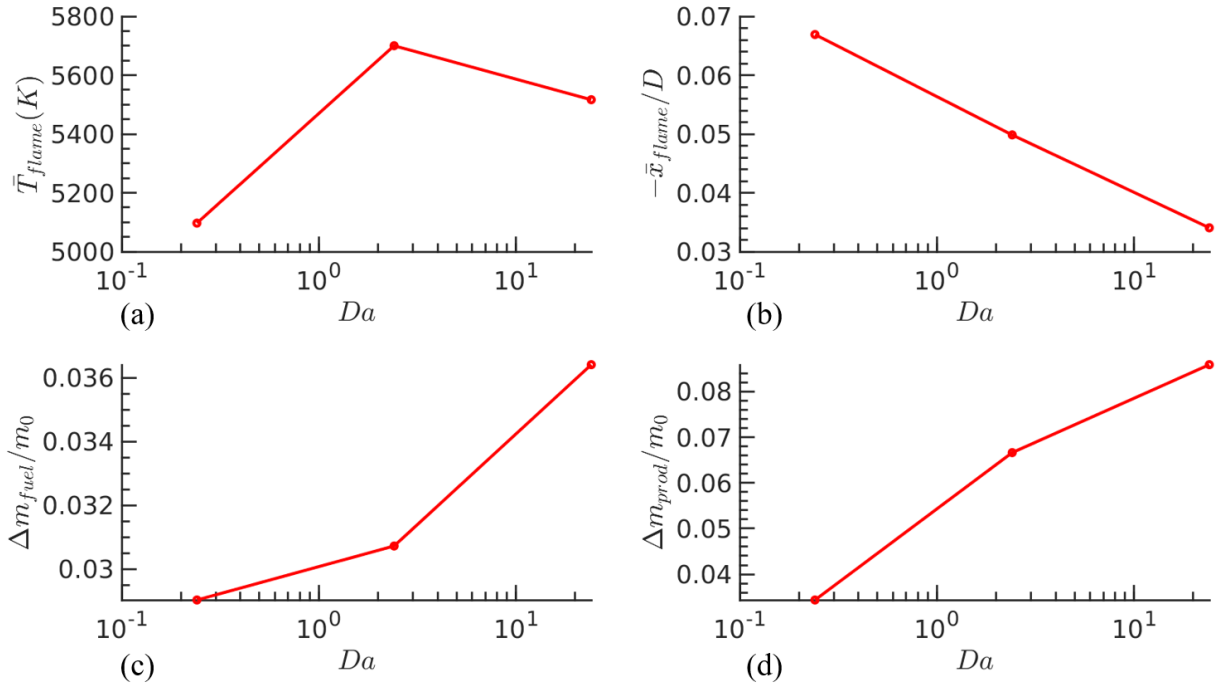

Fig. 4.20: (a) Flame temperature (b) flame position with respect to the windward side interface (c) total fuel vapors produced by $t^* = 1.0$ (d) total reaction products produced by $t^* = 1.0$ for different reactivity ($Da = 0.24$, $Da = 2.4$, $Da = 24$) cases.

CHAPTER 5:SUMMARY AND CONCLUSIONS

5.1 Mode transition in Rotating Detonation Engines

From detailed numerical simulations using multi-step reaction kinetics, we have presented an alternate pathway through which the number of detonation waves in an RDE can abruptly transition. This finding appears to be a departure from earlier studies [5, 10, 12, 15-17], which hypothesized the transition is triggered when the ratio of the detonation wave height to the cell height was no longer an integer. In contrast, our simulations show the mode number of detonation waves can change even when no cellular detonation network existed prior to transition. These findings were established in this article primarily through qualitative results, while a more quantitative and predictive approach to this phenomenon will be taken up in subsequent papers.

Mode transition, when observed in our simulations was triggered by the formation of localized microdetonations which are initially formed as spherical blastwaves and then transformed into planar waves capable of propagating in either direction. The phase reversal does not appear to be predicted by changes in N_2 concentration but could result from complex transients that accompany the mode transition process. Two sets of simulations were performed to examine if the observed phenomena were dependent on the specific pathways along which the [N_2] perturbations were applied. In cases 1 - 9, the [N_2] perturbations were applied in a single, large step, so that the increased reactivity in the terminal state typically produced transition to a new stable state. Case 10 represents an alternate approach in which [N_2] was varied incrementally (in a process that approximated a continuous trajectory). However, due to the gradual decrease in N_2 moles, mode transition was not observed except at the final value of 2.5 and 0.5 moles of N_2, when nW changed to 2 and 4 respectively. Collectively, these results indicate the initial configuration

and the perturbation path influence the mode transition process and the number of detonation waves observed in the final state. Key engine performance parameters such as the total thrust, specific impulse and detonation wave velocity were also evaluated for both sets of simulations. In all cases, the total thrust showed a weak dependence on the fuel mixture reactivity, in spite of the occurrence of multiple mode transition events. In contrast, the specific impulse increased with increasing fuel reactivity with potential implications for the design and operation of practical RDE devices.

From detailed numerical simulations using multi-step reaction kinetics, we have presented an alternate pathway through which an RDE can undergo mode transition. This finding appears to be a departure from earlier studies [5, 10, 12, 15-17], which hypothesized the transition is triggered when the ratio of the detonation wave height to the detonation cell height was no longer an integer. In contrast, our simulations show the mode number of detonation waves can change even when no cellular detonation network existed prior to transition. It was also established that $\tau_{MD}<\tau_L$ is a necessary condition for mode transition to occur, ensuring the local hot spot can grow into a detonation wave (through DDT) before being consumed by the parent wave. A robust procedure to estimate τ_{MD} from peak pressure time histories associated with the hot spots was presented. Based on these observations, a relationship to predict the number of DWs was proposed and verified using data from numerical simulations over a wide range of inlet conditions.

5.2 Evolution of a shock-driven liquid fuel droplet

In this article, we have presented the first detailed 2D axisymmetric numerical simulations of a high Mach number shock interacting with a liquid hydrocarbon fuel droplet, considering the simultaneous effects of chemical reactions and phase change. A $5\mu m$, $n-Dodecane$ droplet preheated to $460\ K$ was initially suspended in a preheated pure O_2 gas at $700\ K$, and impinged by

a Mach 5 shock - we call this our notional droplet, since it could represent operating conditions in a potential pressure-gain combustion engine. Following shock interaction, the Weber number associated with the post-shock flow reached 500, as the fuel droplet evolved through simultaneous deformation, evaporation and burning. To isolate the effects of droplet deformation, evaporation and reactions on droplet evolution, three separate cases corresponding to inert, evaporating and reacting droplets were simulated. Furthermore, since fuel reactivity can vary with operating conditions or composition, we explored deviations from this baseline case, in the form of Damkohler number variations. The simulations in each case were performed to a non-dimensional time $t^* = 1.0$, which we take as representing a nominal breakup time.

We find at early times, the droplet deformation is influenced by KH instabilities that appear on the droplet surface. A quantitative analysis shows the observed KH dominant wavelengths are reasonably close to the values predicted by linear theory [1, 2], but only when the local Weber number effects on the surface of the droplet in each case are considered. In the presence of evaporation, a heavy fuel vapor layer forms, contributing to significant attenuation of KH growth in the early stages. The impact on KH growth also affects the growth of thin sheet structures which appear to be ejected from the droplet equatorial region. For example, the total surface area for a $5\mu m$ droplet under Mach 5 flow, simulated in this work, was observed to decrease by 30% by the end of the simulation, when evaporation effects and chemical reactions were included.

Significant spatial inhomogeneities were observed in the droplet heating in all three scenarios studied in this work. As the hot post-shock gasses impinge on the droplet, a bowshock is formed at a standoff distance from the windward side, predicted by $\frac{\delta_{bowshock}}{D} \approx 0.0715 exp\left(\frac{3.24}{M^2}\right)$ [115].The maximum temperatures were observed at the windward side under

the intense heating by the hot post-bowshock gasses, which were thus the most active sites for vapor production and chemical reactions. In contrast, the presence of entrapped pre-shock cold gasses at low pressures ($\sim 0.5atm - 2atm$) on the leeward side of the droplet exhibits lower evaporation rates by almost two orders of magnitude. Thus, these simulation results challenge the assumptions of uniform droplet heating and evaporation based on the static gas phase temperature, widely used in Lagrangian point-particle calculations. For particles at high relative velocities with respect to the gas, such assumptions could result in significant underprediction of the evaporation rate.

During evaporation, the conversion of the high-density liquid into gas phase $(\rho_g < \rho_l)$ induces a Stefan flow, which blows-off the hot-post shock gasses further cooling the droplet. Together with the convective cooling, these effects were observed to lower the temperature of the evaporating and reacting droplets compared to the non-evaporating (inert) droplet. The total evaporation rate of the reacting droplets increases primarily due to an increase in total surface area of the droplet, while the average evaporation rate becomes constant over time. This is attributed to the production of a fuel-lean mixture due to evaporation, which results in a modest increase in flame temperature, and without a significant effect on droplet surface heating.

As the fuel reactivity was increased through the Damkohler number, the layer of unreacted fuel surrounding the droplet (windward, equatorial and leeward) was found to decrease, while more reaction products were formed. Furthermore, the flame thickness decreased and the flame temperature increased with Da. Our simulations are in broad agreement with laminar diffusion flame theory [116, 117], which predicts that as the Damkohler number is increased, there is a transition from the thick flame regime characterized by slow reactions and cross-diffusion of the fuel and reactants into each other, to a thin flame regime marked by the fuel and oxidizer mixing

and reacting almost instantaneously. As Da is increased, our simulations also show the thin flame sheet shifts toward the more deficient species (i.e. the droplet surface) in agreement with the theory of [116, 117]. Fuel reactivity was also found to affect the evolution of droplet surface morphology, as the thickness of heavy fuel vapor layer surrounding the droplet decreased with increasing reactivity, allowing the sheet structures to expand at a higher rate through the surrounding lower density gas.

The results presented can be used in developing or refining drag and evaporation laws, and droplet deformation models for shock-processed fuel droplets; such models are used as subgrid models in system-level simulations using Lagrangian point-particles [30, 118-120]. We plan to extend this study to finite Ohnesorge numbers by including viscous effects, which will affect the internal circulation within the droplet. In the current simulations, the initial conditions were chosen so that the droplets did not become supercritical over $t^* = 1.0$. Droplets at higher preheated temperatures or shock strengths are likely to enter the supercritical regime over these timescales, which must be addressed through appropriate models [66, 121] for EOS and temperature-dependent liquid phase properties applicable to that regime. Finally, the growth of hydrodynamic instabilities on the droplet surface and subsequent droplet breakup will follow different pathways in a 3D droplet than the 2D axisymmetric case considered here, which will be addressed in future efforts.

REFERENCES

[1] R. A. Jepsen, S. S. Yoon, and B. Demosthenous, "Effects of air on splashing during a large droplet impact: Experimental and numerical investigations," *Atomization Spray,* vol. 16, no. 8, pp. 981-996, 2006. https://doi.org/10.1615/AtomizSpr.v16.i8.80.

[2] S. Chandrasekhar, *Hydrodynamic and hydromagnetic stability*. Dover Publications, 1981. https://store.doverpublications.com/048664071x.html.

[3] AFRL, "Rotating Detonation Engines (RDE)." [Online]. Available: https://afresearchlab.com/technology/rotating-detonation-engines-rde/

[4] L. Blain, "NASA's rotating detonation rocket engine posts record test results," January 31, 2023. [Online]. Available: https://newatlas.com/space/nasa-rotating-detonation-rocket-engine/

[5] P. Wolanski, "Detonative propulsion," *Proceedings of the Combustion Institute,* vol. 34, pp. 125-158, 2013. https://doi.org/10.1016/j.proci.2012.10.005.

[6] K. Kailasanath, *The Rotating Detonation-Wave Engine Concept: A Brief Status Report*. 2011.

[7] D. Schwer and K. Kailasanath, "Numerical investigation of the physics of rotating-detonation-engines," *Proceedings of the Combustion Institute,* vol. 33, pp. 2195-2202, 2011. https://doi.org/10.1016/j.proci.2010.07.050.

[8] R. Zhou, D. Wu, and J. P. Wang, "Progress of continuously rotating detonation engines," *Chinese Journal of Aeronautics,* vol. 29, no. 1, pp. 15-29, Feb 2016. https://doi.org/10.1016/j.cja.2015.12.006.

[9] S. J. Liu, W. D. Liu, Z. Y. Lin, and W. Lin, "Experimental Research on the Propagation Characteristics of Continuous Rotating Detonation Wave near the Operating Boundary," *Combustion Science and Technology,* vol. 187, no. 11, pp. 1790-1804, 2015. https://doi.org/10.1080/00102202.2015.1019620.

[10] J. Kindracki, P. Wolanski, and Z. Gut, "Experimental research on the rotating detonation in gaseous fuels-oxygen mixtures," *Shock Waves,* vol. 21, no. 2, pp. 75-84, Apr 2011. https://doi.org/10.1007/s00193-011-0298-y.

[11] S. Jin, L. Qi, N. B. Zhao, H. T. Zheng, Q. Y. Meng, and J. L. Yang, "Experimental and numerical research on rotating detonation combustor under non-premixed conditions," *International Journal of Hydrogen Energy,* vol. 45, no. 16, pp. 10176-10188, Mar 20 2020. https://doi.org/10.1016/j.ijhydene.2020.02.009.

[12] A. S. George, R. Driscoll, V. Anand, and E. Gutmark, "On the existence and multiplicity of rotating detonations," *Proceedings of the Combustion Institute,* vol. 36, no. 2, pp. 2691-2698, 2017. https://doi.org/10.1016/j.proci.2016.06.132.

[13] V. Anand, A. St George, R. Driscoll, and E. Gutmark, "Characterization of instabilities in a Rotating Detonation Combustor," *International Journal of Hydrogen Energy*, vol. 40, no. 46, pp. 16649-16659, Dec 14 2015. https://doi.org/10.1016/j.ijhydene.2015.09.046.

[14] S. B. Yao, M. Liu, and J. P. Wang, "Numerical Investigation of Spontaneous Formation of Multiple Detonation Wave Fronts in Rotating Detonation Engine," *Combustion Science and Technology*, vol. 187, no. 12, pp. 1867-1878, 2015. https://doi.org/10.1080/00102202.2015.1067202.

[15] F. A. Bykovskii, S. A. Zhdan, and E. F. Vedernikov, "Continuous spin detonation of fuel-air mixtures," *Combustion Explosion and Shock Waves*, vol. 42, no. 4, pp. 463-471, Jul-Aug 2006. https://doi.org/10.1007/s10573-006-0076-9.

[16] F. A. Bykovskii, S. A. Zhdan, and E. F. Vedernikov, "Continuous spin detonations," *Journal of Propulsion and Power*, vol. 22, no. 6, pp. 1204-1216, Nov-Dec 2006. https://doi.org/10.2514/1.17656.

[17] F. A. Bykovskii and S. A. Zhdan, "Current status of research of continuous detonation in fuel-air mixtures," *Combustion Explosion and Shock Waves*, vol. 51, no. 1, pp. 21-35, Jan 2015. https://doi.org/10.1134/S0010508215010025.

[18] L. Deng, H. Ma, C. Xu, X. Liu, and C. S. Zhou, "The feasibility of mode control in rotating detonation engine," *Applied Thermal Engineering*, vol. 129, pp. 1538-1550, Jan 25 2018. https://doi.org/10.1016/j.applthermaleng.2017.10.146.

[19] Z. J. Xia, M. Y. Luan, X. Y. Liu, and J. P. Wang, "Numerical simulation of wave mode transition in rotating detonation engine with OpenFOAM," *International Journal of Hydrogen Energy*, vol. 45, no. 38, pp. 19989-19995, Jul 31 2020. https://doi.org/10.1016/j.ijhydene.2020.05.100.

[20] P. Tarey, P. Ramaprabhu, J. McFarland, and P. Bigdelou, "Investigation of Mode Transition in Rotating Detonation Engines using Detailed Numerical Simulations," in *AIAA Propulsion and Energy 2020 Forum*, 2020.

[21] Z. D. Lei, Z. W. Chen, X. Q. Yang, J. Ding, and P. F. Weng, "Operational mode transition in a rotating detonation engine," *Journal of Zhejiang University-Science A*, vol. 21, no. 9, pp. 721-733, Sep 2020. https://doi.org/10.1631/jzus.A1900349.

[22] Z. X. Ren, B. Wang, G. M. Xiang, D. Zhao, and L. X. Zheng, "Supersonic spray combustion subject to scramjets: Progress and challenges," *Progress in Aerospace Sciences*, vol. 105, pp. 40-59, Feb 2019. https://doi.org/10.1016/j.paerosci.2018.12.002.

[23] J. B. Perurena, C. O. Asma, R. Theunissen, and O. Chazot, "Experimental investigation of liquid jet injection into Mach 6 hypersonic crossflow," *Experiments in Fluids*, vol. 46, no. 3, pp. 403-417, Mar 2009. https://doi.org/10.1007/s00348-008-0566-5.

[24] O. A. Powell, J. T. Edwards, R. B. Norris, K. E. Numbers, and J. A. Pearce, "Development of hydrocarbon-fueled scramjet engines: The Hypersonic Technology (HyTech) program,"

Journal of Propulsion and Power, vol. 17, no. 6, pp. 1170-1176, Nov-Dec 2001. https://doi.org/10.2514/2.5891.

[25] C. Segal, "Introduction," in *Scramjet Engine: Processes and Characteristics*, no. 25), 2009, ch. Introduction, pp. 1-15.

[26] P. Wolanski, W. Balicki, W. Perkowski, and A. Bilar, "Experimental research of liquid-fueled continuously rotating detonation chamber," *Shock Waves,* vol. 31, no. 7, pp. 807-812, Oct 2021. https://doi.org/10.1007/s00193-021-01014-w.

[27] A. J. Harroun, S. D. Heister, and J. H. Ruf, "Computational and Experimental Study of Nozzle Performance for Rotating Detonation Rocket Engines," *Journal of Propulsion and Power,* vol. 37, no. 5, pp. 660-673, Sep-Oct 2021. https://doi.org/10.2514/1.B38244.

[28] C. Sula, H. Grosshans, and M. V. Papalexandris, "Assessment of Droplet Breakup Models for Spray Flow Simulations," *Flow Turbulence and Combustion,* vol. 105, no. 3, pp. 889-914, Sep 2020. https://doi.org/10.1007/s10494-020-00139-9.

[29] S. J. Xue, H. J. Liu, L. X. Zhou, W. D. Yang, H. B. Hu, and Y. Yan, "Experimental research on rotating detonation with liquid hypergolic propellants," *Chinese Journal of Aeronautics,* vol. 31, no. 12, pp. 2199-2205, Dec 2018. https://doi.org/10.1016/j.cja.2018.08.022.

[30] E. P. O. F. Douglas A. Schwer, Jr. and David A. Kessler, "Liquid-Fueled Detonation Modeling at the U.S. Naval Research Laboratory," Naval Research Lab, Washington DC, United States, 2018. https://apps.dtic.mil/sti/pdfs/AD1062712.pdf

[31] J.-P. Rodrigue, *The Geography of Transport Systems*. Routledge, 2020. https://www.routledge.com/The-Geography-of-Transport-Systems/Rodrigue/p/book/9780367364632.

[32] IRENA, "Hydrogen." [Online]. Available: https://www.irena.org/Energy-Transition/Technology/Hydrogen

[33] US-DOE, "Liquefied Natural Gas (LNG)." [Online]. Available: https://www.energy.gov/fecm/liquefied-natural-gas-lng

[34] US-DOE, "Filling CNG Fuel Tanks." [Online]. Available: https://afdc.energy.gov/vehicles/natural_gas_filling_tanks.html#:~:text=Pressure%20rating%3A%20The%20typical%20industry,on%20a%2070%C2%BAF%20ambient%20temperature

[35] J. Han and G. Tryggvason, "Secondary breakup of axisymmetric liquid drops. I. Acceleration by a constant body force," *Phys Fluids,* vol. 11, no. 12, pp. 3650-3667, Dec 1999. https://doi.org/10.1063/1.870229.

[36] J. Han and G. Tryggvason, "Secondary breakup of axisymmetric liquid drops. II. Impulsive acceleration," *Phys Fluids,* vol. 13, no. 6, pp. 1554-1565, Jun 2001. https://doi.org/10.1063/1.1370389.

[37] Z. T. Deng and S. M. Jeng, "Numerical Simulation of Droplet Deformation in Convective Flows," in *AIAA Journal*, vol. 30, no. 5), 1992, pp. 1290-1297.

[38] R. W. Houim and K. K. Kuo, "A ghost fluid method for compressible reacting flows with phase change," *J Comput Phys*, vol. 235, pp. 865-900, Feb 15 2013. https://doi.org/10.1016/j.jcp.2012.09.022.

[39] M. Berglund and C. Fureby, "LES of supersonic combustion in a scramjet engine model," *Proceedings of the Combustion Institute*, vol. 31, pp. 2497-2504, 2007. https://doi.org/10.1016/j.proci.2006.07.074.

[40] S. Bhoite, B. Windom, J. Singh, D. Montgomery, and A. J. Marchese, "A study of ignition and combustion of liquid hydrocarbon droplets in premixed fuel/air mixtures in a rapid compression machine," *Proceedings of the Combustion Institute*, 2022/11/14/ 2022. https://doi.org/10.1016/j.proci.2022.08.125.

[41] A. J. Marchese, T. L. Vaughn, K. Kroenlein, and F. L. Dryer, "Ignition delay of fatty acid methyl ester fuel droplets: Microgravity experiments and detailed numerical modeling," *Proceedings of the Combustion Institute*, vol. 33, pp. 2021-2030, 2011. https://doi.org/10.1016/j.proci.2010.06.044.

[42] T. G. Theofanous, G. J. Li, and T. N. Dinh, "Aerobreakup in rarefied supersonic gas flows," *Journal of Fluids Engineering-Transactions of the Asme*, vol. 126, no. 4, pp. 516-527, Jul 2004. https://doi.org/10.1115/1.1777234.

[43] T. G. Theofanous, "Aerobreakup of Newtonian and Viscoelastic Liquids," *Annual Review of Fluid Mechanics, Vol 43*, vol. 43, pp. 661-690, 2011. https://doi.org/10.1146/annurev-fluid-122109-160638.

[44] T. G. Theofanous and G. J. Li, "On the physics of aerobreakup," *Phys Fluids*, vol. 20, no. 5, May 2008, Art no. 052103. https://doi.org/10.1063/1.2907989.

[45] K. Mizuno, T. Yada, T. Kamiya, M. Asahara, and T. Miyasaka, "Deformation behavior of liquid droplet in shock-induced atomization," *Int J Multiphas Flow*, vol. 155, Oct 2022, Art no. 104141. https://doi.org/10.1016/j.ijmultiphaseflow.2022.104141.

[46] J. Leung and S. Menon, *Design and Test of a Shock Tube Facility to Investigate Droplet Aerobreakup*. 2020.

[47] Z. G. Wang, T. Hopfes, M. Giglmaier, and N. A. Adams, "Experimental investigation of shock-induced tandem droplet breakup," *Phys Fluids*, vol. 33, no. 1, Jan 1 2021, Art no. 012113. https://doi.org/10.1063/5.0039098.

[48] S. Sharma, A. P. Singh, S. S. Rao, A. Kumar, and S. Basu, "Shock induced aerobreakup of a droplet," *J Fluid Mech*, vol. 929, Oct 27 2021, Art no. A27. https://doi.org/10.1017/jfm.2021.860.

[49] B. Dorschner, L. Biasiori-Poulanges, K. Schmidmayer, H. El-Rabii, and T. Colonius, "On the formation and recurrent shedding of ligaments in droplet aerobreakup," *J Fluid Mech*, vol. 904, Dec 10 2020, Art no. A20; PII S0022112020006990. https://doi.org/10.1017/jfm.2020.699.

[50] J. C. Meng and T. Colonius, "Numerical simulation of the aerobreakup of a water droplet," *J Fluid Mech*, vol. 835, pp. 1108-1135, Jan 25 2018. https://doi.org/10.1017/jfm.2017.804.

[51] G. Nykteri and M. Gavaises, "Droplet aerobreakup under the shear-induced entrainment regime using a multiscale two-fluid approach," *Physical Review Fluids*, vol. 6, no. 8, Aug 17 2021, Art no. 084304. https://doi.org/10.1103/PhysRevFluids.6.084304.

[52] M. Jain, R. S. Prakash, G. Tomar, and R. V. Ravikrishna, "Secondary breakup of a drop at moderate Weber numbers," *Proceedings of the Royal Society A-Mathematical Physical and Engineering Sciences*, vol. 471, no. 2177, May 8 2015, Art no. 20140930. https://doi.org/10.1098/rspa.2014.0930.

[53] S. S. Jain, N. Tyagi, R. S. Prakash, R. V. Ravikrishna, and G. Tomar, "Secondary breakup of drops at moderate Weber numbers: Effect of Density ratio and Reynolds number," *Int J Multiphas Flow*, vol. 117, pp. 25-41, Aug 2019. https://doi.org/10.1016/j.ijmultiphaseflow.2019.04.026.

[54] J. W. J. Kaiser, J. M. Winter, S. Adami, and N. A. Adams, "Investigation of interface deformation dynamics during high-Weber number cylindrical droplet breakup," *Int J Multiphas Flow*, vol. 132, Nov 2020, Art no. 103409. https://doi.org/10.1016/j.ijmultiphaseflow.2020.103409.

[55] J. O. Hinze, "Fundamentals of the Hydrodynamic Mechanism of Splitting in Dispersion Processes," *Aiche Journal*, vol. 1, no. 3, pp. 289-295, 1955. https://doi.org/10.1002/aic.690010303.

[56] A. R. Hanson, E. G. Domich, and H. S. Adams, "Shock Tube Investigation of the Breakup of Drops by Air Blasts," *Phys Fluids*, vol. 6, no. 8, pp. 1070-1080, 1963. https://doi.org/10.1063/1.1706864.

[57] G. M. Faeth, L. P. Hsiang, and P. K. Wu, "Structure and breakup properties of sprays," *Int J Multiphas Flow*, vol. 21, pp. 99-127, Dec 1995. https://doi.org/10.1016/0301-9322(95)00059-7.

[58] A. A. Borisov, B. E. Gel'fand, M. S. Natanzon, and O. M. Kossov, "Droplet breakup regimes and criteria for their existence," *Journal of engineering physics*, vol. 40, no. 1, pp. 44-49, 1981/01/01 1981. https://doi.org/10.1007/BF00825066.

[59] Z. K. Xu, T. Y. Wang, and Z. Z. Che, "Droplet breakup in airflow with strong shear effect," *J Fluid Mech*, vol. 941, May 6 2022, Art no. A54. https://doi.org/10.1017/jfm.2022.326.

[60] Z. K. Xu, T. Y. Wang, and Z. Z. Che, "Droplet deformation and breakup in shear flow of air," *Phys Fluids*, vol. 32, no. 5, May 1 2020, Art no. 052109. https://doi.org/10.1063/5.0006236.

[61] M. Jalaal and K. Mehravaran, "Transient growth of droplet instabilities in a stream," *Phys Fluids*, vol. 26, no. 1, Jan 2014, Art no. 012101. https://doi.org/10.1063/1.4851056.

[62] S. Sharma, N. K. Chandra, S. Basu, and A. Kumar, "Advances in droplet aerobreakup," *Eur Phys J-Spec Top*, vol. 232, no. 6, pp. 719-733, Jun 2023. https://doi.org/10.1140/epjs/s11734-022-00653-z.

[63] S.-M. J. a. Z. Deng, "Numerical Simulation of Deformed Droplet Dynamics and Evaporation," in *Recent Advances in Spray Combustion: Spray Combustion Measurements and Model Simulation*, 1996, pp. 305-328.

[64] P. Das and H. S. Udaykumar, "Sharp-interface calculations of the vaporization rate of reacting aluminum droplets in shocked flows," *Int J Multiphas Flow*, vol. 134, Jan 2021, Art no. 103442. https://doi.org/10.1016/j.ijmultiphaseflow.2020.103442.

[65] J. P. Redding and P. Khare, "A computational study on shock induced deformation, fragmentation and vaporization of volatile liquid fuel droplets," *Int J Heat Mass Tran*, vol. 184, Mar 2022, Art no. 122345. https://doi.org/10.1016/j.ijheatmasstransfer.2021.122345.

[66] B. Boyd and D. Jarrahbashi, "Numerical study of the transcritical shock-droplet interaction," *Physical Review Fluids*, vol. 6, no. 11, Nov 15 2021, Art no. 113601. https://doi.org/10.1103/PhysRevFluids.6.113601.

[67] G. Strotos, I. Malgarinos, N. Nikolopoulos, and M. Gavaises, "Aerodynamic breakup of an n-decane droplet in a high temperature gas environment," *Fuel*, vol. 185, pp. 370-380, Dec 1 2016. https://doi.org/10.1016/j.fuel.2016.08.014.

[68] T. G. Theofanous, V. V. Mitkin, C. L. Ng, C. H. Chang, X. Deng, and S. Sushchikh, "The physics of aerobreakup. II. Viscous liquids," *Phys Fluids*, vol. 24, no. 2, Feb 2012, Art no. 022104. https://doi.org/10.1063/1.3680867.

[69] B. Fryxell *et al.*, "Flash: An adaptive mesh hydrodynamics code for modeling astrophysical thermonuclear flashes," *Astrophysical Journal Supplement Series*, vol. 131, no. 1, pp. 273-334, Nov 2000. https://doi.org/10.1086/317361.

[70] N. Attal *et al.*, "Development and validation of a chemical reaction solver coupled to the FLASH code for combustion applications," *Comput Fluids*, vol. 107, pp. 59-76, Jan 31 2015. https://doi.org/10.1016/j.compfluid.2014.09.051.

[71] G. S. Jiang and C. W. Shu, "Efficient implementation of weighted ENO schemes," *J Comput Phys*, vol. 126, no. 1, pp. 202-228, Jun 1996. https://doi.org/10.1006/jcph.1996.0130.

[72] D. Lee and A. E. Deane, "An unsplit staggered mesh scheme for multidimensional magnetohydrodynamics," *J Comput Phys*, vol. 228, no. 4, pp. 952-975, Mar 1 2009. https://doi.org/10.1016/j.jcp.2008.08.026.

[73] P. Colella and P. R. Woodward, "The Piecewise Parabolic Method (Ppm) for Gas-Dynamical Simulations," *J Comput Phys*, vol. 54, no. 1, pp. 174-201, 1984. https://doi.org/10.1016/0021-9991(84)90143-8.

[74] B. J. McBride, *Coefficients for calculating thermodynamic and transport properties of individual species*. NASA, 1993. https://ntrs.nasa.gov/citations/19940013151.

[75] Y. H. Tseng and J. H. Ferziger, "A ghost-cell immersed boundary method for flow in complex geometry," *J Comput Phys*, vol. 192, no. 2, pp. 593-623, Dec 10 2003. https://doi.org/10.1016/j.jcp.2003.07.024.

[76] Y. Wang, L. Qiu, R. D. Reitz, and R. Diwakar, "Simulating cavitating liquid jets using a compressible and equilibrium two-phase flow solver," *Int J Multiphas Flow*, vol. 63, pp. 52-67, Jul 2014. https://doi.org/10.1016/j.ijmultiphaseflow.2014.03.006.

[77] P. Movahed, W. Kreider, A. D. Maxwell, B. Dunmire, and J. B. Freund, "Ultrasound-Induced Bubble Clusters in Tissue-Mimicking Agar Phantoms," *Ultrasound Med Biol*, vol. 43, no. 10, pp. 2318-2328, Oct 2017. https://doi.org/10.1016/j.ultrasmedbio.2017.06.013.

[78] P. Movahed, W. Kreider, A. D. Maxwell, S. B. Hutchens, and J. B. Freund, "Cavitation-induced damage of soft materials by focused ultrasound bursts: A fracture-based bubble dynamics model," *J Acoust Soc Am*, vol. 140, no. 2, pp. 1374-1386, Aug 2016. https://doi.org/10.1121/1.4961364.

[79] R. P. Fedkiw, "The Ghost Fluid Method for Numerical Treatment of Discontinuities and Interfaces," in *Godunov Methods: Theory and Applications*, E. F. Toro Ed. New York, NY: Springer US, 2001, pp. 309-317.

[80] R. P. Fedkiw, T. Aslam, B. Merriman, and S. Osher, "A non-oscillatory Eulerian approach to interfaces in multimaterial flows (the ghost fluid method)," *J Comput Phys*, vol. 152, no. 2, pp. 457-492, Jul 1 1999. https://doi.org/10.1006/jcph.1999.6236.

[81] L. Xu and T. G. Liu, "Accuracies and conservation errors of various ghost fluid methods for multi-medium Riemann problem," *J Comput Phys*, vol. 230, no. 12, pp. 4975-4990, Jun 1 2011. https://doi.org/10.1016/j.jcp.2011.03.021.

[82] W. R. G. Bo, X. T. Liu, J. Glimm, and X. L. Li, "A Robust Front Tracking Method: Verification and Application to Simulation of the Primary Breakup of a Liquid Jet," *Siam J Sci Comput*, vol. 33, no. 4, pp. 1505-1524, 2011. https://doi.org/10.1137/10079135x.

[83] T. G. Liu, B. C. Khoo, and C. W. Wang, "The ghost fluid method for compressible gas-water simulation," *J Comput Phys*, vol. 204, no. 1, pp. 193-221, Mar 20 2005. https://doi.org/10.1016/j.jcp.2004.10.012.

[84] X. Y. Hu and B. C. Khoo, "An interface interaction method for compressible multifluids," *J Comput Phys*, vol. 198, no. 1, pp. 35-64, Jul 20 2004. https://doi.org/10.1016/j.jcp.2003.12.018.

[85] P. Das and H. S. Udaykumar, "A sharp-interface method for the simulation of shock-induced vaporization of droplets," *J Comput Phys*, vol. 405, Mar 15 2020, Art no. 105250. https://doi.org/10.1016/j.jcp.2019.109005.

[86] S. K. Sambasivan and H. S. UdayKumar, "Ghost Fluid Method for Strong Shock Interactions Part 1: Fluid-Fluid Interfaces," *Aiaa J*, vol. 47, no. 12, pp. 2907-2922, Dec 2009. https://doi.org/10.2514/1.43148.

[87] P. Bigdelou, C. Liu, P. Tarey, and P. Ramaprabhu, "An efficient Ghost Fluid Method to remove overheating from material interfaces in compressible multi-medium flows," *Comput Fluids*, vol. 233, Jan 30 2022, Art no. 105250. https://doi.org/10.1016/j.compfluid.2021.105250.

[88] D. P. Peng, B. Merriman, S. Osher, H. K. Zhao, and M. J. Kang, "A PDE-based fast local level set method," *J Comput Phys*, vol. 155, no. 2, pp. 410-438, Nov 1 1999. https://doi.org/10.1006/jcph.1999.6345.

[89] S. Osher and J. A. Sethian, "Fronts Propagating with Curvature-Dependent Speed - Algorithms Based on Hamilton-Jacobi Formulations," *J Comput Phys*, vol. 79, no. 1, pp. 12-49, Nov 1988. https://doi.org/10.1016/0021-9991(88)90002-2.

[90] C.-W. Shu, "High Order ENO and WENO Schemes for Computational Fluid Dynamics," in *High-Order Methods for Computational Physics*, T. J. Barth and H. Deconinck Eds. Berlin, Heidelberg: Springer Berlin Heidelberg, 1999, pp. 439-582.

[91] K. M. Olson and P. MacNeice, "An overview of the PARAMESH AMR software package and some of its applications," *Lect Notes Comp Sci*, vol. 41, pp. 315-330, 2005. [Online]. Available: <Go to ISI>://WOS:000226971600022.

[92] P. MacNeice, K. M. Olson, C. Mobarry, R. de Fainchtein, and C. Packer, "PARAMESH: A parallel adaptive mesh refinement community toolkit," *Comput Phys Commun*, vol. 126, no. 3, pp. 330-354, Apr 2000. https://doi.org/10.1016/S0010-4655(99)00501-9.

[93] M. P. Benjamin J. Musick, Jacob A. McFarland, and Praveen K. Ramaprabhu, "Numerical Simulations of Droplet Evaporation and Breakup Effects on Heterogenous Detonations," *(Submitted)*, 2023.

[94] M. J. Z. Bonnie J. McBride, and Sanford Gordon. NASA Glenn Coefficients for Calculating Thermodynamic Properties of Individual Species [Online] Available: https://ntrs.nasa.gov/citations/20020085330

[95] S. C. a. T. G. Cowling, "The Mathematical Theory of Non-uniform Gases. An account of the kinetic theory of viscosity, thermal conduction, and diffusion in gases. By Sydney Chapman and T. G. Cowling. 2nd Edn., pp. ix, 431. 60s. 1952. (Cambridge University

Press)," *The Mathematical Gazette,* vol. 38, no. 323, pp. 63-64, 1954. https://doi.org/10.2307/3609795.

[96] R. W. Schrage, *A Theoretical Study of Interphase Mass Transfer*. Columbia University Pres, 1953.

[97] E. D. H. Wang, B. Sirjean, D. A. Sheen, R. Tango, A. Violi, J. Y. W. Lai, F. N. Egolfopoulos, D. F. Davidson, R. K. Hanson, C. T. Bowman, C. K. Law, W. Tsang, N. P. Cernansky, D. L. Miller, R. P. Lindstedt. A high-temperature chemical kinetic model of n-alkane (up to n-dodecane), cyclohexane, and methyl-, ethyl-, n-propyl and n-butyl-cyclohexane oxidation at high temperatures, JetSurF version 2.0 [Online] Available: http://web.stanford.edu/group/haiwanglab/JetSurF/JetSurF2.0/index.html

[98] E. Toro, "Riemann Solvers and Numerical Methods for Fluid Dynamics: A Practical Introduction," 2009.

[99] S. Gottlieb and C. W. Shu, "Total variation diminishing Runge-Kutta schemes," *Math Comput,* vol. 67, no. 221, pp. 73-85, Jan 1998. https://doi.org/10.1090/S0025-5718-98-00913-2.

[100] B. C. K. a. N. A. A. X. Y. Hu. A smooth interface interaction method for compressible flows [Online] Available: https://xiangyu-hu.userweb.mwn.de/papers/2005-ISSW25.pdf

[101] K. K.-y. Kuo, *Principles of Combustion,* 2nd ed. John Wiley, 2005. https://www.wiley.com/en-us/Principles+of+Combustion%2C+2nd+Edition-p-9780471046899.

[102] T. Aslam, S. T. Luo, and H. K. Zhao, "A Static Pde Approach for Multidimensional Extrapolation Using Fast Sweeping Methods," *Siam J Sci Comput,* vol. 36, no. 6, pp. A2907-A2928, 2014. https://doi.org/10.1137/140956919.

[103] D. P. D. Frank P. Incropera, Theodore L. Bergman, Adrienne S. Lavine *Fundamentals of heat and mass transfer*, 6th ed. John Wiley & Sons, 2006, p. 1024. https://search.library.wisc.edu/catalog/9910020981602121.

[104] J. S. Evans and C. J. Schexnayder, "Influence of Chemical-Kinetics and Unmixedness on Burning in Supersonic Hydrogen Flames," *Aiaa J,* vol. 18, no. 2, pp. 188-193, 1980. https://doi.org/10.2514/3.50747.

[105] M. F. Ivanov, A. D. Kiverin, I. S. Yakovenko, and M. A. Liberman, "Hydrogen-oxygen flame acceleration and deflagration-to-detonation transition in three-dimensional rectangular channels with no-slip walls," *International Journal of Hydrogen Energy,* vol. 38, no. 36, pp. 16427-16440, Dec 13 2013. https://doi.org/10.1016/j.ijhydene.2013.08.124.

[106] D. A. Kessler, V. N. Gamezo, and E. S. Oran, "Simulations of flame acceleration and deflagration-to-detonation transitions in methane-air systems," *Combustion and Flame,* vol. 157, no. 11, pp. 2063-2077, Nov 2010. https://doi.org/10.1016/j.combustflame.2010.04.011.

[107] A. Y. Poludnenko, T. A. Gardiner, and E. S. Oran, "Spontaneous Transition of Turbulent Flames to Detonations in Unconfined Media," *Physical Review Letters*, vol. 107, no. 5, Jul 27 2011. https://doi.org/10.1103/PhysRevLett.107.054501.

[108] G. Thomas, G. Oakley, and R. Bambrey, "An experimental study of flame acceleration and deflagration to detonation transition in representative process piping," *Process Safety and Environmental Protection*, vol. 88, no. 2, pp. 75-90, Mar 2010. https://doi.org/10.1016/j.psep.2009.11.008.

[109] O. Dounia, O. Vermorel, A. Misdariis, and T. Poinsot, "Influence of kinetics on DDT simulations," *Combustion and Flame*, vol. 200, pp. 1-14, Feb 2019. https://doi.org/10.1016/j.combustflame.2018.11.009.

[110] V. N. Gamezo, T. Ogawa, and E. S. Oran, "Numerical simulations of flame propagation and DDT in obstructed channels filled with hydrogen-air mixture," *Proceedings of the Combustion Institute*, vol. 31, pp. 2463-2471, 2007. https://doi.org/10.1016/j.proci.2006.07.220.

[111] A. Karanam, S. Ganju, and J. Chattopadhyay, "TimeScale Analysis, Numerical Simulation and Validation of Flame Acceleration, and DDT in Hydrogen-Air Mixtures," *Combustion Science and Technology*, Mar 6 2020. https://doi.org/10.1080/00102202.2020.1732363.

[112] S. Jin, C. Xu, H. Zheng, and H. Zhang, "Detailed chemistry modeling of rotating detonations with dilute n-heptane sprays and preheated air," *Proceedings of the Combustion Institute*, vol. 39, no. 4, pp. 4761-4769, 2023/01/01/ 2023. https://doi.org/10.1016/j.proci.2022.08.075.

[113] C. Yan, W. Nie, B. Wang, and W. Lin, "Rotating detonation combustion of liquid kerosene under near-ramjet limit conditions," *AIP Advances*, vol. 13, no. 6, 2023. https://doi.org/10.1063/5.0157988.

[114] A. A. Ranger and J. A. Nicholls, "Aerodynamic Shattering of Liquid Drops," *Aiaa J*, vol. 7, no. 2, pp. 285-&, 1969. https://doi.org/10.2514/3.5087.

[115] F. S. Billing, "Shock-wave shapes around spherical-and cylindrical-nosed bodies," *American Institute of Aeronautics and Astronautics (AIAA)*, vol. 4, 1967. https://doi.org/10.2514/3.28969.

[116] T. Poinsot and D. Veynante, *Theoretical and Numerical Combustion*, 2nd edition ed. 2005. https://www.abebooks.com/9781930217102/Theoretical-Numerical-Combustion-Second-Edition-1930217102/plp.

[117] S. P. Burke and T. E. W. Schumann, "Diffusion flames," *Ind Eng Chem*, vol. 20, no. 1, pp. 998-1004, Jan 1928. https://doi.org/10.1021/ie50226a005.

[118] K. Kailasanath, "Multiphase Detonations in Pulse Detonation Engines-A Status Report," in *39th AIAA/ASME/SAE/ASEE Joint Propulsion Conference and Exhibit*, 2003.

[119] J. A. McFarland, W. J. Black, J. Dahal, and B. E. Morgan, "Computational study of the shock driven instability of a multiphase particle-gas system," *Phys Fluids,* vol. 28, no. 2, Feb 2016, Art no. 024105. https://doi.org/10.1063/1.4941131.

[120] M. Paudel, J. Dahal, and J. McFarland, "Particle evaporation and hydrodynamics in a shock driven multiphase instability," *Int J Multiphas Flow,* vol. 101, pp. 137-151, Apr 2018. https://doi.org/10.1016/j.ijmultiphaseflow.2018.01.008.

[121] K. Jung, Y. Kim, and N. Kim, "Real-Fluid Modeling for Turbulent Mixing Processes of N-Dodecane Spray Jet Under Superciritical Pressure," *Int J Auto Tech-Kor,* vol. 21, no. 2, pp. 397-406, Apr 2020. https://doi.org/10.1007/s12239-020-0037-4.

[122] A. Chandra and P. Keblinski, "Investigating the validity of Schrage relationships for water using molecular dynamics simulations," *J Chem Phys,* vol. 153, no. 12, Sep 28 2020, Art no. 124505. https://doi.org/10.1063/5.0018726.

[123] E. Bird, J. G. Plascencia, and Z. Liang, "Thermal transport across the interface between liquid n-dodecane and its own vapor: A molecular dynamics study," *J Chem Phys,* vol. 152, no. 18, May 14 2020, Art no. 184701. https://doi.org/10.1063/1.5144279.

[124] Z. Liang, T. Biben, and P. Keblinski, "Molecular simulation of steady-state evaporation and condensation: Validity of the Schrage relationships," *Int J Heat Mass Tran,* vol. 114, pp. 105-114, Nov 2017. https://doi.org/10.1016/j.ijheatmasstransfer.2017.06.025.

APPENDIX

APPENDIX A: VALIDATION OF EVAPORATION LAW

In this section, we describe our validation of the Schrage-Knudsen evaporation law with data from Molecular Dynamics (MD) simulations reported in [122]. Previous MD studies [123, 124] have shown the Schrage-Knudsen law accurately predicts the evaporation rate at the interface between the liquid and gas phase. Fig. A 1 shows the simulation setup used in IMPACT, and reproduces the conditions of the MD simulations in [122]. The 1D domain in Fig. A 1 is $216\ nm$ long, with a gaseous zone sandwiched between two liquid regions each of length $3\ nm$. Following [122], liquid water at temperatures of T_{hot} and T_{cold} occupy the end zones, while the simulations were repeated over a range of the liquid temperatures. The region in between is initialized with water vapor with the following properties in all of our simulations:

$$(T, P, \rho, u) = (415\ K, 1\ atm, 0.521\ kg/m, 0\ m/s).$$

Zero-gradient boundary conditions were used at the left and right boundaries of the 1D domain.

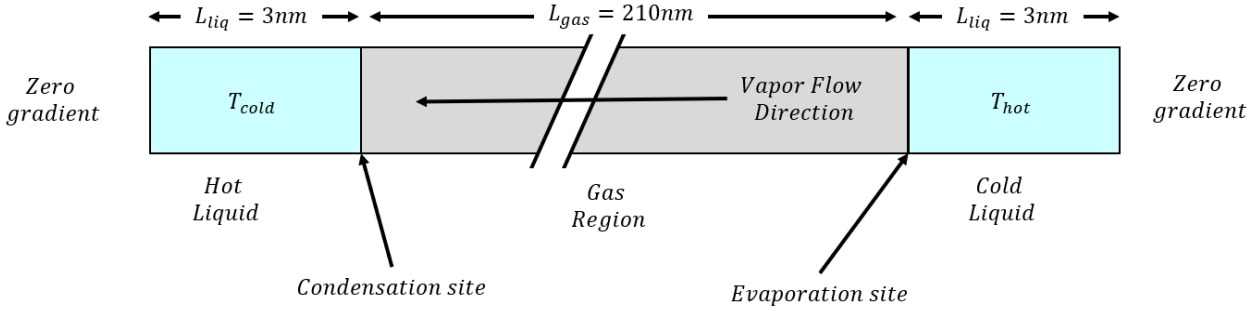

Fig. A 1: 1D domain for MD test case [122] validation in IMPACT.

Table A 1 : Validation between MD and Schrage-Knudsen evaporation law implemented in IMPACT.

	$Case\ 1\ (\Delta T = 10\ K)$			$Case\ 2\ (\Delta T\ = 20\ K)$			$Case\ 3\ (\Delta T\ = 30\ K)$		
$Flow\ Property$	$u_n^v\ (m/s)$	$\rho_v\ (kg/m^3)$	$J"\ (kg/m^2 s)$	$u_n^v\ (m/s)$	$\rho_v\ (kg/m^3)$	$J"\ (kg/m^2 s)$	$u_n^v\ (m/s)$	$\rho_v\ (kg/m^3)$	$J"\ (kg/m^2 s)$
MD [122]	34	1.425	56.5	68	1.435	116.2	110.86	1.49	165.0
$IMPACT$	40	1.438	58.0	82	1.448	119.5	120.0	1.48	178.2
$\%\ Error$	16	0.9	2.62	18	0.9	2.8	8.23	-0.67	7.94

In Table A 1, a comparison of the simulation results obtained from IMPACT and the MD study of [122] is presented. Cases $1 - 3$ correspond to temperature differences between the hot and cold liquid regions of $\Delta T\ = 10\ K$, $20\ K$ and $30\ K$ respectively, where $T_{hot} = T + \Delta T\ /\ 2$, $T_{cold} = T - \Delta T\ /\ 2$ and T is the initial temperature of the water vapor in the intervening region (Fig. A1). From the results summarized in [122], as the temperature difference ΔT is increased, the corresponding vapor mass flux J'' and evaporation induced gas velocity u_n^v increases. The results show agreement in the density and mass flux to within 10 % of the MD results presented in [122]. The percentage error associated with the normal velocities are higher ($10 - 18$ %), and we attribute this to the presence of a transverse velocity (v_T) in the MD simulations [122]. Streamwise (x) profiles of the temperature, normal velocity and density are shown in Fig. A 2 for case 3, which was the simulation with the highest evaporation rate. Results from IMPACT are shown for three times corresponding to $t = 2.4\ ns$, $4.4\ ns$ and $6.4\ ns$, while the MD results from [122] are plotted at $t = 6.4\ ns$. Note that the data points from the MD simulations [122] in Fig. A 2 were obtained by binning and spatially averaging molecular properties within each bin.

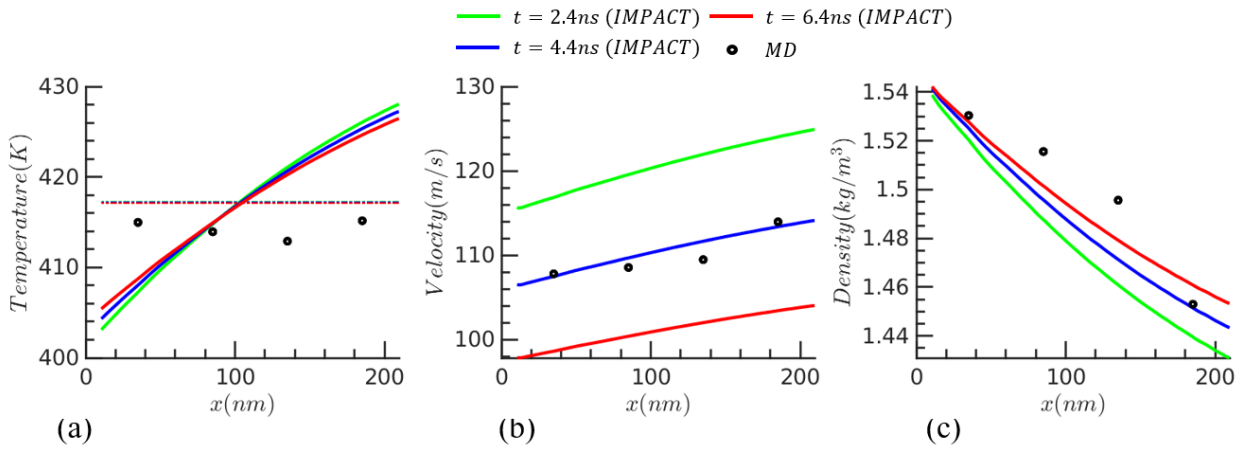

Fig. A 2:Comparison between MD and IMPACT results for case 3 ($\Delta T = 30K$) (a) Temperature (b) Velocity (c) Density. Dashdot lines in fig. (a) shows the x-averaged temperature from IMPACT for $t = 2.4\ ns$, $4.4\ ns$ and $6.4\ ns$.

APPENDIX B: CUT CELL METHOD FOR INTERFACE COUPLING BETWEEN DIFFERENT MATERIALS

The interfacial Riemann Problem illustrated in Fig. 2.1 is solved using the RS-GFM approach of [85, 86], where the following velocity and pressure jump conditions are applied to obtain the intermediate or star states W_{A^*}, W_{B^*}:

$$\left[u_{\eta,*}\right] = \dot{m}''_{l,evap}\left[\frac{1}{\rho_*}\right] \tag{B1}$$

$$[p_*] = -\sigma\kappa - \dot{m}''_{l,evap}\left[u_{\eta,*}\right] \tag{B2}$$

In eq. (B1) and (B2), [ ] represents the jump in a given variable across the interface, and σ and κ are the surface tension coefficient and interface curvature respectively. In this work, liquid $n-Dodecane$ is the only evaporating species, therefore, in eq.(2.17), $\dot{m}''_{O_2} = \dot{m}''_{Prod} = 0$, and $\dot{m}''_{C_{12}H_{26}} = \dot{m}''_l$, with $\dot{m}''_l$ given by eq. (2.10). To compute the temperatures in the interfacial cells, we first solve the interface heat flux ($\dot{q}''_{cond}$) jump condition given by

$$[\dot{q}''_{cond}] = -\dot{m}''_l h_{vap} \tag{B3}$$

where Δh_{vap} is the heat of vaporization of liquid $n-Dodecane$. The interface temperature T_I (eq. B4), can be obtained by solving the heat flux jump condition, eq. B3 in a discretized form, followed by approximation of interfacial cell temperatures, such as T_C (eq. B5) as a linear extrapolation of T_I [85].

$$T_I = \frac{\lambda_A T_A + \lambda_B T_B}{\lambda_A + \lambda_B} \tag{B4}$$

$$T_C = \frac{T_I(\phi_C + \Delta\eta) - \phi_C T_B}{\Delta\eta} \tag{B5}$$

where, ϕ_C is the levelset function value in cell C (Fig. 2.1). A probe length, $\Delta\eta = 1.5dx$ (Fig. 2.1) was used in this work.

APPENDIX C: CALCULATION OF MICRO-DETONATION FORMATION TIMES FOR RDE GEOMETRIES

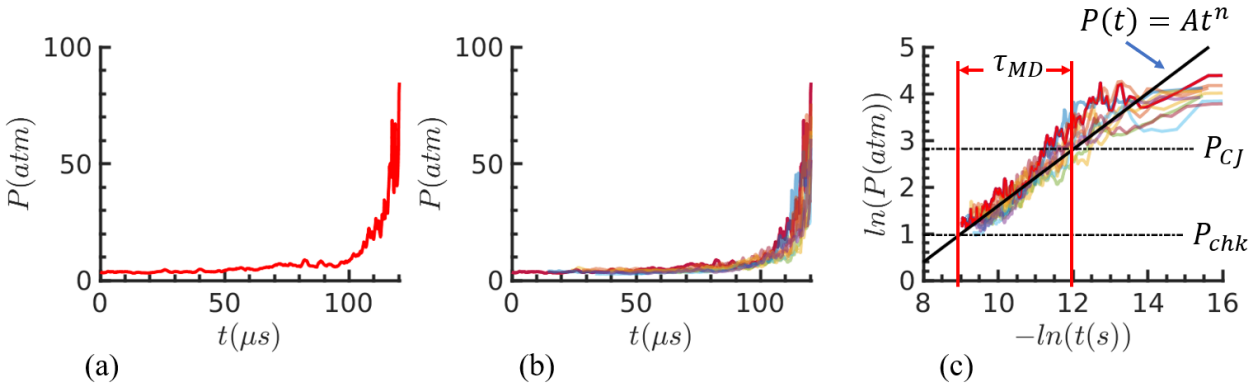

Fig. C 1: Postprocessing of microdetonation (MD) Pressure-time($t-P$) history to obtain τ_{MD} (for $[xN_2]: 5 \rightarrow 2.5$ case) (a) $t-P$ history of a single isolated MD (b) pressure timehistories from multiple MD events time-shifted (c) linear fit on $ln\,(t) - ln\,(P)$ data to estimate $\tau_{MD} = t_{P_{CJ}} - t_{P_{chk}}$.

We briefly describe the procedure used in computing the time-of-formation of micro-detonations that drive mode transition in RDE geometries. The $ln\,(t) - ln\,(P)$ pressure time history plots shown in Fig. 3.14, are obtained by tracking the pressure in the vicinity of a microdetonation. Starting from the deflagrative stage of a hot spot, a moving window is initialized to track the pressure evolution of the hot spot as a function of time (Fig. C 1 (a)). Initially, in the deflagrative stage, the pressure remains almost constant ($t < 75\mu s$) as shown in Fig. C 1 (a) and (b). As the local turbulent mixing leads to the initiation of a deflagration to detonation (DDT) transition, the pressure appears to increase following a power-law behavior: $P(t) = At^n (t > 75\mu s)$. During mode transition, such pressure time histories were tracked for several microdetonations occurring in our simulations. The power law fit (Fig. C 1 (c)) was applied to the pressure timeseries obtained between the initial pressure and the moment the CJ pressure P_{CJ} is reached at that point. Similarly, for simulations in which the Nitrogen dilution was varied, the

parameters of the power law fit can be compared by time-shifting the different timeseries, so that the times at which the P_{CJ} pressure was reached coincided between the datasets.